GAS-PHASE SYNTHESIS OF MULTICOMPONENT MAGNETIC/PLASMONIC NANOPARTICLES FOR CANCER THERANOSTICS

A DISSERTATION
SUBMITTED TO THE FACULTY OF THE GRADUATE SCHOOL
OF THE UNIVERSITY OF MINNESOTA
BY

Pingyan Lei

IN PARTIAL FULFILLMENT OF THE REQUIREMENTS
FOR THE DEGREE OF
DOCTOR OF PHILOSOPHY

Steven L. Girshick, adviser

June, 2013

Acknowledgments

I would like to thank my advisor Professor Steven L. Girshick for his perceptive guidance and continuous support throughout my graduate study and research. I really appreciate his patience, kindness, and insights. I would like to express my gratitude for his help and advice on the organization and writing of this thesis.

I would also like to thank Dr. Adam Boies (University of Cambridge, UK) and Dr. Steven Calder for their assistance and collaboration. I would like to thank Professor Joachim Heberlein for his expert advice on the plasma system; also, I would like to thank Professor John Bischof, Professor Chris Hogan, Professor Jiangping Wang, Professor Carston Wagner, and Professor Taner Akkin for their insightful discussions.

I would also like to thank Zhenpeng Qin, Michael Etheridge, and Sidath Kumarapperuma for their stimulating discussions and advice. Thanks to Vijayanand Kanakadass, Dr. David Rowe, Dr. Rebecca Anthony, and other graduate students in the High Temperature and Plasma Lab for their help and thoughtful conversations.

I would like to extend my thanks to Robin Russell, Pat Nelson, Dave Hultman, Mike Jensen, Robert Jones, and Mike Leveille in the Mechanical Engineering Research Shop for their help in design and machining of the experimental parts.

Finally, I would like to thank my boyfriend Feng Yi for his support and patience, and all my family and friends for their support and encouragement in my life and studies.

This work was funded by the U.S. National Science Foundation under Award Numbers CBET-0730184 and CBET-1066343, and by the Minnesota Futures Grant Program.

To my parents

Abstract

Multi-component nanoparticles have promise for cancer theranostics. This research developed a gas-phase approach for synthesis of multi-layer magnetic/plasmonic nanoparticles, consisting of a superparamagnetic iron oxide core, a continuous silica shell, and an outer layer decorated with gold nanoparticles. These multi-layer nanoparticles can be further coated with hydrophilic polyethylene glycol (PEG), and dispersed in a water solution for future testing, such as imaging, heating, and targeted delivery. Key challenges for manufacturing such nanoparticles include control of the dimensions, morphology, chemical composition and functional properties of each layer.

Superparamagnetic iron oxide nanoparticles (SPIONs) were produced in a DC thermal plasma using ferrocene as the iron precursor. Particle composition and magnetic properties were affected by the O_2 flow rate, plasma power, location of the ceramic tube positioned above the nozzle exit, and use of dilution argon injected downstream of the ferrocene packed bed. The achieved optimum product had a saturation magnetization equalling ~40 emu/g with a coercivity of 26 Oe and a remanence of 1.5 emu/g. These particles had a mean diameter ~9 nm, and mainly contained the magnetite phase. These results were the best ever reported for synthesis of SPIONs by a plasma process.

Plasma-synthesized SPIONs were transported into a coating chamber where a continuous silica shell was grown by means of photo-induced chemical vapor deposition. Silica coating thickness could be tuned between sub-nanometer to several nanometers by varying the residence time and silica precursor flow rate. Gold decoration was achieved

by passing silica-coated iron oxide nanoparticles through a gold hot-wire generator and decoration chamber where small gold nanoparticles were scavenged on the silica surface.

A two-step, gas-phase process was developed for PEGylating gold-decorated silica nanoparticles, by modifying the gold surface with hydroxyl groups, followed by inserting ethylene oxide vapor for polymerization. PEG thickness depended on the ethylene oxide flow rate, PEGylation temperature, and density of the hydroxyl groups on the particle surface. This work was the first reported gas-phase PEGylation of gold-decorated silica nanoparticles.

Several online methods, including scanning mobility particle sizing and tandem differential mobility analysis, were used for characterization of particle size distribution and thickness of individual layers. Particle morphology was characterized by transmission electron microscopy (TEM) with particles collected onto TEM grids, and elemental composition are characterized by energy dispersive spectroscopy in scanning TEM. Bulk powder samples were collected on filters for offline characterization by X-ray diffraction, X-ray photoelectron spectroscopy, Fourier transform infrared spectroscopy, and magnetic property measurement instruments.

Table of Contents

List of Tables

List of Figures

Chapter 1 Introduction and Motivation

1.1 INTRODUCTION

With the development of nanotechnology, engineered nanoparticles have expanded their potential with new uses in many fields, for example, in catalytic, optical, electronic, and biomedical applications. Wet chemistry is the most frequently used approach for the synthesis of nanoparticles, however, this method has potential drawbacks. Wet-chemistry methods normally involve time-consuming batch processes that can last many hours or even days, and nanoparticle production rates are typically small. Moreover, environmental unfriendly surfactants or solvents are usually used in synthesis processes. Thus, hazardous solvents must be managed and discarded properly and impurity residues are a potential problem. Additionally, the physical and chemical properties of the synthesized nanoparticles are sensitive to many experimental parameters, such as reactant ratio, pH value, temperature, and stirring rate. Properties of synthesized particles are usually characterized after the synthesis process has been completed, so that the experimental condition cannot be optimized instantly. Furthermore, during the transfer from the synthesis lab to the characterization facilities, the product may experience the risk of exposure to air, which may bring contamination to the product and lead to a change of the chemical compositions and particle morphology.

An alternative approach, gas-phase synthesis, provides continuous (rather than batch) nanoparticle production with residence times on the order of milliseconds, and

most gas-phase processes are scalable to achieve high production rates. During gas-phase processes, nanoparticles are produced in an inert gas environment, such as N_2 and Ar. No surfactants or solvents are involved, and impurity residues are less of an issue than in wet-chemistry. Moreover, the particle size distribution can be measured in-flight by online characterization techniques (i.e., scanning mobility particle sizer) using a sampling probe. Chemical composition and surface chemistry can be analyzed by mass spectrometry (e.g., inductively-coupled-plasma mass spectrometry) and Fourier transform infrared spectroscopy with the equipment connected online. Rapid feedback of the experimental conditions will be reflected by means of online characterization techniques; thus, the experimental parameters are more easily optimized.

In recent years, multi-component or multi-layer nanoparticles have attracted intense attention from researchers, because such particles combine multiple functions within one single unit. Gas-phase methods have unique advantages for synthesizing multi-layer nanoparticles. The synthesis process can be carried out by a series of sequential steps, each step fabricating one layer or one component. Nanoparticles are produced in a continuous gas stream. The online characterization techniques help to control and optimize both the dimensions and chemical composition of each layer.

1.2 MOTIVATION

Traditional cancer treatments such as surgery, chemotherapy, and radiotherapy have made considerable progress over the past few decades, however, drawbacks persist, such as toxic side effects in certain treatments and low survival rates for some types of

cancer. Multifunctional nanoparticles engineered to provide alternative cancer treatment routes combine both diagnostic and therapeutic functions within a single particle. These particles can be targeted for attachment to specific sites such as tumor cells, and can provide both improved diagnostic capabilities and noninvasive, localized hyperthermia therapy that kills cancer cells.

In this research, a gas-phase approach is established to engineer multi-layer structured nanoparticles consisting of multiple component layers having multiple biofunctional properties for both cancer diagnostics and therapy. The design model of a biofunctionalized, magnetic/plasmonic nanoparticle is shown in Fig.1.1. The design model contains a superparamagnetic iron oxide core (γ-Fe_2O_3 or Fe_3O_4), a dielectric silica inner layer, and a gold layer. The gold layer could be either a continuous gold shell or isolated gold nanoparticles on the surface (called decoration). The magnetic core, which can be either a single iron oxide nanoparticle or agglomerates of nanoparticles, provides enhanced magnetic resonance imaging (MRI) for tumor detection and localized magnetic heating for cancer therapy, while the biocompatible silica layer reduces the coalescence of magnetic nanoparticles and improves the chemical and thermal stability. The gold shell and gold nanoparticles have absorption in the near-infrared and visible wavelength regions, respectively, which can be used for optical imaging and tumor destruction through laser ablation. The multi-component nanoparticles can be further stabilized with hydrophilic polymer coatings, such as polyethylene glycol (PEG), and targeting molecules (e.g., ligands, antibodies, drugs, and receptors). The PEG on the nanoparticle surface increases the solubility and biocompatibility of the nanoparticles in biological

systems, reducing uptake of the nanoparticles by the reticuloendothelial system to allow longer circulation time in the blood. The targeting molecules actively target specific types of cells, directing biofunctionalized nanoparticles to accumulate near tumor cells. The tumor cells then can be killed by hyperthermia. The designed nanoparticles integrate multi-biofunctional components to provide improved diagnostic capabilities and noninvasive therapies for cancer treatments.

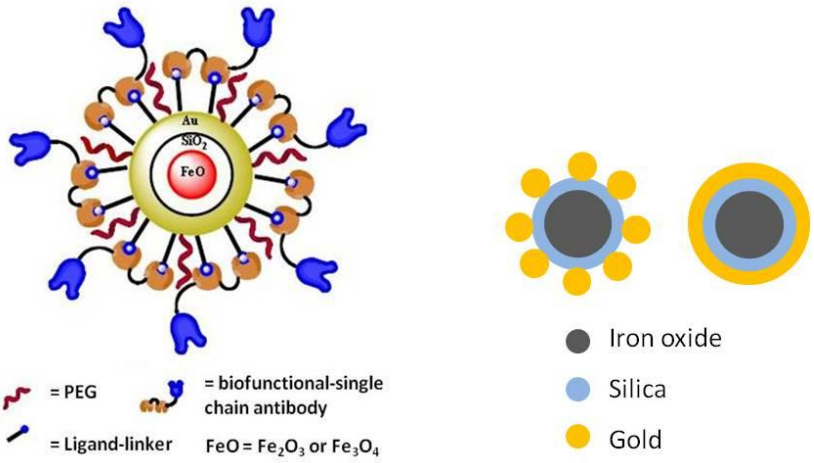

Figure 1.1 Design of magnetic/plasmonic nanoparticles.

1.2.1 Magnetic Iron Oxide Nanoparticles

The magnetic behavior of materials is usually classified into five groups: diamagnetism, paramagnetism, ferromagnetism, ferrimagnetism, and antiferromagnetism [1]. Diamagnetism is due to a change in the electron orbital motion when an external magnetic field is applied, which occurs in all materials. Diamagnetism is a very weak phenomenon, and only those materials composed of atoms which have no net magnetic moments (i.e., all the orbital shells are filled and there are no unpaired electrons) are classified as diamagnetic. Paramagnetism occurs in materials that have net magnetic

moments due to unpaired electrons in partially filled shells. These magnetic moments in paramagnetic materials are weakly coupled to each other, and they are randomly aligned in the absence of an external magnetic field; thus, zero magnetization is observed. Ferromagnetism occurs in materials which have net magnetic moments. The magnetic moments in ferromagnetic materials exhibit very strong interactions produced by electronic exchange forces, resulting in a parallel alignment of magnetic moments. Thus, ferromagnetic materials exhibit a net magnetization even in the absence of a magnetic field. Ferrimagnetism happens in materials composed of at least two sites of magnetic moments, which are antiparallel aligned. The magnetic moments of these two sites are not equal resulting in a net magnetic moment. Thus, the magnetic behavior of ferrimagentism is similar to ferromagnetism. If the two antiparallel aligned sites of magnetic moments are equal, the net magnetization goes to zero in the absence of an external magnetic field. This type of magnetism is called antiferromagnetism, which behaves similarly to paramagnetism. There is another type of magnetism—superparamagnetism—which happens in small ferromagnetic or ferrimagnetic nanoparticles. When the size of particles is sufficiently small, the random thermal energy of the small particles can overcome the magnetic anisotropy energy, allowing the magnetic moment to flip spontaneously for temperatures greater than their blocking temperature, which is generally far below room temperature. The characteristic time between two flips is called the Néelian relaxation time. When the measuring time is much longer than the Néelian relaxation time, net magnetization is not observed in the absence of an external magnetic field.

Iron oxide has several chemical phases. The four most familiar iron oxide phases are wüstite (FeO), maghemite (γ-Fe_2O_3), magnetite (Fe_3O_4), and hematite (α-Fe_2O_3) [2]. Wüstite has a cubic crystal structure, with a magnetism type of paramagnetism, while hematite has a hexagonal crystal structure, with a magnetism type of antiferromagnetism. Both maghemite and magnetite have cubic crystal structures with a magnetism type of ferrimagnetism. The bulk saturation magnetization can reach 60–80 emu/g for maghemite and 90–92 emu/g for magnetite.

Magnetic iron oxide nanoparticles (γ-Fe_2O_3 or Fe_3O_4) have been considered for use in many areas, including data storage, catalysis, environmental remediation, magnetic fluids, and biomedicine [3, 4]. When the magnetic iron oxide particle size is less than 20 nm, the particles exhibit superparamagnetism [2]. At present, there is particularly intense interest in the use of superparamagnetic iron oxide nanoparticles (SPIONs) for biomedical applications due to their high mobility and magnetic properties, such as bacterial detection, protein purification, drug delivery, thermal therapies, and magnetic resonance imaging [5-9].

Superparamagnetic iron oxide nanoparticles are used as contrast-enhancement agents for magnetic resonance imaging, providing non-invasive, three dimensional, and molecular level resolution for imaging internal structures of the human body. During MRI scans, the local magnetic field of superparamagnetic iron oxide nanoparticles accelerates the spin–spin relaxation (transverse relaxation) rate of water protons, resulting in a darker contrast in the MRI. The improved internal structure images can allow detection of liver metastases [10-13]. Kumano et al. also found a similar potential to use

SPIONs as an MRI-enhancement agent to determine metastatic hepatic tumors and nonsolid benign lesions [14].

Moreover, superparamagnetic iron oxide nanoparticles can be heated under an alternating magnetic field, producing a localized temperature increase, which can be used for hyperthermia therapy in cancer treatments. The heating mechanism of superparamagnetic iron oxide nanoparticles comes from Néelian relaxation and Brownian relaxation (Fig. 1.2). For Néelian relaxation, the direction of the magnetic moment of the particle flips with the direction of the alternating magnetic field, while for Brownian relaxation, the particle physically rotates with the direction of the magnetic field. Both mechanisms lead to localized temperature increase under an external alternating magnetic field, killing tumor cells by hyperthermia [15, 16].

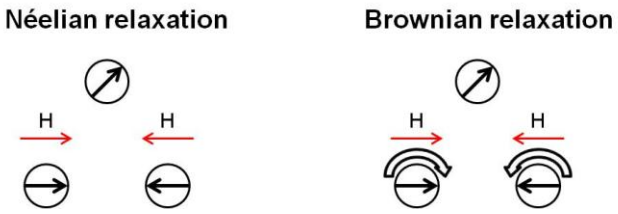

Figure 1.2 Heating mechanisms of superparamagnetic iron oxide nanoparticles under an external alternating magnetic field, *H* is the magnetic field.

1.2.2 GOLD NANOPARTICLES

Gold nanoparticles have been widely used in catalytic and electronic applications owing to their active catalytic activity and unique electronic properties [17-22]. Recently, gold nanoparticles have attracted increasing attention for use in biomedical applications, such as optical imaging [23-25], cancer diagnostics [26-28], and photothermal therapy [29-32]. Gold nanoparticles exhibit surface plasmon resonance (SPR), resulting in a

strong absorption in the visible wavelength region. This strong SPR absorption comes from the collective oscillation of electrons in the conduction band induced by the incident light. The coherent oscillation frequency strongly depends on the particle shape, size, and dielectric constant of the metal particles and surrounding media, as well as temperature. Link et al. measured the UV-vis absorption spectra of different sizes of gold nanoparticles in a water solution [33]. They found that the wavelength of absorption maximum was 517 nm for 9 nm particles, which increased to 575 nm for 99 nm particles, and the absorption bandwidth increased with the particle size. Gold shells have SPR absorption in the near-infrared region. Loo et al. found that the absorption wavelength increased with the core radius/shell thickness ratio for silica core/gold shell nanoparticle [34]. The unique optical properties of gold-based nanoparticles make them a great agent for imaging and diagnostics, and also a promising material for phothotherapy with an external laser, as the strong SPR absorption transfers the laser energy to thermal energy of the particles resulting in a localized temperature increase. The optical properties of gold-based nanostructures can be tuned by their size and shell thickness according to the biomedical application requirements. Additionally, gold nanoparticles are considered a potential candidate for drug delivery and cancer treatment, not only due to their inert, low-toxic, and biocompatible features but also because they can be readily biofunctionalized with targeting molecules for attachment with specific type of cells.

1.3 RESEARCH OBJECTIVES

Nanoparticles designed for use in biological systems have special requirements with respect to particle size, shape, surface chemistry, toxicity, and biocompatibility. The long-term objective of this research is to develop a gas-phase method for synthesizing multi-layer structured multifunctional SPIO@SiO_2@Au@PEG nanoparticles for cancer theranostics. The overall assembly line is shown in Fig. 1.3, consisting of four synthesis steps: superparamagnetic iron oxide production, silica coating, gold decoration, and surface modification (i.e., gas-phase PEGylation). The synthesis process of each component is investigated separately to study the effect of experimental parameters on the chemical composition, morphology, and magnetic/optical properties.

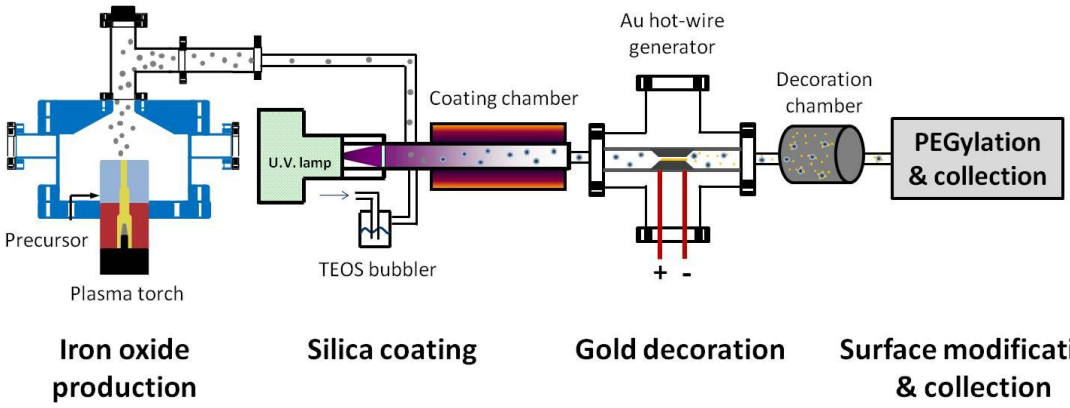

Figure 1.3 Schematic of multi-functional nanoparticle synthesis assembly line.

This thesis is divided into six chapters. Chapter 1 contains the introduction and motivation for the research project. Chapter 2 describes the synthesis process of SPIONs using a DC thermal plasma. Chapter 3 introduces the photo-induced chemical vapor deposition (photo-CVD) method for synthesizing silica coatings on iron oxide

nanoparticles. Chapter 4 establishes a gas-phase PEGylation process for growing polyethylene glycol coatings on gold-decorated silica nanoparticles. Chapter 5 presents some preliminary results on synthesis of tri-layer SPIO@SiO_2@Au nanoparticles. Chapter 6 summarizes the results from each synthesis process, and some future recommendations are also discussed.

1.4 Online Characterization Methods

1.4.1 Scanning Mobility Particle Sizer

The particle size distribution can be measured online by a scanning mobility particle sizer (SMPS) system, consisting of an electrical neutralizer (Po-210 bipolar charger), a differential mobility analyzer (DMA, TSI model 3085), and a condensation particle counter (CPC, TSI model 3025A). First, polydisperse particles are charged by passing through the bipolar charger, and then enter the DMA which samples out monodisperse particles. The monodisperse particles from the DMA exit are sent into the CPC to determine the particle number density. The SMPS system is controlled by a LabVIEW program with a scanning range of the particle mobility diameter of 3–80 nm for the system used in this study.

The charge distribution of particles passing through the bipolar charger used in this research can be described by an approximate formula given by Wiedensohler [35]:

$$f(N) = 10^{[\sum_{i=0}^{5} a_i(N)(log\frac{D_p}{nm})^i]} \quad (1.1)$$

where N is the number of elementary charge units on the particle, a_i is the approximation coefficient, and D_p is the particle diameter. Equation 1.1 is valid for the size ranges:

$$1 \text{ nm} \leq D_p \leq 1000 \text{ nm, for } N = -1, 0, 1$$

$$20 \text{ nm} \leq D_p \leq 1000 \text{ nm, for } N = -2, 2$$

The approximation coefficients for Equation 1.1 are listed in Table 1-1.

$a_i(N)$	N=-2	N=-1	N=0	N=1	N=2
a_0	-26.3328	-2.3197	-0.0003	-2.3484	-44.4756
a_1	35.9044	0.6175	-0.1014	0.6044	79.3772
a_2	-21.4608	0.6201	0.3073	0.4800	-62.8900
a_3	7.0867	-0.1105	-0.3372	0.0013	26.4492
a_4	-1.3088	-0.1260	0.1023	-0.1553	-5.7480
a_5	0.1051	0.0297	-0.0105	0.0320	0.5049

Table 1-1 Coefficients for Equation 1.1 [35].

Based on this calculation, most of the particles are singly charged after passing through the bipolar charger. The charge distributions are plotted for both -1 and +1 particles in Fig. 1.4. The results show that these negative and positive particles are not equally charged: the percentage of negative particles (-1) is somewhat higher than that of positive particles (+1), indicating that the bipolar charger charges particles negatively more efficiently than it charges particles positively.

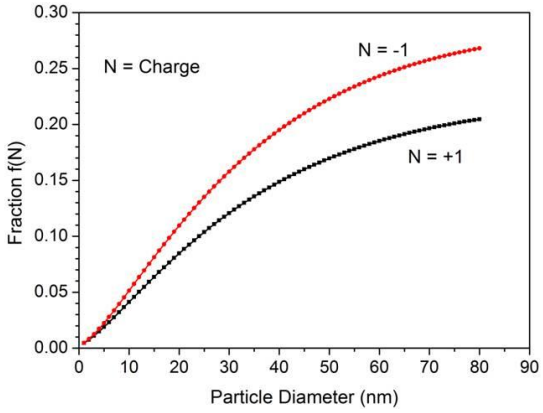

Figure 1.4 Bipolar charge distribution for $N = -1$, and $N = 1$ particles.

The differential mobility analyzer selects particles based on the particle electrical mobility (Z_p), defined as:

$$Z_p = \frac{neC_c}{3\pi\mu D_p} \tag{1.2}$$

where n is the number of elementary charges on the particles, e is the elementary charge, C_c is the Cunningham slip correction factor, μ is the gas viscosity, and D_p is the particle diameter. An expression for the slip correction is given by Allen and Raabe [36]:

$$C_c = 1 + Kn[1.142 + 0.558 \exp(-\frac{0.999}{Kn})] \tag{1.3}$$

where $Kn = 2\lambda/D_p$ is the Knudsen number, and λ is the gas mean free path.

A schematic of the Nano DMA used here is shown in Fig. 1.5 [37]. The DMA consists of two concentric metal cylinders: the outer cylinder is electrically grounded; the inner cylinder—center rod—is kept at a negative or positive potential which is provided by a high-voltage power supply (BERTAN model 25B-10R). Polydisperse aerosol (Q_p)

and sheath flow (Q_{sh}) pass through the annular space between the cylinders. If the inner cylinder is kept at a positive voltage, negative particles entering the DMA are attracted by the electric force and move towards the center rod. Only particles within a narrow range of electrical mobility can exit with the monodisperse flow (Q_m) through the small slit located at the bottom of the center rod, while the rest of particles are precipitated along the rod or carried out in the excess flow (Q_e).

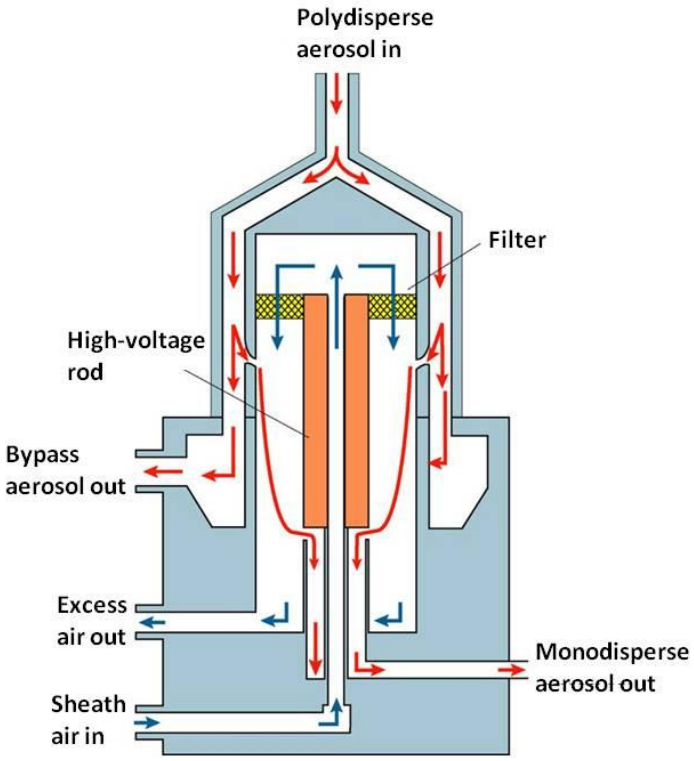

Figure 1.5 Schematic diagram of the model 3085 nano DMA [37].

The DMA transfer function (Ω) is defined as the probability that particles with a given electrical mobility Z_p that enter the DMA via the aerosol inlet leave via the sampling flow [38]. Knutson and Whitby found that the DMA transfer function has a

triangular shape centered at $Z_p{}^*$, as seen in Fig. 1.6 (a). If $Q_{sh} = Q_e$, $Q_p = Q_m$, and $Q_{sh}/Q_p = 10$, the transfer function is given by:

$$Z_p{}^* = \frac{Q_{sh}}{2\pi VL} ln\,(\frac{r_2}{r_1}) \tag{1.4}$$

The half-width of the mobility band ΔZ_p is given by:

$$\Delta Z_p = \frac{1}{10} Z_p{}^* \tag{1.5}$$

where V is the voltage on the center rod, r_2 is the outer radius of annular space, r_1 is the inner radius of annular space, and L is the length between polydisperse aerosol inlet and monodisperse exit slit. For the Nano DMA, r_2 = 1.905 cm, r_1 = 0.937 cm, and L = 4.987 cm. The Nano DMA transfer function Ω vs. particle mobility diameter D_p is plotted in Fig1.6 (b), with 10 slm of N_2 sheath and 1 slm of aerosol flow.

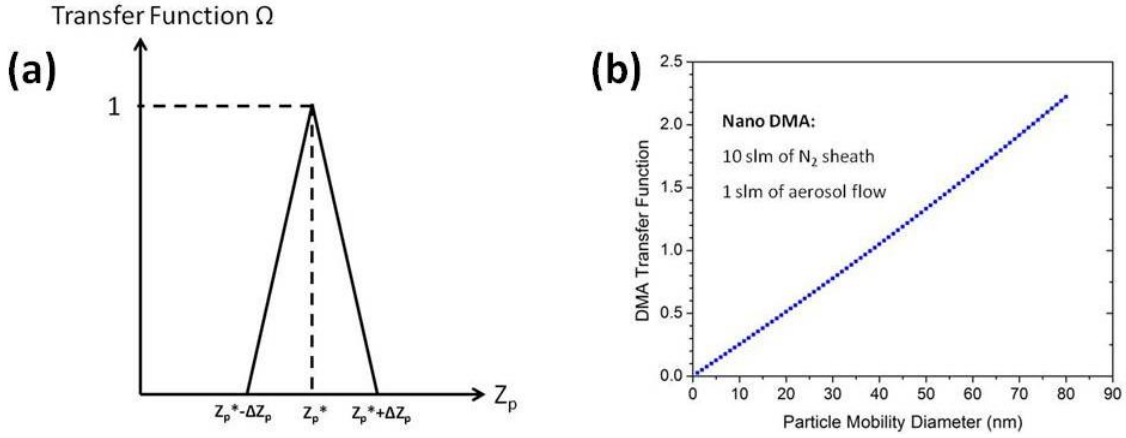

Figure 1.6 DMA transfer function.

Based on Equation 1.2 and 1.4, one can get the relation between the particle diameter D_p and DMA voltage V described as below:

$$D_p = \frac{2neLC_c}{3\mu Q_{sh} \ln\left(\frac{r_2}{r_1}\right)} V \tag{1.6}$$

Thus, the size of the particles sampled out by the DMA can be controlled by the center rod voltage for a given sheath flow rate and DMA geometry. When the DMA voltage is applied in a scanning mode, the particle size distribution can be determined with the combination of CPC results. Raw data of particle counts scanned by the SMPS system can be transferred to the particle size distribution with corrections of the bipolar charge efficiency and DMA transfer function. The raw data of the particle distribution obtained by SMPS is shown in Fig. 1.7(a), while the corrected particle size distribution is shown in Fig. 1.7(b). The peak of the corrected size distribution tends to shift to a smaller diameter. This is because both the bipolar charge efficiency and DMA transfer function increase as particle mobility diameter increases.

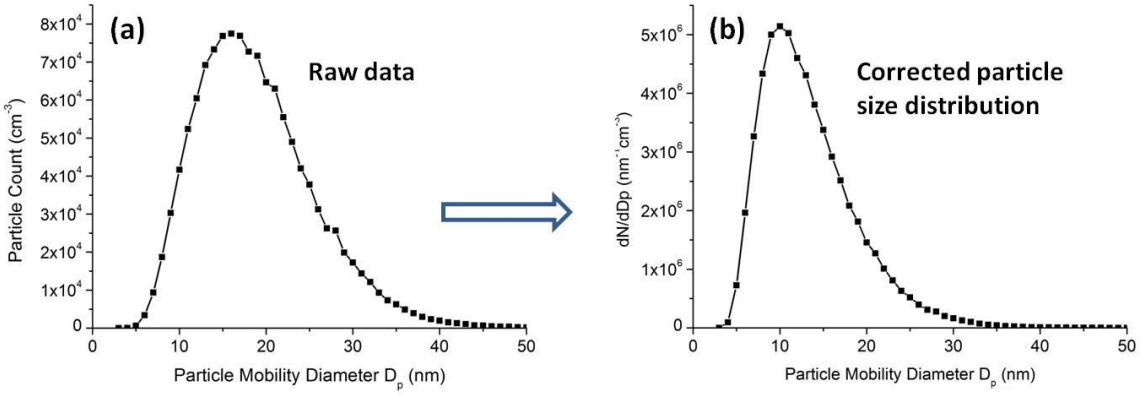

Figure 1.7 SMPS results: (a) raw data; (b) corrected particle size distribution.

1.4.2 TANDEM DIFFERENTIAL MOBILITY ANALYZER

Two DMAs can be connected in series to form a tandem differential mobility analyzer (TDMA) system. The first DMA generates particles of a narrow size range

(monodisperse) from polydisperse aerosols based on the particle electrical mobility (Fig. 1.8). Next, the monodisperse particles undergo experimental processes, such as evaporation, condensation, or chemical reaction, resulting in a particle size change, which is monitored by the second DMA. The TDMA system was first used by Liu et al. to investigate size changes in sulfuric acid aerosol particles [39]. McMurry et al. reported the use of a TDMA system for studying the reaction rate between ammonia gas and sulfuric acid aerosols [40]. Rader et al. also described the application of a TDMA system for studies of droplet growth or evaporation [41]. Recently, a TDMA system has been used as an online technique to study organic coatings on sodium chloride nanoparticles [42] and silica coating on silver nanoparticles [43] by a photo-CVD method. In this research, a TDMA system is used to monitor the photo-CVD silica coating on iron oxide nanoparticles (Chapter 3), and gold decoration on silica nanoparticles and gas-phase PEGylation of gold-decorated silica nanoparticles (Chapter 4).

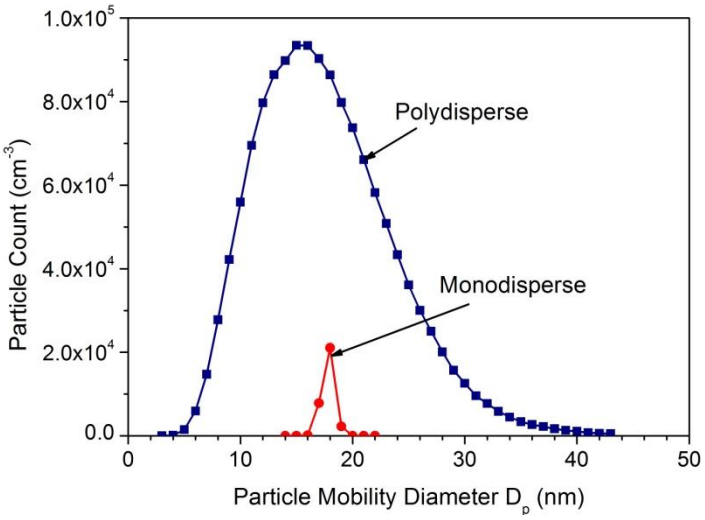

Figure 1.8 SMPS results of particle counts for polydisperse and monodisperse particles, the monodisperse particles were generated by selecting particles at a diameter of 19 nm by the first DMA in a TDMA system.

Chapter 2 Thermal Plasma Synthesis of Magnetic Iron Oxide Nanoparticles

2.1 BACKGROUND

As discussed in the previous chapter, superparamagnetic iron oxide nanoparticles are considered a promising agent for cancer theranostics, which provides improved cancer diagnostic abilities and localized hyperthermia to damage and kill cancer cells using an external alternating magnetic field [44-46]. Numerous studies have reported synthesis of SPIONs. The most common method is through wet chemistry by co-precipitation of Fe^{+2} and Fe^{+3} salts in alkaline solutions [6, 47-49]. Iron oxide nanoparticles synthesized by wet-chemistry usually have a broad size distribution, and surfactants are typically required to suppress agglomeration. These surfactants may need to be removed from the nanoparticle surfaces before subsequent coating and/or functionalization for biomedical applications. The gas-phase approach produces nanoparticles in a continuous gas stream, and no surfactants are used. While for biomedical applications the final desired product is nanoparticles in aqueous dispersion, a number of recent studies have demonstrated gas-phase functionalization or coating of aerosol nanoparticles [43, 50, 51]. Thus, the gas-phase synthesis could involve a sequential, continuous-flow process, involving SPION synthesis followed by surface functionalization or coating, followed by dispersion into liquid.

A number of gas-phase methods have been utilized to synthesize iron oxide nanoparticles, the most common being combustion flames and plasmas. This study focuses on the latter; and a comparison of my results with those obtained with flame synthesis is discussed in the ‘‘Results and Discussion’’ section.

Plasma synthesis of iron and iron oxide nanoparticles has been the subject of a number of studies, dating to at least 1981. Several types of plasmas have been used, including radio frequency (RF) thermal plasmas [52, 53], microwave plasmas [54-62], transferred arcs [63-67], non-transferred arc direct current (DC) plasmas [63, 68], and low-pressure RF plasmas [69-73]. Iron-containing chemical precursors have included solid iron or steel anodes or wire electrodes [63-67], coarse iron powder injected into a plasma, where it evaporates and recondenses [52, 53, 68], and vapor-phase compounds including ferrocene ($Fe(C_5H_5)_2$) [54, 69, 70, 73], iron trichloride ($FeCl_3$) [55, 56], iron pentacarbonyl ($Fe(CO)_5$) [57-63, 71, 72], and triiron dodecacarbonyl ($Fe_3(CO)_{12}$) [56].

Unfortunately, only a few of these studies characterized the magnetic properties of the material produced. Vollath et al. [56], in their microwave synthesis experiments, reported superparamagnetic behavior when they used $FeCl_3$ as the precursor but not for the case when $Fe_3(CO)_{12}$ was used. In the former case, the saturation magnetization M_s at room temperature measured ~4 emu/g, which is too low to be useful for most applications. Kalyanaraman et al. [57], who also used a microwave plasma, also reported superparamagnetism, though they noted that their magnetic measurements were preliminary, and they did not report values of specific saturation magnetization. Similarly, McIlroy et al. [70], who injected ferrocene into a low-pressure RF plasma

without adding additional oxygen, in an attempt to produce pure Fe nanoparticles, found only Fe_3O_4, and reported magnetic properties ‘‘reminiscent of superparamagnetic behavior,’’ though their sample sizes were too small to quantify this effect. Pure Fe nanoparticles are superparamagnetic for sizes smaller than about 8 nm [74]. However, it is difficult to produce pure Fe nanoparticles, because their high specific surface area, together with the high affinity of iron for oxygen—pure Fe nanoparticles are highly pyrophoric—make it difficult to avoid oxidation either during or after particle synthesis.

The group of Banerjee et al. [64, 65, 67], who used transferred arcs with iron anodes, performed extensive magnetic characterization of the material they produced. However, their reported particle sizes were mostly too large (> 20 nm) for superparamagnetism. They reported values of saturation magnetization as high as 88 emu/g for magnetite and 79 emu/ g for maghemite, close to the bulk values, but their high measured coercivities, ~350 Oe, indicated that their material was not superparamagnetic. Panchal et al. [39] synthesized SPIONs using low-pressure argon RF plasmas into which they injected either ferrocene or iron pentacarbonyl [72]. In the ferrocene case no oxygen was added, the objective being to produce pure Fe particles, but, as in [70], they found only oxide particles, consisting of 25–40 nm agglomerates composed of 2–4 nm crystallites. Magnetic property measurements showed that the particles were superparamagnetic, although the apparent saturation magnetization at 300 K, ~6 emu/g, was low. In the case of iron pentacarbonyl as precursor, they obtained particle diameters of 7–14 nm, and magnetic property measurements showed the particles to be superparamagnetic. The saturation magnetization at 300 K measured 21 emu/g, a more

promising value for potential applications. However it should be noted that their method is a batch process, since the nanoparticles become negatively charged and trapped in the nonthermal RF plasma, and are collected when the plasma is turned off. The authors noted that their powder yields were low.

In this chapter, I demonstrate the synthesis of SPIONs using a DC thermal plasma with injected ferrocene vapor together with various flow rates of oxygen. Experimental parameters were optimized for the production of magnetic iron oxides with high saturation magnetization and small coercivity to exhibit superparamagnetism. For cases with sufficient oxygen flow, the powders produced were found to consist substantially of magnetite, possibly mixed with maghemite, and were superparamagnetic, with values of saturation magnetization at room temperature around 40 emu/g at a coercivity of 26 Oe. To my knowledge, this is the best magnetic performance achieved to date for any plasma synthesis of SPIONs, and is comparable to the best reported results for flame synthesis.

2.2 Experimental Procedure

2.2.1 Plasma System

A DC thermal plasma system is used for synthesis of SPIONs. The plasma system has three components: a plasma torch gun (PRAXAIR SG-100), a DC power supply (Topcon 32 kW), and a high frequency starter (PRAXAIR HF-2200). Fig. 2.1 shows the electrical connection among these three components. The DC power supply provides output readings of the voltage, current, and power. The voltage and current can be

controlled at the front panel. The high-frequency starter generates a high-voltage pulse to ignite the plasma. The plasma gun is cooled by deionized water. A gas sensor located in the plasma gas delivery line and a water sensor located in the torch cooling water line make sure that the plasma torch is ignited safely, which means that the plasma can only be ignited when both sensors detect gas/water flowing in the lines. The entire system is grounded to the earth.

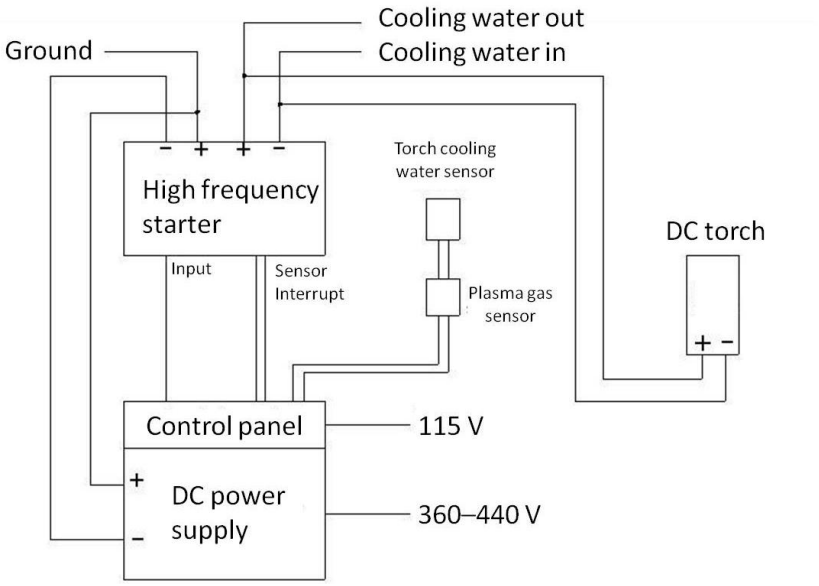

Figure 2.1 Electrical connection of the DC plasma system.

A DC thermal plasma torch normally consists of three main components: a tungsten tipped cathode, a gas injector, and a copper anode. The nozzle-shaped anode also acts as an arc constrictor in the non-transferred arc torch, in which a plasma jet is formed for plasma spraying and powder synthesis applications, as shown in Fig. 2.2. The plasma is usually ignited by a high-frequency starter that provides a high-voltage pulse to create a conducting band forming an electric arc between the cathode and anode. The

electric heating produced by this arc causes the gas to reach a high temperature (> 10,000 K) that can dissociate and ionize most materials. The commercial PRAXAIR SG-100 plasma guns are usually designed for higher power (> 40 kW) applications. The electrodes of the plasma gun used for this study were modified to operate at low power (< 10 kW) with a reduced inner diameter of the anode and a reduced diameter of the cathode. These modifications were made by Thermach Inc..

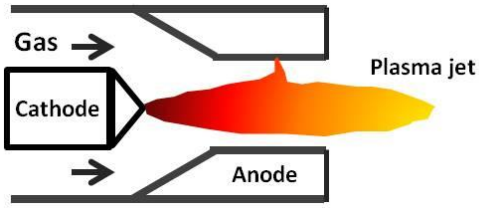

Figure 2.2 Plasma jet inside a DC plasma torch.

2.2.2 EXPERIMENTAL SETUP

The experimental system used to synthesize SPIONs is shown schematically in Fig. 2.3. The plasma was generated by the DC plasma torch, which was operated at a current in the range of 200–250 A. The main plasma gas was argon kept constant at 30 slm. Hydrogen or helium was added with the main argon flow to further increase the power. Gas flow rates were controlled by mass flow controllers (Sierra 810C). The cooling water flow rate for the plasma torch was set at ~11.4 liters per minute.

Ferrocene (Sigma-Aldrich, F408-100G) was used as the iron precursor. Ferrocene vapor was introduced into the plasma using a packed bed [75, 76] comprised of a stainless steel tube filled with 3-mm-diameter glass beads (Sigma-Aldrich), over which the powder was dispersed. The ferrocene vapor was entrained in 500 sccm of argon

flowing through the packed bed. The packed bed was maintained at 120 ℃ using a heating mantle to get sufficient vapor pressure. The ferrocene vapor flow rate was controlled by adjusting the total pressure of the packed bed in the range of 67–101 kPa.

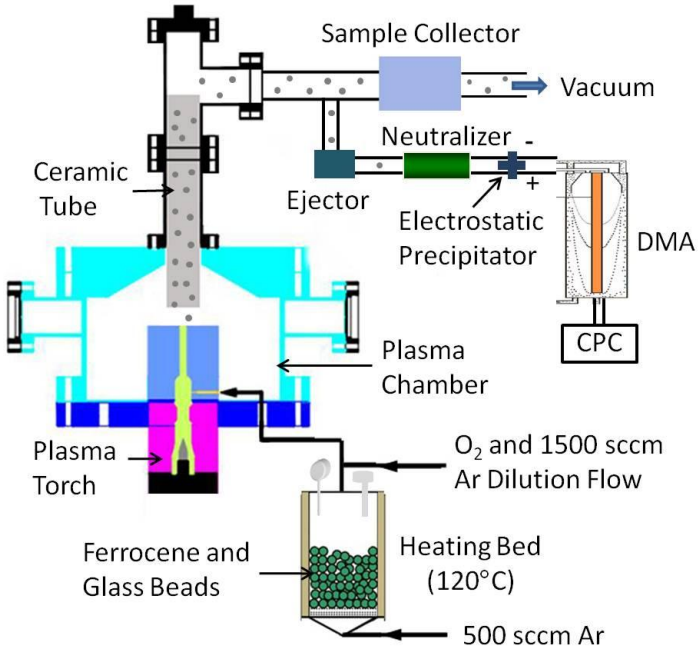

Figure 2.3 Schematic of experimental setup.

Oxygen was introduced downstream of the packed bed, and the resulting mixture was injected into the plasma at 9.5 mm downstream of a converging nozzle inlet. The ceramic nozzle was made of boron nitride. An additional 1500-sccm Ar dilution could be injected downstream of the packed bed to reduce clogging. All precursor delivery lines were heated to 125–145 ℃ to avoid ferrocene condensation before injection into the plasma. The flow exiting the nozzle expanded into a 250-mm-diameter chamber, maintained at a pressure in the range 40–53 kPa. A ceramic tube (32-mm OD, 25-mm ID, 356-mm length) was positioned above the nozzle exit to provide a longer, more uniform

high-temperature region for the nanoparticles that nucleate in the nozzle expansion [77]. Argon quench flow could be injected downstream of the ceramic tube to suppress particle agglomeration. Experiments were conducted to explore the effects of several system parameters, including plasma type (i.e., adding H_2 or He), arc current, ceramic tube position, and flow rates of helium, argon quench gas, ferrocene vapor, additional oxygen gas, and argon dilution gas that was mixed with the precursor vapor before injection into the plasma.

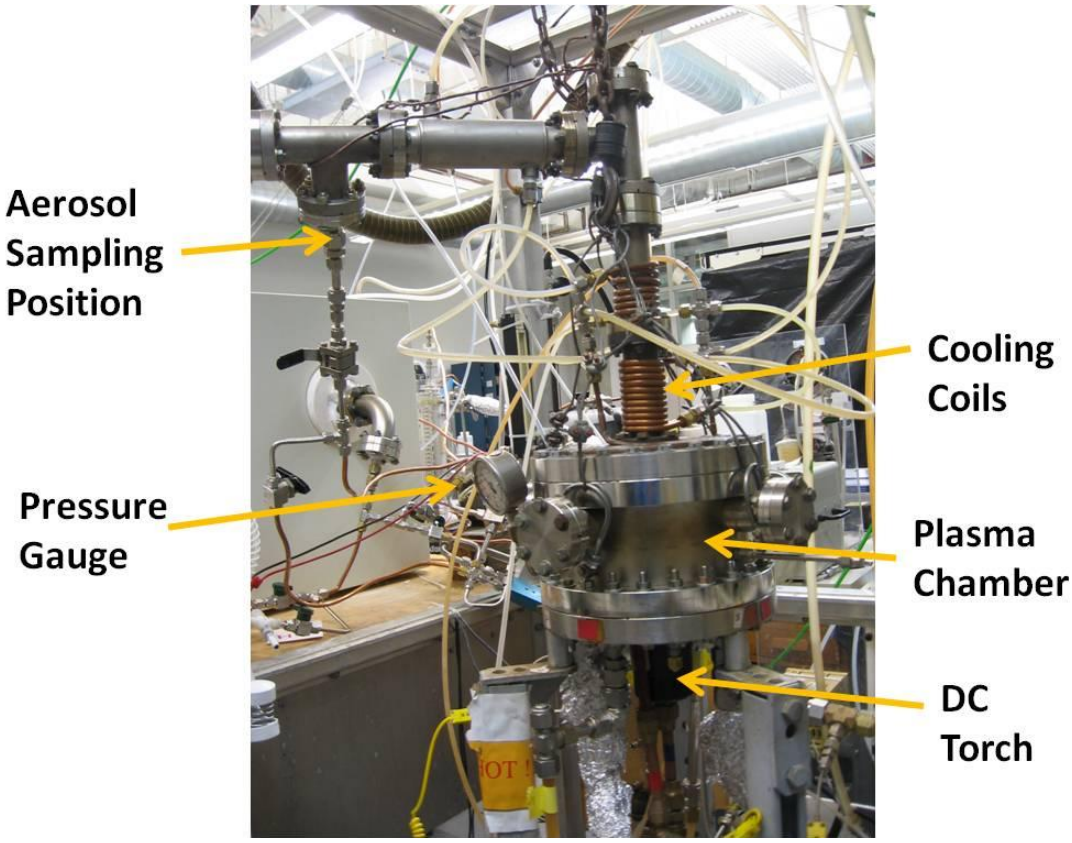

Figure 2.4 Photograph of the DC plasma reactor system.

Fig 2.4 shows a photograph of the DC plasma reactor system. The plasma gun is mounted on the bottom of the plasma chamber. A boron nitride ceramic nozzle (inside

the plasma chamber) positioned at the exit of the plasma torch is used for precursor injection. The plasma jet is confined inside the ceramic nozzle, maintaining the high temperature, and then it expands into the large chamber, where the temperature decreases rapidly and particle nucleation occurs. A pressure gauge connected to the chamber indicates the inside chamber pressure. Cooling water coils are used on the top of the chamber wall to protect the chamber from the high temperature, and also downstream to provide cooling for the exhaust gas. Plasma-synthesized aerosols can be either sampled into an online scanning mobility particle sizer system for particle size distribution measurements or collected on glass fiber filters for offline characterization.

2.2.3 FERROCENE VAPORIZATION

Ferrocene is a stable yellow powder at room temperature and sublimes upon heating. It is a much safer reagent than iron pentacarbonyl, which is highly flammable and toxic. The sublimation of ferrocene was achieved inside the packed bed, as shown in Fig. 2.5. A pressure gauge and thermocouple were used to control the total pressure and temperature, respectively. The equilibrium vapor pressure of ferrocene was determined using the simplified Clark and Glew equation [78].

$$R ln \frac{p}{p^0} = -\frac{\Delta_{cd}^{g} G_m^0(\theta)}{\theta} + \Delta_{cd}^{g} H_m^0(\theta) \left(\frac{1}{\theta} - \frac{1}{T}\right) + \Delta_{cd}^{g} C_{p,m}^0(\theta)(\frac{\theta}{T} - 1 + \ln\left(\frac{T}{\theta}\right)) \qquad (2.1)$$

where p is the vapor pressure, p^0 is a selected reference pressure, θ is a selected reference temperature, R is the molecular gas constant, $\Delta_{cd}^{g} G_m^0(\theta)$ is difference of the molar Gibbs free energy between the gaseous and the condensed phase (crystalline or

liquid) at the selected reference pressure, $\Delta_{cd}^{g}H_{m}^{0}(\theta)$ is the difference of the molar enthalpy between the gaseous and the condensed phase at the selected reference pressure, $\Delta_{cd}^{g}C_{p,m}^{0}(\theta)$ is the difference between the heat capacities of the perfect gas and of the condensed phase. At reference temperature $\theta = 298.15$ K and pressure $p^{0} = 10^{5}$ Pa, the parameters of Equation 4.1 for ferrocene are listed as below [78]: $\Delta_{cd}^{g}G_{m}^{0}(\theta) = 28562\ \mathrm{J \cdot mol^{-1}}$, $\Delta_{cd}^{g}H_{m}^{0}(\theta) = 74488\ \mathrm{J \cdot mol^{-1}}$, and $\Delta_{cd}^{g}C_{p,m}^{0}(\theta) = -45.4\ \mathrm{J \cdot K^{-1} \cdot mol^{-1}}$. Fig. 2.6 shows the calculated equilibrium vapor pressure P_{Ferro} vs. T curve. At a temperature of 120 ℃, the equilibrium vapor pressure of ferrocene equals 1,165 Pa.

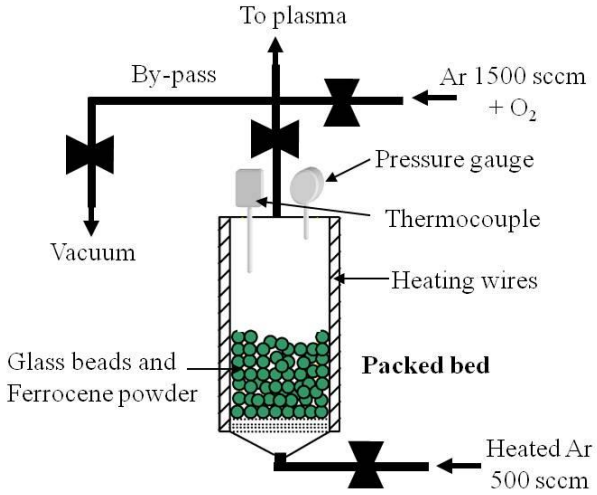

Figure 2.5 Packed bed for ferrocene vaporization.

The temperature, total pressure, and argon carrier gas flow rate determine the amount of ferrocene vapor delivered. When all three parameters are given, the ferrocene vapor flow rate (Q_{Ferro}) can be estimated using

$$Q_{Ferro} = \frac{P_{Ferro}}{P_{Ar}} Q_{Ar} \tag{2.2}$$

where the partial pressure of the argon carrier gas (P_{Ar}) is the difference between the total pressure and the ferrocene vapor pressure (P_{Ferro}). For experiments described here, the packed bed was maintained at 120 ℃ and the argon carrier flow rate equalled 500 sccm. The ferrocene flow rate can be varied by controlling the total pressure of the packed bed. For example, at a total pressure of ~81 kPa, a ferrocene flow rate of ~7 sccm is obtained.

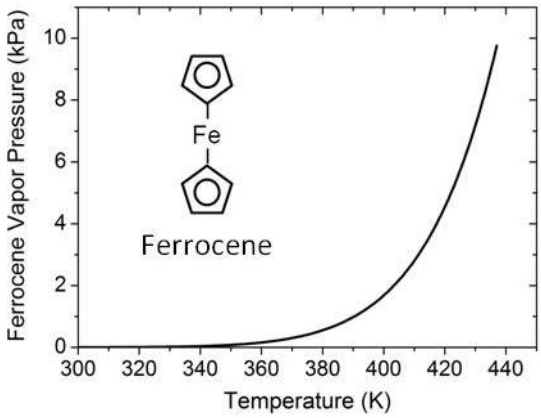

Figure 2.6 Equilibrium vapor pressure of ferrocene using Clark and Glew equation.

2.2.4 PRECURSOR DELIVERY

The ferrocene vapor was delivered by the argon carrier gas. In order to keep the ferrocene in gas phase to avoid condensation that can cause clogging, all delivery lines were heated to 125–145 ℃ by heating wires wrapped around the stainless steel tubes. Preliminary results showed that an additional preheated argon dilution flow of 1500 sccm injected downstream of the packed bed, as shown in Fig. 2.5, reduced the problem of clogging inside the ferrocene delivery lines.

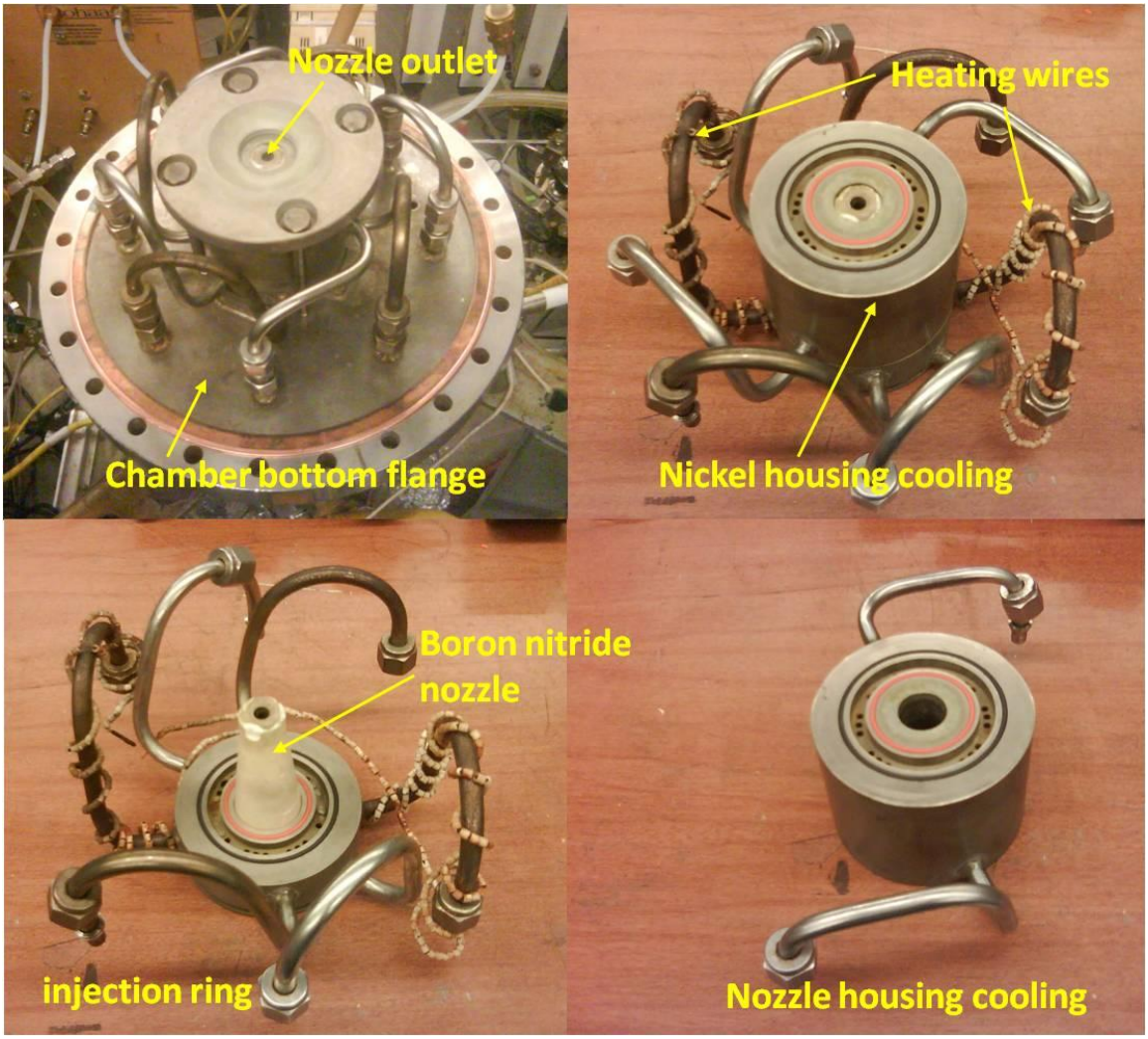

Figure 2.7 Ceramic nozzle and nickel-housing cooling configuration inside the chamber.

Further modifications were made along the delivery lines inside the chamber preceding injection into the plasma jet. Fig. 2.7 shows the ceramic nozzle and the nickel-housing configuration inside the plasma chamber. The ceramic nozzle was surrounded by a water-cooled nickel housing that consisted of two sections: an injection ring section and a nozzle cooling section. The injection ring section connects to three pairs of delivery lines: one for cooling water, one for precursor injection located at 9.5 mm downstream of

the nozzle entrance, and the other pair (not used) for additional precursor/gas injection located at 15.9 mm downstream of the nozzle entrance. These two pairs of gas injection holes are offset from each other by 90 °. The bent tubes used for ferrocene delivery were wrapped with heating wires, as shown in Fig. 2.7, to avoid ferrocene condensation.

Since the injection ring section was cooled by cold water, the pair of precursor injection holes was modified to keep the temperature high enough to prevent precursor condensation. The modification was developed by Bing Zhang [76]. A schematic of the modification is shown in Fig. 2.8. First, two water cooling holes were blocked at each side of the injection holes (Fig. 2.8(a)). Second, the injection hole was made of a thin, stainless steel insert (2-mm inner diameter), wrapped with flexible mica that has a much lower thermal conductivity than nickel and boron nitride, as shown in Fig. 2.8(b). The injection holes inside the ceramic nozzle were similarly modified, as seen in Fig. 2.9.

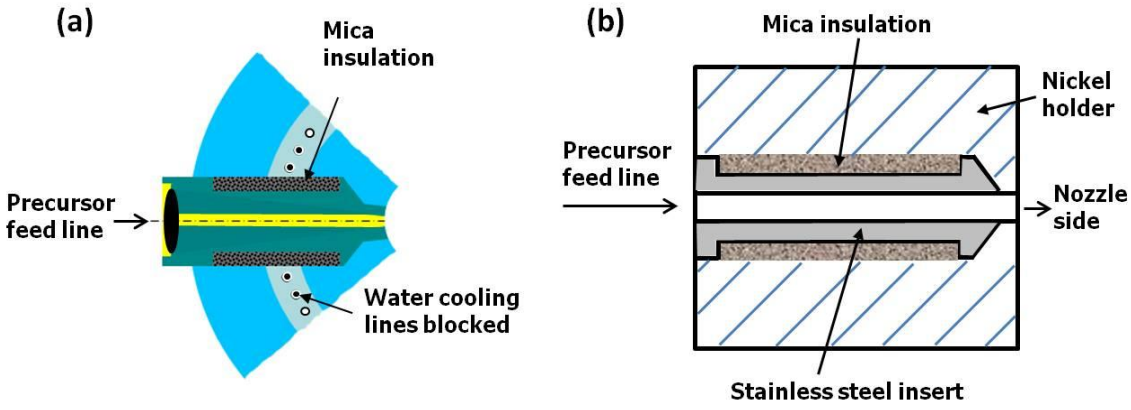

Figure 2.8 Modification of the precursor injection holes inside the injection ring, developed by Bing Zhang [76].

A schematic of the boron nitride nozzle is shown in Fig. 2.9, all dimensions are in millimeters. The outer contour of the nozzle follows Hansen's design [79] to achieve high

nozzle temperatures and to minimize the deposition of the particles on the internal wall surface of the nozzle. The total length of the nozzle is shortened to 75.4 mm. The outer diameter is 25.4 and 15 mm at the nozzle entrance and exit, respectively. The nozzle has two pairs of radial injection ports: one located at 9.5 mm, and the other located at 15.9 mm downstream of the nozzle entrance. In this study, only one pair of the upstream-end injection ports is used for ferrocene injection. According to Zhang's results [76], the inner diameter of the ferrocene injection port was modified to 2 mm to avoid clogging inside the holes. The internal contour of the nozzle, as seen in Fig. 2.9, follows the design modified by Gidwani [80] to eliminate the recirculation region inside the nozzle. The inner diameter is 5.65 mm at the nozzle entrance, 5.52 mm at the nozzle exit, and the largest inner diameter is 6.5 mm located at 19 mm downstream from the nozzle entrance.

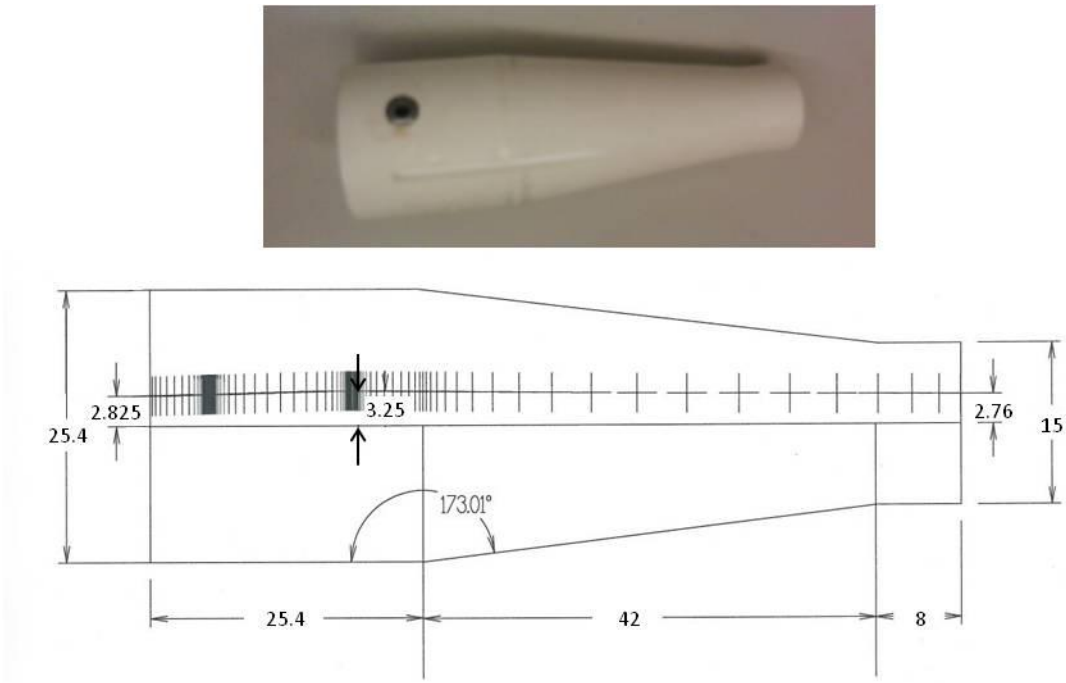

Figure 2.9 Boron nitride nozzle, all dimensions are in mm.

2.2.5 MATERIALS CHARACTERIZATION

The size distribution of plasma-synthesized particles was measured online by extracting aerosol with a sampling probe located in the reactor exhaust, using an ejector driven by high-pressure N_2, similar to the system described in [81]. The sampled aerosol was delivered to an SMPS system, as described in Chapter 1. Additionally, sampled particles were collected onto lacey carbon grids (Ted Pella 01890) located downstream of the neutralizer, using an electrostatic precipitator with an applied voltage of 3 kV. These samples were characterized by high-resolution transmission electron microscopy (HRTEM), conducted on a Tecnai G2 F30 electron microscope. Larger quantities of powder were collected on glass fiber filters inside the collector mounted in the reactor exhaust line. Chemical and phase composition were investigated using X-ray diffraction (XRD), performed with a Siemens D-500 diffraction meter with a 2.2 kW sealed cobalt source. Magnetic properties were characterized with a Princeton Micro Vibrating Sample Magnetometer (VSM) for room-temperature hysteresis loops, and with a Quantum Design magnetic property measurement system (MPMS), utilizing a Superconducting Quantum Interference Device (SQUID) magnetometer, for low-temperature measurements. To obtain zero-field cooling/field cooling (ZFC/FC) curves, the sample was initially cooled to 5 K in zero field, then the induced magnetization was measured under an applied field of 50 Oe while heating the sample to 300 K and then cooling it back to 5 K. Saturation isothermal remanent magnetization (SIRM) curves were obtained by saturating the sample in a 2.5 T field at 300 K, then recording the remanent

magnetization in zero field while cooling it from 300 to 20 K and then heating it back to 300 K.

2.3 Results and Discussion

2.3.1 Optimization of Experimental Conditions

Oxidation of ferrocene produces iron oxide, carbon dioxide, and water in the exhaust. Iron oxide nucleates and forms small nanoparticles as the temperature decreases in the flow direction. Preliminary experiments focused on optimizing the experimental conditions, such as plasma type, ceramic tube location, Ar quench flow rate, plasma power, and oxygen flow rate to achieve nanoparticles with good magnetic properties, for example high saturation magnetization and low coercivity.

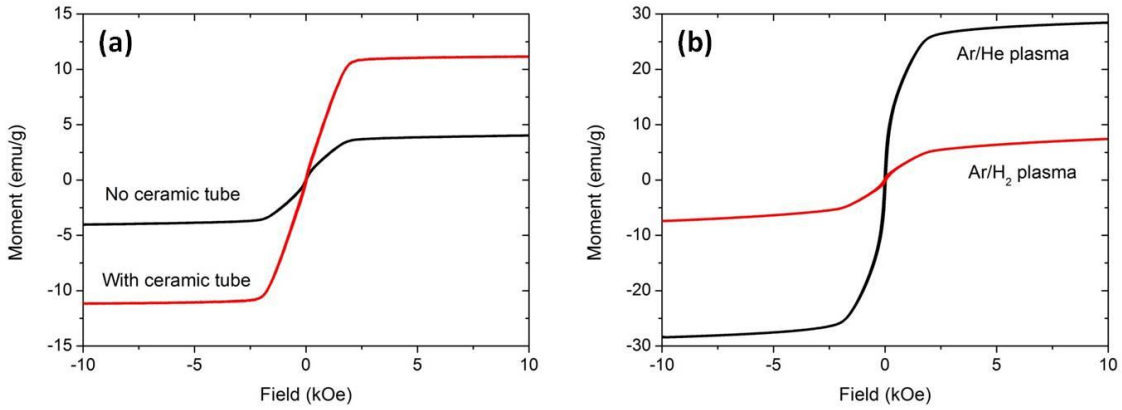

Figure 2.10 Hysteresis loops measured at room temperature: (a) Ar/H_2 plasma: 200 A, 0.5 slm H_2, ceramic tube located at ~5 cm above the nozzle exit; (b) comparing plasma type: 250A, 8 slm He, or 0.2 slm H_2, ceramic tube located at ~5 cm above the nozzle exit.

Fig. 2.10 shows magnetic hysteresis loops of synthesized nanoparticles collected on glass fiber filters. The ferrocene feeding rate was ~9 sccm and an additional O_2 of 200

sccm was used. Fig. 2.10(a) compares the results of two cases in Ar/H_2 plasma: with and without the ceramic tube. The plasma was run at a current of 200 A with 30 slm Ar and 0.5 slm H_2. The saturation magnetization was ~4.1 emu/g for the no ceramic tube case, and it increased to ~11.1 emu/g with the use of a ceramic tube positioned downstream of the plasma chamber, ~5 cm above the nozzle exit. The low values of achieved saturation magnetization compared to bulk magnetic iron oxides could be due to contamination inside the product, such as carbon and hematite. For the ceramic tube case, an increased saturation magnetization corresponds to a higher fraction of magnetic iron oxide phases (Fe_3O_4 or γ-Fe_2O_3) inside the product. This may be because wüstite can form in processes that experience rapid quench from high-temperature environments; a high temperature region with increased residence time provided inside the ceramic tube could help the transformation of the wüstite phase to the magnetic Fe_3O_4 phase [2].

Magnetic hysteresis loops for powder produced with two types of plasmas are compared in Fig. 2.10(b). In both cases, the plasma ran at a current of 250 A with an Ar flow rate of 30 slm; the ceramic tube was positioned ~5 cm above the nozzle exit; the plasma was kept at about the same power (7.5–7.7 kW) when 0.2 slm H_2 was used in an Ar/H_2 plasma and 8 slm He was used in an Ar/He plasma. The saturation magnetization measured by VSM was ~7.4 emu/g for the Ar/H_2 plasma, ~28.4 emu/g for the Ar/He plasma. For the same ferrocene and O_2 feeding rate, a higher saturation magnetization was obtained in the Ar/He plasma. This is probably because helium is a noble gas that does not react with O_2, while the hydrogen reacts with O_2, which may lead to less iron

oxidation and also the production of non-magnetic iron hydroxide phases. Thus, the ceramic tube and helium were used in later experiments.

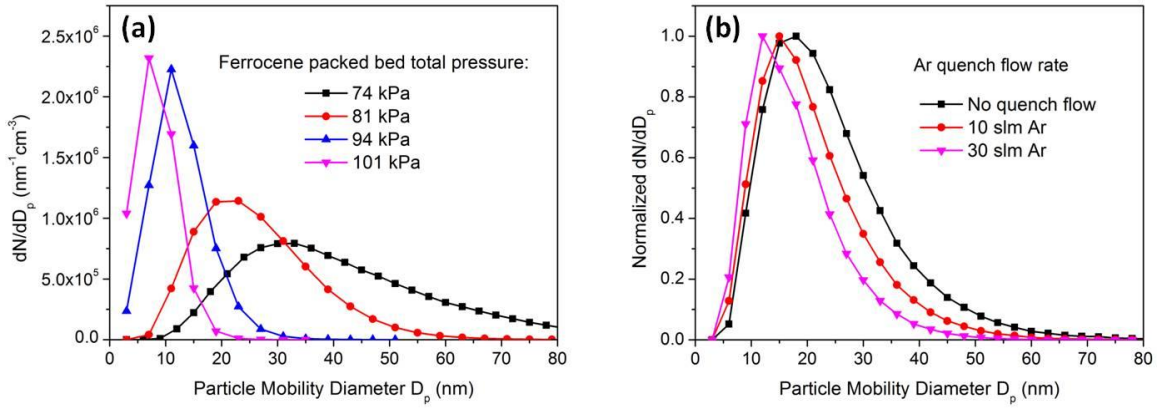

Figure 2.11 SMPS results of particle size distribution: (a) varying ferrocene packed bed total pressure: 8 slm He, 200 sccm O_2; (b) varying Ar quench flow rate: no He, 1.5 slm O_2, total pressure of ferrocene packed bed at 81 kPa.

Particle size distributions of plasma-synthesized nanoparticles were measured with SMPS. The plasma was operated at a current of 250 A with 30 slm Ar and 8 slm He. Argon carrier gas was kept at 500 sccm, and additional O_2 of 200 sccm was used. According to Equation 2.2, a lower total pressure leads to a higher ferrocene vapor flow rate. Fig. 2.11(a) shows that the size distribution shifts to larger sizes and becomes broader as the total pressure of the ferrocene packed bed decreased from 101 kPa to 74 kPa, indicating that the size of synthesized particles increased with the ferrocene vapor flow rate. Here, I need to point out that the particle diameter measured by SMPS is the mobility diameter of agglomerates, which may contain several primary particles. For the same ferrocene feeding rate (i.e., same total pressure of the precursor packed bed), the agglomerate size can be reduced by adding Ar quench flow into the downstream-end of the ceramic tube, as seen in Fig. 2.11 (b). The size distribution shifts to smaller diameters

and becomes narrower as the Ar quench flow increases from zero to 30 slm. This is because additional argon quench flow suppresses particle coagulation.

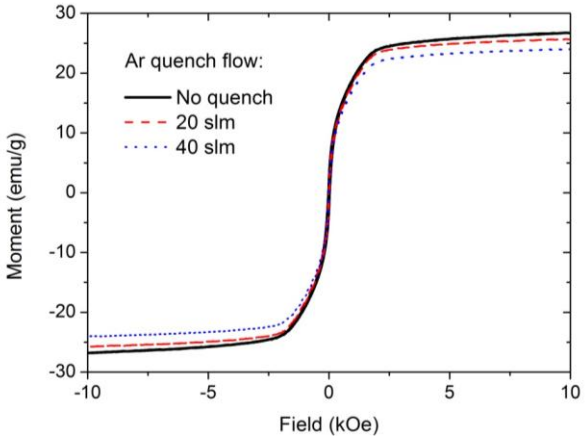

Figure 2.12 Hysteresis loops measured at room temperature, varying quench flow rate: plasma current of 240 A, 8 slm He, 200 sccm O_2, and ~9 sccm ferrocene.

Argon quench flow can reduce the agglomerate size, but it has little effect on magnetic properties of the particles produced. As seen in Fig. 2.12, three cases of Ar quench flow were investigated: 0, 20, and 40 slm. For the same plasma condition and precursor flow rate, the saturation magnetization of synthesized particles was about the same for all three cases, indicating that the chemical composition had not changed.

The position of the ceramic tube was also investigated to obtain particles with a high saturation magnetization. Fig. 2.13(a) shows the VSM measurements of hysteresis loops for particles produced with the ceramic tube positioned at 3, 5, and 7.5 cm above the nozzle exit. The plasma was run at a current of 250 A with 30 slm Ar, 8 slm He, ~9 sccm ferrocene vapor, and 200 sccm O_2. For the 3-cm case, the ceramic tube was close to the plasma jet. The saturation magnetization measured was ~9.5 emu/g. Inside the product, some grey powder was observed, indicating that the ceramic tube was too

close to the high temperature plasma jet and the ceramic tube was partially melted resulting in B_2O_3 contamination inside the product. The best saturation magnetization was achieved for the 5-cm case. Since the plasma jet temperature decreased rapidly when it expanded into the plasma chamber, the temperature inside the ceramic tube decreased as it moved farther away from the plasma jet. A lower saturation magnetization was observed for the 7.5-cm case indicating that the temperature inside the ceramic tube may have been too low for phase transformation of magnetic iron oxides.

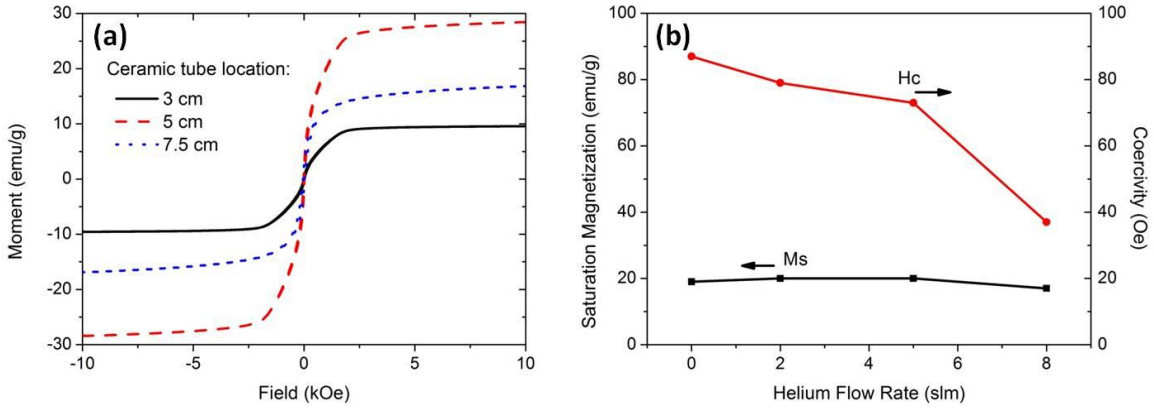

Figure 2.13 VSM results: (a) hysteresis loops, varying ceramic tube location: plasma current of 250 A, 8 slm He, 200 sccm O_2, 9 sccm ferrocene; (b) varying He flow rate: plasma current of 250 A, 200 sccm O_2, 9 sccm ferrocene, ceramic tube location 7.5 cm from nozzle exit.

Experiments were also carried out to study the plasma power effect on particle magnetic properties. The plasma power can be varied by controlling the plasma current and He flow rate. Preliminary results showed that when plasma current increased from 200 A to 250 A, the coercivity of synthesized particles decreased in the Ar/He plasma. For experiments described here, the plasma current was kept at 250 A, only the He flow rate was varied. Fig. 2.13(b) shows the effect of the helium flow rate on saturation magnetization (M_s) and coercivity (H_c) of synthesized nanoparticles. The plasma power

increased from 5.9 kW to 7.5 kW, as He flow rate increased from 0 to 8 slm. M_s of the synthesized particles was almost the same (a little bit decrease), while H_c decreased dramatically. Since coercivity increases with the single domain crystal size, a reduced H_c indicated that smaller crystallites were produced as the plasma power increased. In order to achieve superparamagnetism, H_c needs to be as small as possible (ideally zero).

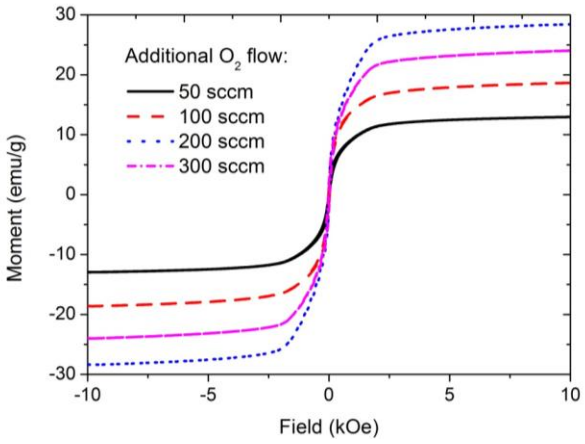

Figure 2.14 Hysteresis loops measured at room temperature, varying the O_2 flow rate.

Fig. 2.14 show the hysteresis loops of particles synthesized at a current of 250 A with 30 slm Ar and 8 slm He. The ferrocene feeding rate was kept constant at ~9 sccm, while the O_2 flow rate was varied. The VSM results show that the saturation magnetization increased as the O_2 flow increased from 50 sccm to 200 sccm, and then decreased as the O_2 flow further increased to 300 sccm. The best M_s was equalled ~28.4 emu/g. All hysteresis loops have a very small remanence and coercivity indicating superparamagentism of the plasma-synthesized nanoparticles.

All investigations showed that the Ar/He plasma with a high plasma power was favored for production of magnetic iron oxide with particles small enough to exhibit

superparamagnetic behavior; the use of a ceramic tube above the nozzle exit greatly improved the magnetic properties (i.e., saturation magnetization) of the powder produced; argon quench flow injected downstream of the ceramic tube was found to reduce particle agglomerate sizes, but it had little effect on the magnetic properties of the powder produced; and the oxygen flow rate was a dominant parameter affecting the magnetic properties. However, clogging was observed frequently in the ferrocene delivery lines. In order to reduce clogging, an Ar dilution of 1.5 slm was injected downstream of the ferrocene packed bed, as discussed previously, and the ferrocene feeding rate was also reduced from 9 sccm to 7 sccm by increasing the total pressure from 67 kPa to 81 kPa.

2.3.2 Optimum SPION Production

According to the optimization discussed above, the experimental conditions were modified as follows: the plasma was operated at a current of 250 A with 30 slm of Ar and 5 slm of He; the ceramic tube was fixed at ~5 cm above the nozzle exit, the total pressure of the ferrocene packed bed was maintained at ~81 kPa, and an argon dilution of 1.5 slm was introduced downstream of the packed bed. With the additional argon dilution, a total mixture flow of ~2 slm was achieved, resulting in a deeper penetration into the central high temperature region of the plasma jet. Thus, more atomic oxygen was produced for the ferrocene reaction, and the color change of the powder produced was observed at a smaller oxygen flow rate than in the experiments without additional Ar dilution,

discussed below. Further experiments focused on the effects of the oxygen flow rate on chemical, physical, and magnetic properties of nanoparticles produced.

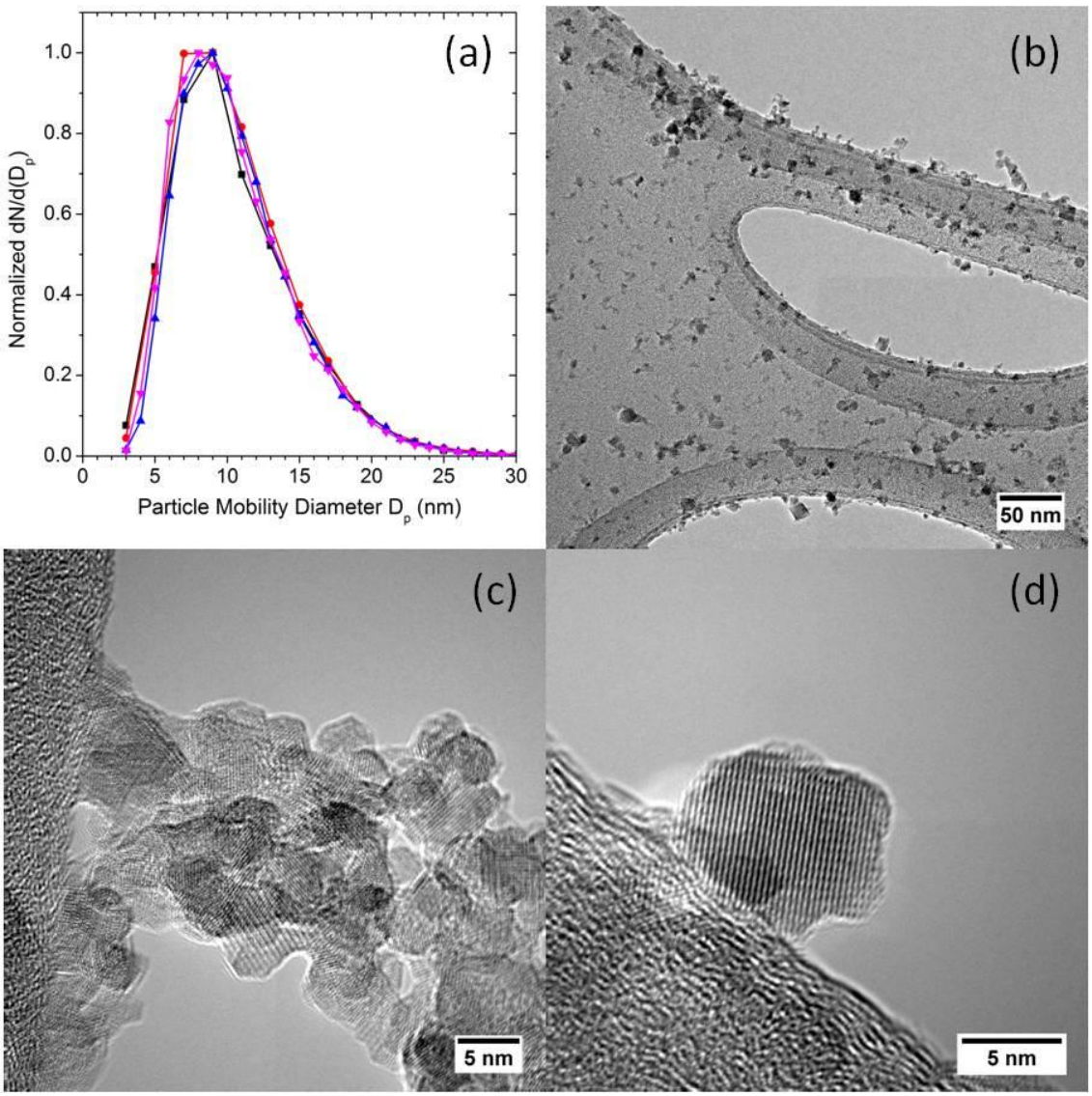

Figure 2.15 Aerosol sampled from reactor exhaust at oxygen flow rate of 20 sccm: (a) particle size distributions measured by SMPS (different symbols correspond to different voltage scans of the differential mobility analyzer); (b) low-resolution TEM image; (c, d) high resolution TEM images. Large structure in TEM images is TEM grid.

Figure 2.15 shows particle mobility diameter distributions measured with SMPS, and TEM images of particles sampled for the same set of conditions, for an oxygen flow rate of 20 sccm. As seen in Fig. 2.15(a), the measured size distributions for a given set of run conditions showed good reproducibility. For the case shown, the results indicate the mode in the size distribution of ~8 to 9 nm, a maximum agglomerate size around 30 nm, and a geometric standard deviation of ~1.49, close to the ~1.45 value expected for a coagulating aerosol [82]. Fig. 2.15(b) shows a corresponding low-resolution TEM image, and Fig. 2.15(c) and (d) show two HRTEM images. Note that the agglomerate structures seen in Fig. 2.15(b) and (c) were not necessarily formed in the aerosol phase, as loose agglomerates can form during deposition on the TEM grid. Nevertheless, as the HRTEM images show that individual crystallites are smaller than 10 nm, it is evident that the mobility diameter distributions seen in Fig. 2.15(a) represent a mixture of isolated crystallites together with small agglomerates. Fig. 2.15(d) clearly shows the lattice fringes of a single iron oxide nanoparticle. The d-spacing measured in the image equals ~0.30 nm, corresponding to the magnetite (022) or the maghemite (220) planes.

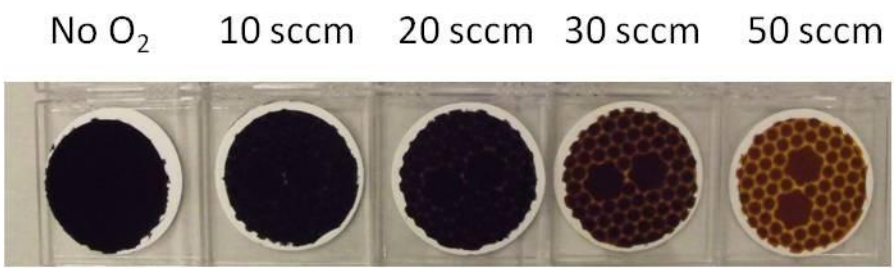

Figure 2.16 Particles collected on glass fiber filters.

Fig. 2.16 shows the color change of the synthesized powder collected on glass fiber filters with varying oxygen flow rate. For the zero and 10 sccm cases, the powder is black, which may be due to carbon contamination produced at a low O_2 flow rate. Then the color becomes dark brown for the 20-sccm case, and slowly turns to red-brown as the O_2 flow rate increases, indicating that more hematite is formed in the product at higher O_2 flow rate.

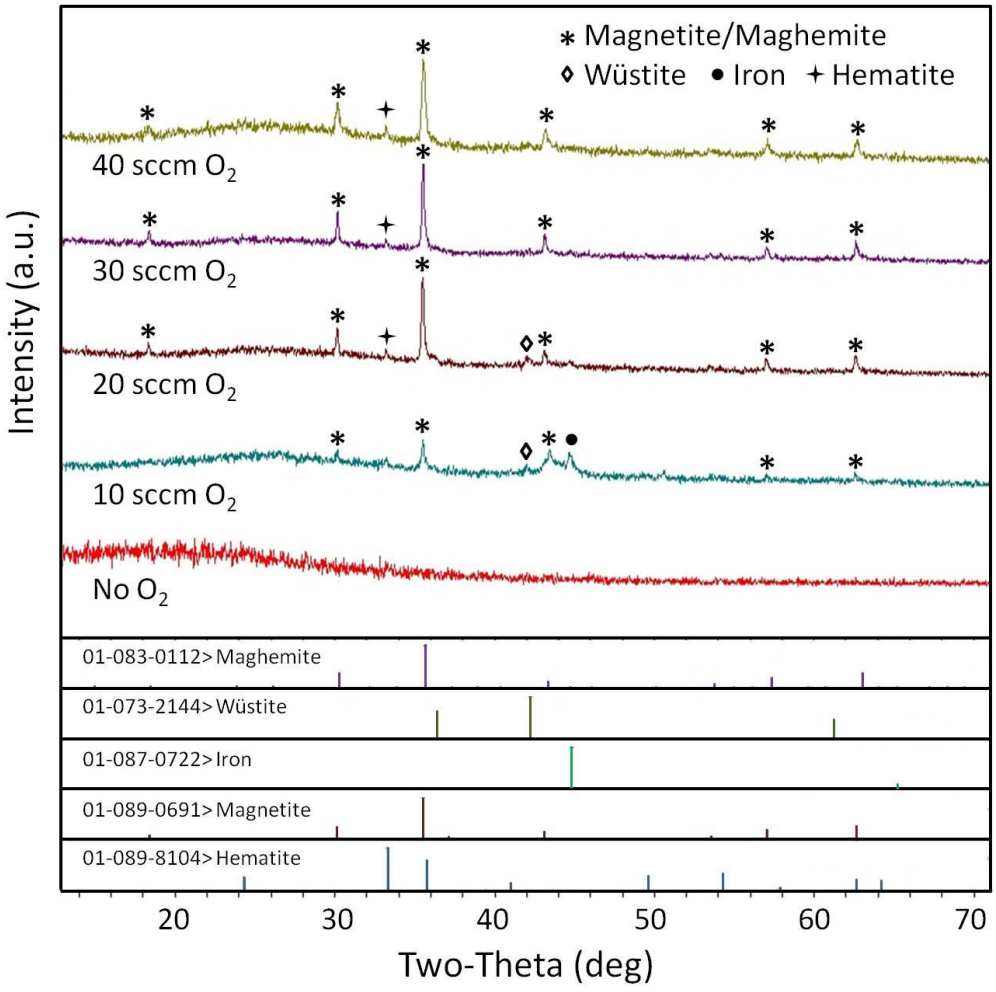

Figure 2.17 X-ray diffraction patterns of powder collected on glass fiber filters located in reactor exhaust, for various flow rates of oxygen. Patterns were analyzed using JADE 9 software (Materials Data, Inc).

Figure 2.17 shows measured XRD patterns of powder collected on glass fiber filters for various oxygen flow rates. As the flow rate of oxygen increases from 0 to 30 sccm, the XRD patterns show a clear trend toward increasing oxidation.

For the case where no additional oxygen was added to the plasma, no crystalline signal is detected in the XRD pattern. Instead, the pattern in this case is mainly indicative of amorphous carbon. Although the thermal plasma is expected to break the Fe–C bonds in the ferrocene precursor, the presence of sufficient oxygen is evidently necessary to prevent the condensation of carbonaceous material.

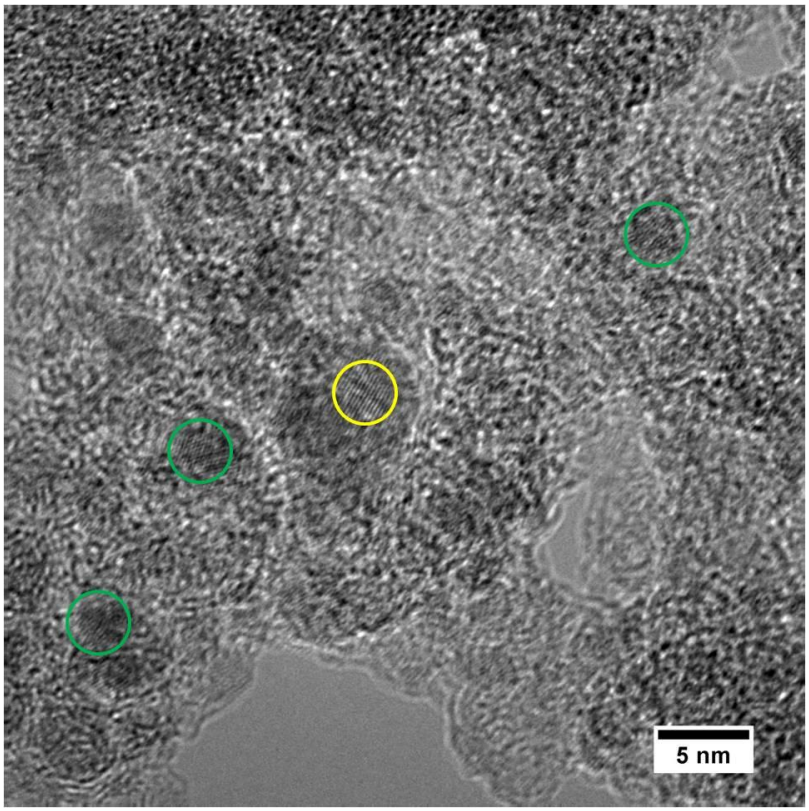

Figure 2.18 HRTEM image of sample for case of zero oxygen flow. Circles highlight several regions with evident crystalline lattice fringes.

An HRTEM image for the zero-oxygen case is shown in Fig. 2.18. The material appears to be mainly amorphous, consistent with the XRD pattern, but one also sees isolated areas of lattice fringes, from crystallites that are only a few nm in size. The d-spacing of the crystallite highlighted in the center of the image measures ~0.21 nm. Within the uncertainty of the measurement, it could represent either the (110) plane of Fe (0.2027 nm), the (004) plane of magnetite (0.2096 nm), or the (400) plane of maghemite (0.20869 nm). The small size of these crystallites, together with their being embedded in an amorphous carbon matrix, may explain the absence of evident peaks in the XRD pattern.

In cases where oxygen was added to the gases injected into the plasma, at flow rates ranging from 10 to 40 sccm, crystalline peaks appear in the XRD patterns of collected powder, as seen in Fig. 2.17. At an O_2 flow rate of 10 sccm, the XRD pattern shows peaks associated with pure Fe, wüstite, and magnetite and/or maghemite. Note that magnetite and maghemite have the same cubic spinel structure and quite similar lattice parameters (magnetite a = 0.8396 nm, maghemite a = 0.83474 nm) [2], as a result of which their dominant XRD peaks are effectively indistinguishable.

At an oxygen flow rate of 20 sccm, the pure Fe peak almost disappears, while the peaks associated with magnetite and/or maghemite show increased intensity. The wüstite peak remains (though much smaller relative to the magnetite/maghemite peaks than in the 10-sccm case) and a small peak associated with hematite appears. With further increases in the oxygen flow rate, to 30 and 40 sccm, the wüstite peak disappears. The powder is predominantly magnetite and/or maghemite, with a small component of hematite. The

hematite phase is antiferromagnetic, which decreases the average saturation magnetization of the products.

Hysteresis loops measured by VSM at room temperature with a maximum applied field of 1.5 T are shown in Fig. 2.19(a) for cases that correspond to the XRD patterns shown in Fig. 2.17. Magnetic moments were normalized in each case by the total sample mass collected on the glass fiber filters. All the curves show nearly zero hysteresis, indicating that the particles are superparamagnetic [47, 83], and approach their saturation values rapidly, with the exception of the case with an oxygen flow rate of 10 sccm. The saturation magnetization and coercivity determined from these measurements are summarized in Fig. 2.19 (b) and (c).

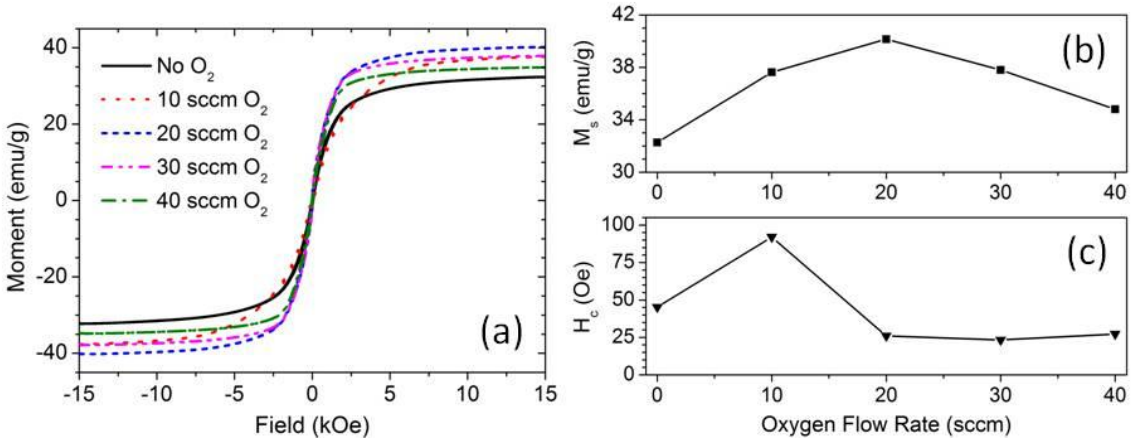

Figure 2.19 Vibrating sample magnetometer measurements at room temperature of collected powder samples for various oxygen flow rates: (a) hysteresis loops; (b) saturation magnetization (M_s); (c) coercivity (H_c).

The results for the zero oxygen case, which show a surprisingly high saturation magnetization of 32.3 emu/g, with a coercivity measuring 45 Oe, suggest that the crystallites seen in Fig. 2.18 are primarily pure Fe. The saturation magnetization of bulk

iron, 222 emu/g [84], is much higher than that of either magnetite (92–100 emu/g) or maghemite (60–80 emu/g) [2], and the crystallites seen in Fig. 2.18 are smaller than the 8-nm superparamagnetic critical size for Fe. This hypothesis is further supported by the Fe peak in the XRD pattern, Fig. 2.17, for the 10-sccm case, since if pure Fe particles are formed in the 10-sccm oxygen case, then they are even more likely to form in the zero-oxygen case. The much higher coercivity in the 10-sccm case, ~90 Oe, can plausibly be explained by the fact that growth of the Fe particles in the zero-oxygen case is constrained by their encapsulation in an amorphous carbon matrix, whereas there is much less carbon inclusion with added oxygen, allowing the Fe particles to grow larger than 8 nm. Although magnetite and maghemite particles are superparamagnetic up to 20 nm, the presence of a relatively small fraction of Fe particles larger than 8 nm would cause a significant increase in coercivity.

The highest measured saturation magnetization, 40.15 emu/g, was achieved at an oxygen flow rate of 20 sccm. The coercivity and remanence for this sample measured 26 Oe and 1.5 emu/g, respectively, meaning that the powder is almost completely superparamagnetic. The fact that the saturation magnetization is lower than the values for bulk magnetite and maghemite may be due to the presence of a small fraction of hematite, as indicated by the XRD pattern, hematite being antiferromagnetic [2], and/or to the frequently observed, and theoretically predicted, strong reduction in saturation magnetization for superparamagnetic particles as crystallite size decreases [85-88]. However a recent study [89], which involved wet chemical synthesis of ~5-nm-diameter magnetite particles that were subsequently coated with a thin layer of organic film and

then gold, reported a very high M_s of 81 emu/g, suggesting that the effect of particle size on M_s may actually be due to impurities on the particle surfaces, which become more important as particle size decreases.

As the oxygen flow rate increases above 20 sccm, Fig. 2.19(b) shows that the saturation magnetization decreases, while the coercivity, shown in Fig. 2.19(c), is basically unchanged. We hypothesize that this behavior is due to increasing oxidation of the superparamagnetic particles from magnetite to maghemite. As noted above, the bulk saturation magnetization of maghemite is lower than that of magnetite. From the XRD patterns in Fig. 2.17, the small peak at 33.28 ° attributed to hematite is essentially unchanged as the oxygen flow rate increases from 20 to 40 sccm, indicating that the increased oxidation occurs between the two superparamagnetic phases, and therefore, does not affect the coercivity. Also supporting this hypothesis, as the oxygen flow rate increases the color of the synthesized powder, as observed by the naked eye, changes from black at 0 sccm to dark brown at 20 sccm, to brown at 30 sccm, and to reddish brown at 40 sccm.

Hysteresis loops of plasma-synthesized iron oxide nanoparticles measured at room temperature (by VSM), and at 10 K (by MPMS) for the case of 20-sccm oxygen are compared in Fig. 2.20. At room temperature the hysteresis loop is nearly reversible, with almost zero hysteresis. At 10 K, a small increase of the saturation magnetization is observed, to ~43 emu/g compared with ~40 emu/g at room temperature, while the coercivity dramatically increases, to ~330 Oe compared with ~26 Oe at room temperature. This behavior is expected, as the thermal energy at 10 K is not sufficient to reverse the

magnetization when the field is reduced to zero. At 10 K, these particles are blocked and behave like ferrimagnetic materials, with an increased remanence and coercivity, as seen in Fig. 2.20.

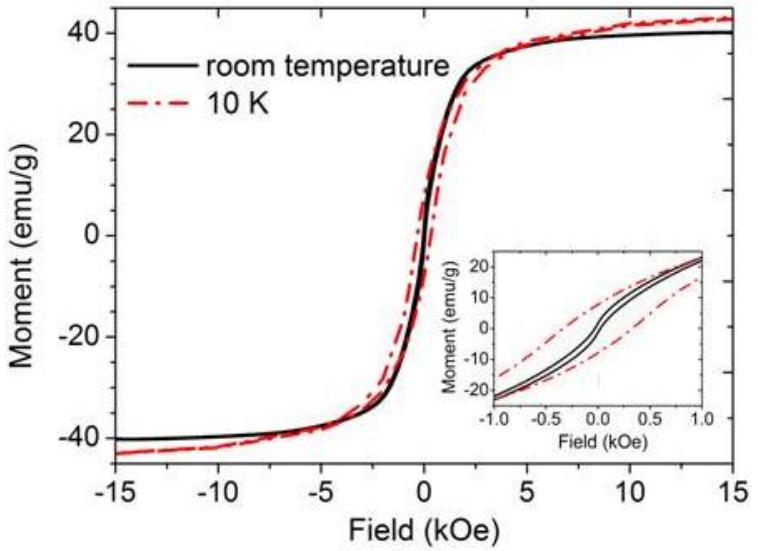

Figure 2.20 Hysteresis loops measured at both room temperature and 10 K, for powder sample synthesized at oxygen flow rate of 20 sccm.

To provide further information about the magnetic properties of the powder produced in the 20-sccm oxygen case, zero-field cooling/field cooling curves were measured by MPMS with a field of 50 Oe, shown in Fig. 2.21(a), and room-temperature saturation isothermal remanent magnetization (SIRM) measurements were obtained, as shown in Fig. 2.21(b). The abrupt change in the magnetic moments for both the cooling and warming curves in Fig. 2.21(b), as well as the sharp change in the slopes of the ZFC/FC curves in Fig. 2.21(a), both of which occur around 120 K, corresponds to the known Verwey transition of magnetite, whose equilibrium structure is cubic above the Verwey temperature $T_V \approx 120$ K, and monoclinic below T_V [90, 91]. As no corresponding

phase transition occurs in maghemite, these measurements indicate that the sample is substantially composed of magnetite, although the additional presence of maghemite cannot be ruled out. Indeed, the fact that the transition in the curves seen in Fig. 2.21(b) is relatively broad rather than sharp could be due to some degree of maghemitization of the magnetite nanoparticles [92].

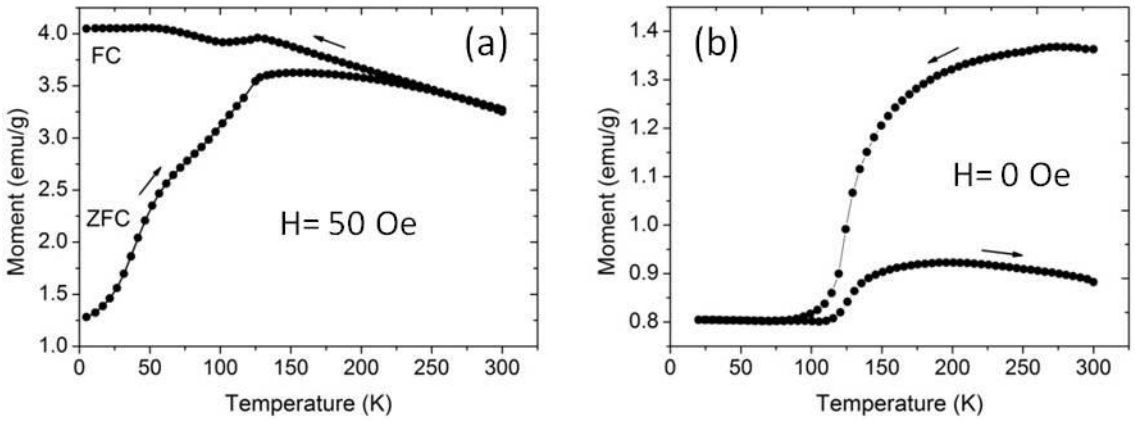

Figure 2.21 Saturation isothermal remanent magnetization measurements of powder sample synthesized at an oxygen flow rate of 20 sccm: (a) zero-field-cooling/field-cooling measurements; (b) zero-field cooling and rewarming measurements.

Additionally, the temperature where the ZFC and FC curves in Fig. 2.21(a) separate, around 250 K, can be equated to the blocking temperature T_B of the largest crystallites in the sample [93]. At temperatures below T_B the thermal energy is insufficient to overcome the magnetic anisotropy energy of the nanoparticles, preventing superparamagnetism. The crystallite volume V can be estimated by

$$V = \frac{25 k_B T_B}{K_{eff}} \tag{2.3}$$

where K_{eff} is the effective magnetic anisotropy constant, and k_B is the Boltzmann constant [94]. Using $K_{eff} \approx 5\times10^4$ J/m for magnetite [2, 95], and assuming spherical crystallites, the largest crystallite diameter estimated by Equation 2.3 equals ~15 nm. Note that most crystallites are considerably smaller than this, as evidenced by both the SMPS measurements (which include agglomerates) and the TEM images in Fig. 2.15. Thus, essentially all of the crystallites are below the ~20-nm critical size for superparamagnetism in magnetite and maghemite.

In any case, the magnetic properties obtained in this study are far superior to those reported for any previous plasma synthesis of SPIONs, as reviewed in the "Background" section. There are several possible explanations for these improved results compared to other studies of plasma synthesis of iron oxide nanoparticles. The precursors in our system are injected into the plasma at the upstream end of a hot-wall converging nozzle, producing a relatively uniform environment for vapor mixing and particle nucleation [96]. A long ceramic tube at the exit of the reactor additionally provides a relatively uniform high-temperature environment, and the total residence time, a few tens of ms, is too short to allow for crystallite growth beyond the superparamagnetic critical size. Further, our study shows that careful control of the oxygen-to-ferrocene ratio is crucial for control of the stoichiometry and phase of the particles produced.

A number of studies have also reported flame synthesis of SPIONs [50, 88, 97-102]. Among these, the best magnetic properties achieved appear to be the recent results of Kumfer et al. [102]. In a series of five experiments with various flame conditions, their measured values of room-temperature saturation magnetization increased monotonically

with coercivity, with values of M_s ranging from 6.5 to 60 emu/g, as values of H_c ranged from 13 to 76 Oe. They attributed increases in M_s both to increases in particle size and to the presence of a significant fraction of pure Fe in the sample with the highest M_s, and increases in coercivity to an increasing fraction of particles above the critical size for superparamagnetism. The sample that lay in the middle of their results, with M_s = 42 emu/g and H_c = 30 Oe, is virtually identical to the results for our case of the 20-sccm oxygen flow case, for which we obtained M_s = 40.15 emu/g and H_c = 26 Oe. As in this study (see below), the powder samples consisted primarily of Fe_3O_4. This is in contrast to the more typical result that flame synthesis, with its inherent abundance of oxygen, tends to produce γ-Fe_2O_3 [50, 97-99]. To produce magnetite, with its higher saturation magnetization than maghemite, Kumfer et al. [102] ran under more reducing conditions than in the typical flame.

2.4 SUMMARY

A DC thermal plasma system was used to synthesize superparamagnetic iron oxide nanoparticles, using ferrocene vapor as the iron precursor. Preliminary results found that the magnetic properties of the synthesized particles were strongly affected by the plasma type, plasma power, and ceramic tube position placed above the nozzle exit. Particles with higher saturation magnetizations were obtained in an argon/helium plasma. Increasing the plasma power, by both increasing the plasma current and helium flow rate, tended to decrease the particle coercivity. The particle size distribution decreased as the

ferrocene precursor feeding rating decreased. Argon quench flow injected downstream helped to decrease the agglomerate size, but it had little effect on the magnetic properties.

Optimum SPIONs were produced in an argon/helium plasma with the ceramic tube positioned ~5 cm above the nozzle exit. An additional argon dilution flow of 1.5 slm was injected downstream of the precursor packed bed to reduce clogging. The chemical and phase composition of produced product depended on the flow rate of oxygen added to the plasma. At zero oxygen flow rate, the powder produced consisted of 2–3 nm Fe crystallites in an amorphous carbon matrix. As the oxygen flow rate increased, the iron was increasingly oxidized. For the oxygen flow rate where the best magnetic properties were achieved, the powder consisted primarily of magnetite (Fe_3O_4), with possible contributions of maghemite (γ-Fe_2O_3), as well as a small fraction of hematite (α-Fe_2O_3). The mode in the particle mobility diameter distribution measured by SMPS equalled 8–9 nm. SMPS measurements and TEM images indicate that the material produced consisted both of single crystallites and small agglomerates, with a maximum agglomerate size of ~30 nm and a maximum crystallite size, determined by SQUID magnetometry, of ~15 nm.

Superparamagnetism was observed in the collected powder for most of the oxygen flow rates tested. The best room-temperature saturation magnetization measured equalled 40.15 emu/g, with a coercivity of 26 Oe and a remanence of 1.5 emu/g. These results are the best yet reported, from the viewpoint of high saturation magnetization with negligible coercivity, for synthesis of SPIONs by any type of plasma, and are comparable to the best results reported to date for flame synthesis.

Chapter 3 Silica Coating on Iron Oxide Nanoparticles

3.1 BACKGROUND

Silica has been widely used in biomedical applications, such as drug delivery [103-109], due to its biocompatibility [109-111]. Because of its high chemical and thermal stabilities, silica has also been considered a promising coating material for stabilizing quantum dots [112-115] and metal particles, such as silver particles [43, 116-118], gold particles [119-122], and magnetic iron oxide nanoparticles [50, 123-126]. The silica not only suppresses the coagulation process (i.e., coalescence of cores) and other undesired effects of the core particles but also provides additional surfaces for further bio-functionalization to achieve multiple functions serving both for diagnostic and therapeutic applications [127-133].

The most frequently used approaches for synthesizing silica coatings are the Stöber method [118, 119, 134-137] and microemulsion processes [138-142] using wet chemistry. However, most of the wet-chemistry studies for synthesis of silica coatings showed a thick silica layer on nano-sized particles [118, 119, 134, 140-142], and it was difficult to grow thin silica coatings (e.g., < 2 nm) on small nanoparticles. Gas-phase approaches have gained intense interest for deposition of thin films, especially when the core particles are synthesized in the gas-phase [42, 43]. The coating process can be accomplished in a continuous gas stream without separating and transferring the intermediate products during the synthesis processes. Contamination due to separation

and transfer steps can be avoided and the production yield can be greatly improved compared to batch processes using wet-chemistry approaches. Moreover, the use of online characterization techniques in the gas-phase approaches has advantages in terms of chemical composition and coating thickness control.

Normally, gas-phase approaches for synthesizing silica films and coatings include thermal chemical vapor deposition (thermal-CVD) [50, 97, 98, 143-145] and plasma-enhanced chemical vapor deposition (PECVD) [143, 146-153]. For the thermal–CVD approach, the silica precursor, such as tetraethylorthosilicate (TEOS, $Si(OC_2H_5)_4$), decomposes at high temperature in the presence of O_2, and condenses on the substrate or nanoparticle surfaces to form silica films. The control of both the temperature and the partial pressure of the silica precursor are critical for producing uniform films and avoiding the homogeneous nucleation of silica. In the PECVD processes, silica precursors, such as silane (SiH_4) [143, 146, 147] and tetraethylorthosilicate [148-150], dissociate in the plasma and react with oxygen species dissociated from O_2 or N_2O, to form silica films by means of chemical vapor deposition. The PECVD process can achieve a higher deposition rate than the thermal-CVD at a much lower temperature. However, vacuum systems are usually required for PECVD, and the deposition processes are sensitive to the plasma power density, frequency, temperature, and pressure.

Another gas-phase approach for synthesis of silica films is photo-induced chemical vapor deposition (photo-CVD), which has received considerable interest for decades [154]. The high-energy photons generated from lasers or ultraviolet lamps initiate or enhance chemical reactions of the precursor vapor, including the formation of

thin films on the surface of the substrates or nanoparticles. The use of energetic photons greatly reduces the required temperature for the deposition processes. Bergonzo et al. reported formation of silicon dioxide films by photo-induced chemical vapor deposition of silane in N_2O or O_2 gases using a 172-nm Xenon excimer lamp [155, 156]. This process has also been investigated by González et al. in a gas mixture of Ar diluted with N_2O and SiH_4 [157]. Awazu et al. demonstrated synthesis of amorphous SiO_2 films from tetramethoxysilane (TMOS) with excimer lamps of energy higher than 7.2 eV [158, 159]. Kurosawa et al. used TEOS as the silica precursor and investigated the deposition process with ultraviolet (UV) lamps of 308 (XeCl), 222 (KrCl), 172 (Xe_2*), 146 (Kr_2*) and 126 nm (Ar_2*) [160]. They found that silica film deposition was only observed at wavelength $\leq$ 172 nm and addition of O_2 to TEOS induced inhibition of C and H impurity inclusion in the films. Continued work by Yokotani et al. also confirmed the silica film formation using TEOS with Xe_2* (172 nm) and Ar_2* (126 nm) excimer lamps [161]. They also found that the photochemical reaction of adsorbed fragments with VUV radiation on the surface of the substrate is the main reaction for the formation of SiO_2.

Zhang et al. have reported the production of polymer coatings on different sizes of sodium chloride and aluminum nanoparticles at atmospheric pressure and room temperature via photo-CVD using a Xenon excimer lamp that irradiates at 172-nm wavelength [42, 76]. They found that the coating thickness could be controlled from sub-nanometer to 20 nm by varying the flow rate of the carbon precursor, such as methyl methacrylate (MMA). Boies et al. obtained similar results for silica coating on silver nanoparticles using TEOS as the silica precursor [43]. They studied the silica coating

quality with varying coating temperatures and found that silica films with high purity were generated at 300–400 ℃, and additional O_2 gas helped to reduce the C impurities inside the films.

To the best of my knowledge, nobody has studied the photo-CVD approach for synthesis of silica coatings on iron oxide nanoparticles. In this chapter, I develop a photo-CVD process for fabricating core-shell structured silica-coated superparamagnetic iron oxide (SPIO@SiO_2) nanoparticles. The dielectric silica coating will help to reduce the coalescence of the superparamagnetic iron oxide core, and prevent further oxidation to keep the magnetic properties. Furthermore, the silica surface can be readily attached to other functional groups for further surface modification of the core-shell structured nanoparticles. The whole synthesis process was in gas phase and the final products were analyzed by both online and offline techniques.

3.2 Experimental Procedure

In order to synthesize silica coating on iron oxide nanoparticles, a two-step gas-phase method was used. In the first step, the iron oxide nanoparticles were produced by an argon/helium thermal plasma, as described in Chapter 2. Then the silica was synthesized by photo-induced chemical vapor deposition inside a CVD furnace/chamber. The iron oxide aerosol nanoparticles produced from the plasma chamber were sampled directly into the coating chamber without exposure to air.

3.2.1 EXPERIMENTAL SETUP

The setup for the experiments in which silica-coated superparamagnetic iron oxide nanoparticles are synthesized is shown in Fig. 3.1. Superparamagnetic iron oxide nanoparticles were produced by a DC thermal plasma, then introduced into a photo-induced chemical vapor deposition chamber for silicon dioxide coating. The thermal plasma condition used to produce SPIO cores for silica coating was set to achieve the best magnetic properties of the magnetic iron oxide nanoparticles as discussed in Chapter 2. The thermal plasma was run at 250 A with a mixture of argon (30 slm) and helium (5 slm) gases. Ferrocene vapor (~7 sccm) was injected into the plasma jet with 500 sccm of argon passing through the precursor packed bed, which was controlled at 120 ℃ by a heating mantle. An additional 1500 sccm argon dilution was added after the precursor packed bed to reduce clogging in the delivery line and 20 sccm of oxygen was also injected for making iron oxide nanoparticles. All delivery lines were kept at 125–145 ℃ to avoid ferrocene vapor condensation before reaching the plasma jet. The pressure of the plasma chamber was kept at ~51 kPa. Iron oxide aerosol particles were sampled downstream of the plasma chamber into the CVD chamber (Lindberg/Blue STF553463) by a nitrogen-driven Venturi pump operating at ~400 kPa.

The temperature of the CVD chamber was kept at 300 ℃ to obtain high quality silica coating [43]. The Xenon excimer lamp (USHIO, model UER20H-172) emits UV light at a wavelength of 172 nm with an irradiation window of 35.5 mm in diameter and an output power of 50 mW cm^{-2}. The energy of the UV photons (~7.2 eV) is high enough to dissociate the TEOS precursor. The precursor vapor was injected by the N_2 carrier gas

bubbling through a liquid TEOS bubbler which was maintained in a water bath at room temperature. Nitrogen of 5 slm was used for lamp cooling. A CaF_2 window (38 mm × 5 mm, purchased from KOCH Crystal Finishing), which is transparent to the UV light, separates the CVD chamber and VUV lamp chamber. A pair of additional gas delivery lines located next to the CaF_2 window was used to inject N_2 purge flow into the CVD chamber. The N_2 purge flow not only keeps the CaF_2 window clean for particle deposition, but also helps to control the residence time inside the CVD coating chamber.

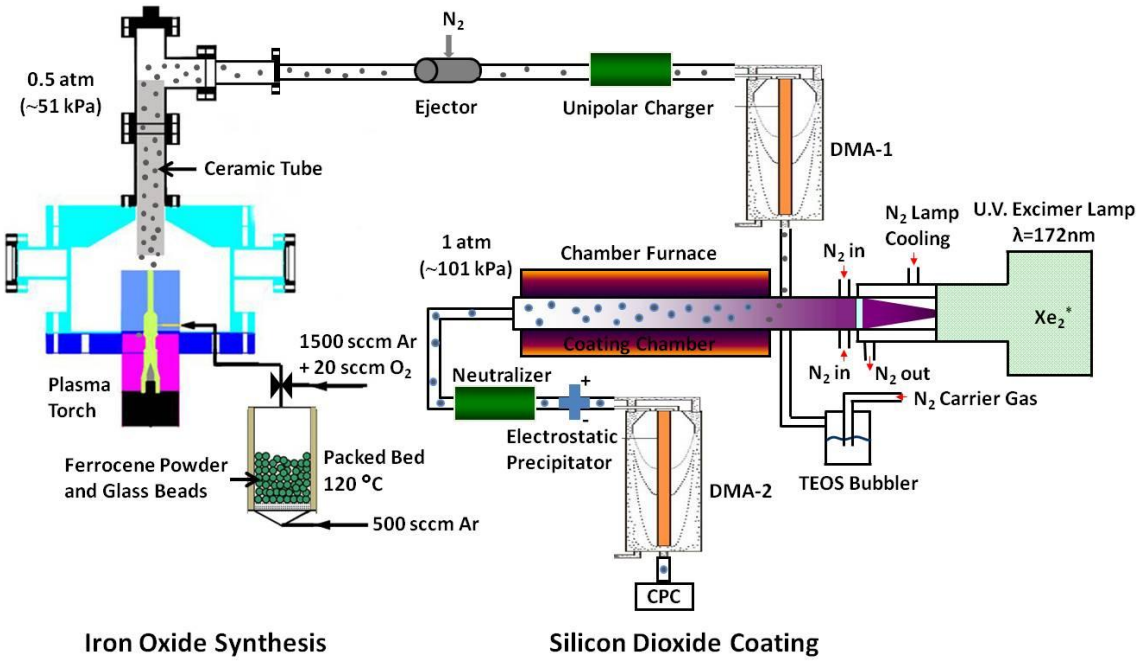

Figure 3.1 Experimental setup for synthesis of silica-coated iron oxide nanoparticles.

An online tandem differential mobility analyzer system was used to study the effects of the experimental parameters, such as TEOS and N_2 purge flow rate, on the coating process. The first DMA was used to size-select plasma-synthesized iron oxide particles to get monodisperse core particles to pass into the coating chamber. The second

DMA together with the CPC, also called the scanning mobility particle sizer (SMPS) system, as described in Chapter 1, scanned the size distribution of the particles after the CVD chamber. The size distributions measured by the second DMA were fitted by Gaussians in Origin 8.1 (Origin Lab). Half of the diameter shift in the peak of the distribution corresponds to the thickness of the silica coating.

Radioactive chargers (Po-210) are used before the DMAs to charge the aerosol particles. Since iron oxide nanoparticles produced from the thermal plasma have a narrow size distribution, with particle sizes smaller than 20 nm, a unipolar charger was used before the first DMA for particle size selection. The unipolar charger, developed by Chen and Pui [162], consists of four sections: the inlet, the ion production, the unipolar charging, and the exit zones. Bipolar ions are produced by radioactive Po-210 sources in the ion production zone, and a DC electric field applied in the ion production and charging zones is used to select and focus unipolar ions for the charging section. Chen and Pui showed that the designed unipolar charger charges nanoparticles more efficiently than bipolar charger. Thus, the unipolar charger was chosen as the particle charger before the first DMA. The normal TDMA setup does not require a second charger before the second DMA. However, the UV light could change the charge state of the particles inside the CVD chamber. Details of the UV effect are discussed below in Section 3.2.3. In this case, a bipolar charger (neutralizer) was placed in line to recharge the coated particles before they entered the second DMA.

Silica-coated iron oxide nanoparticles were collected on lacy carbon TEM grids (Ted Pella 01890) using an electrostatic precipitator with an applied voltage of 3 kV

located after the neutralizer. These samples were characterized by high-resolution transmission electron microscopy (HRTEM, Tecnai G2 F30). Silica coating thickness was measured online by the TDMA and SMPS systems, as described in Chapter 1. The surface chemistry of the silica-coated iron oxide nanoparticles was analyzed by Fourier transform infrared spectroscopy (FTIR, Nicolet Magna 550), with particles collected on stainless steel mesh (400 × 400). Magnetic properties of the collected powder were characterized with a Princeton Micro Vibrating Sample Magnetometer (VSM) with measurements made at room temperature.

3.2.2 UNIPOLAR AND BIPOLAR CHARGER

In order to study the charging efficiency of the unipolar and bipolar chargers, polydisperse iron oxide aerosols of 1 slm were sampled into the TDMA system and a sheath flow of 10 slm N_2 gas was used. The CVD chamber was set at 300 ℃. The UV lamp was off and no TEOS precursor was injected. Comparison of the TDMA particle counts using unipolar and bipolar chargers before the first DMA for particle classification is shown in Fig. 3.2(a). Nitrogen purge of 9.3 slm was injected into the coating chamber. Negative particles at mobility diameter of 13 nm were selected by the first DMA, and the second DMA was set to scan the negative nanoparticles. The results show that the particle counts for the unipolar charger case are twice as high as the bipolar case, indicating that the unipolar charger operating at a voltage of 1 kV is about twice as efficient as the bipolar charger for charging iron oxide nanoparticles of mobility diameter around 13 nm. For the unipolar charger case, a satellite peak at mobility diameter of ~19

nm shows up. This satellite peak is due to the charge state change of 19-nm doubly charged particles, which have the same electric mobility as 13-nm singly charged particles, selected by the first DMA. These doubly charged particles losing one electron charge in the second charger become singly charged. Thus a satellite peak for these singly charged particles of 19 nm appears in the result scanned by the second DMA. The satellite peak is much stronger for the unipolar case than for the bipolar case, indicating a higher fraction of doubly charged particles obtained by the unipolar charger.

Fig. 3.2 (b) shows the effect of the applied voltage of the unipolar charger on particle classification. In this experiment, negative particles were selected at a mobility diameter of 20 nm by the first DMA, the N_2 purge was set at 3.5 slm, and the second DMA was set to scan the negative particles. The first charger was unipolar and the applied voltage increased from 0 to 2 kV. All TDMA particle size distributions were normalized by the peak value at 20 nm. For the zero-voltage case, the unipolar charger behaves like a bipolar charger; the detected satellite peak is negligible. When a voltage was applied, particles passing through the unipolar charger become charged with only one polarity, such as negative. Then, the unipolar charged particles entered the first DMA for size selection. The satellite peak at mobility diameter ~28 nm, seen in Fig. 3.2(b), comes from the doubly charged particles which have the same electric mobility of 20-nm singly charged particles. As the applied voltage increases from 1 kV to 2 kV, the relative intensity of the satellite peak increases; this indicates that the fraction of doubly charged particles increases as the unipolar voltage increases. In all later TDMA coating experiments, the applied voltage was set at 1 kV to reduce the satellite peaks.

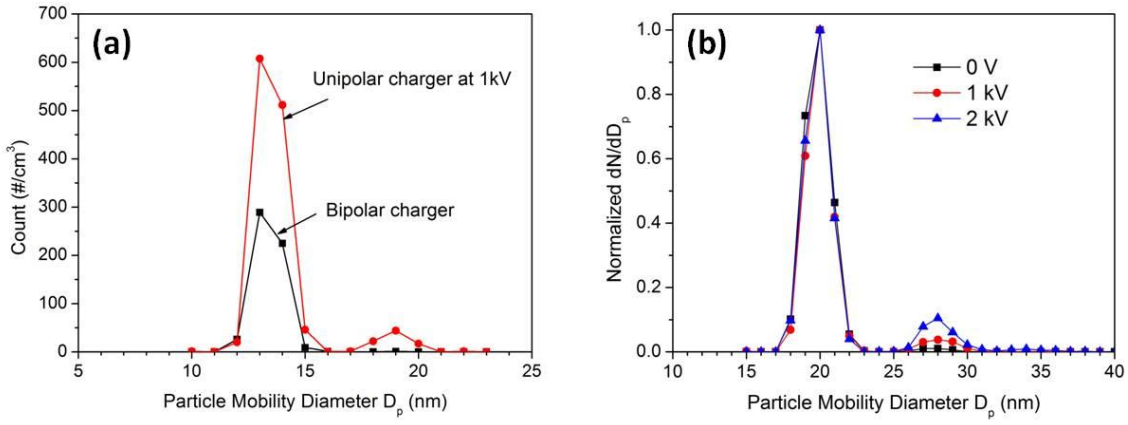

Figure 3.2 TDMA results of the unipolar charger charging effect: (a) comparison of the particle counts for the unipolar and bipolar chargers used before the first DMA; (b) normalized particle size distributions when unipolar charger voltage of 0–2 kV was used.

3.2.3 UV CHARGING EFFECT

The UV photons emitted by the xenon lamp not only dissociate the TEOS precursor, creating reactive species for chemical vapor deposition, but also change the charge state of the particles inside the coating chamber. The UV photon energy (~7.2 eV) is much high than the work function of magnetite (~5.78 eV for bulk Fe_3O_4) [163]. The interaction between the high-energy photons and particles could result in emission of electrons from the particle surfaces [164-168]. The particles become positively charged, and emitted photoelectrons attach to gas molecules to form negative ions. The positively charged particles could become neutral or negative particles by attaching negative ions or photoelectrons. The UV-charging mechanism in this system was studied using the TDMA system by selecting positive and negative iron oxide nanoparticles separately into the coating chamber. The temperature of the CVD chamber was at 300 ℃, and 4.7 slm of N_2 purge was used. The unipolar charger before the first DMA was operated at a voltage

of 1 kV. In order to study the UV-charging effect, no charger was used before the second DMA for the experiments described here.

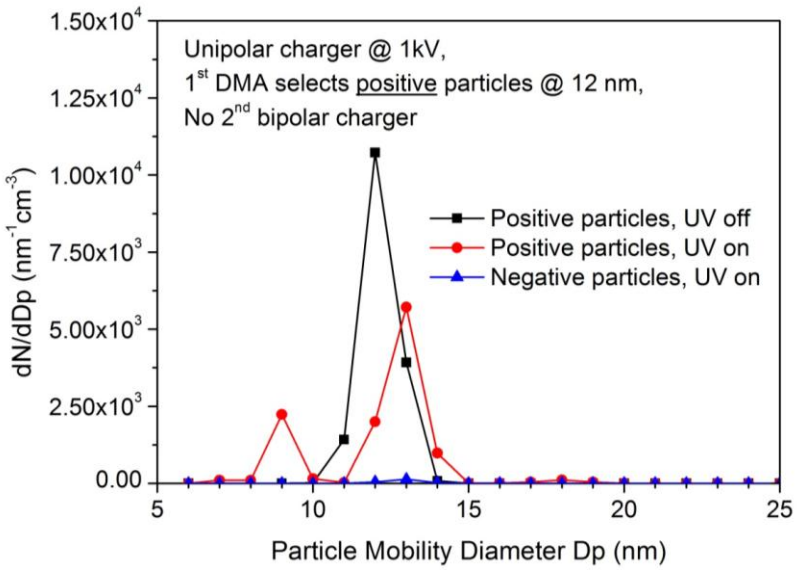

Figure 3.3 TDMA results of the UV effect on the change of particle charge state inside the photo-CVD chamber: 4.7 slm of N_2 purge, positive particles of 12 nm were selected by the 1st DMA, no charger before the 2nd DMA.

Fig. 3.3 shows the particle size distribution measurements for both positive and negative particles scanned by the second DMA. Only positive iron oxide nanoparticles at a mobility diameter of 12 nm were selected by the first DMA to pass into the CVD chamber for this experiment. When the UV lamp was off, only positive particles at 12 nm were detected. When UV lamp was on, the concentration of positive particles decreased, and a satellite peak at around 9 nm appeared. This satellite peak was due to doubly charged particles. A small fraction of negative particles were also detected. These results indicated that positive particles (+1) could either attach negative ions or free electrons

created by photodetachment forming neutral or negative particles (-1), or emit electrons forming doubly charged particles (+2) under the irradiation of the UV light.

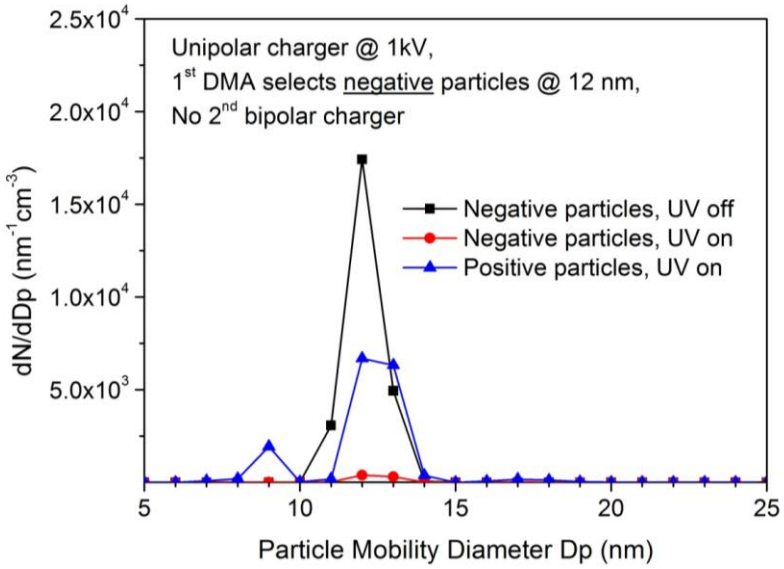

Figure 3.4 TDMA results of the UV effect on the change of particle charge state inside the photo-CVD chamber: 4.7 slm of N_2 purge, negative particles of 12 nm were selected by the 1st DMA, no bipolar charger before the 2nd DMA.

Results for the case, when negative iron oxide nanoparticles at a mobility diameter of 12 nm were selected by the first DMA to pass into the coating chamber are shown in Fig. 3.4. When the UV lamp was off, only negative particles at 12 nm were detected. When the UV lamp was on, both negative and positive particles were detected. However, the results showed that the concentration of positive particles that were detected was much higher than the concentration of the negative particles, indicating that most negative particles (-1) lose electrons under the UV irradiation to form neutral or positively charged (+1 or +2) particles.

The summary of the TDMA measurements of the UV effect for Fig. 3.3 and 3.4 is listed in Table 3-1. This table shows that for both selections of the particle polarity for the first DMA, about 60–70% of particles are charged positively, another ~30% of particles became neutral and only a very small fraction of particles are negatively charged after passing through the CVD chamber with the UV lamp turned on. These TDMA results indicate that the UV photo-detachment process is the dominant charging mechanism inside the CVD chamber, and the particles are more likely to become positively charged under the UV irradiation with the configuration of the coating experiments described here.

Zhang has also studied the effect of photoemission on NaCl nanoparticles at a mobility diameter of 41 nm [76]. He found that when positively charged particles exposed to UV, only 42.1% of particles remained positively charged, the rest became neutral (41.1%) or negative (13.8%) particles; while for the negative case, 28.3% remained negatively charged, 53.2% became neutral, and 18.5% turned to positive particles. A higher fraction of particles keeping the initial charge state for positive particles than for negative particles when exposed to UV also indicates the dominance of UV photo-detachment phenomenon inside the UV chamber.

Polarity of 1st DMA selected particles	**UV on**		
	Negative particles	Positive particles	Neutral particles
Positive particles @12 nm	1.2%	71.3%	27.5%
Negative particles @12 nm	3.0%	63.4%	33.6%

Table 3-1 TDMA results of UV charging effect.

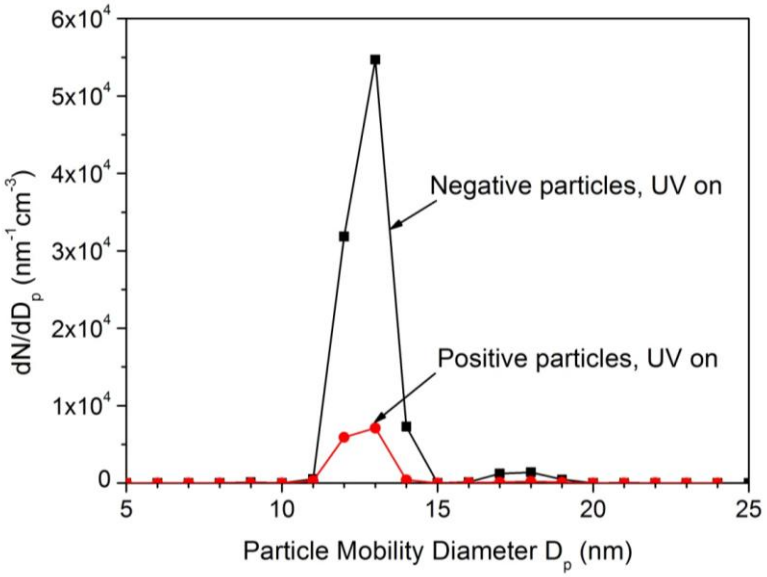

Figure 3.5 TDMA results of positive and negative particles scanned by the second DMA: 4.7 slm of N_2 purge, negative iron oxide particles of 12 nm were selected by the 1st DMA.

A second charger before the second DMA is important for TDMA coating measurements because of the charging effect of the UV photons inside the coating chamber. Fig. 3.5 compares the particle size distribution results of the negative and positive iron oxide nanoparticles scanned by the second DMA. In this experiment, N_2 purge flow of 4.7 slm was used. The unipolar charger was operated at 1 kV and the first DMA was set to select negative particles at a mobility diameter of 12 nm. No TEOS precursor was injected. When the UV lamp turned on, one may expect more positive particles produced by the UV light which is more likely to charge particles positively, as discussed above. When a second particle charger (i.e., neutralizer) is used before the second DMA, the detected particles size distributions for both negative and positive particles in Fig. 3.5 are very different from results in Fig. 3.4. Fig. 3.5 shows that more negative particles are detected than the positive particles, possibly because the neutralizer

recharges the particles and it is more effective to charge particles negatively [169]. In order to get high particle counts for representative TDMA measurements, the TDMA was set for all subsequent measurements to scan and measure negative particles.

3.3 Experimental Results and Discussion

The silica coating process was monitored online by a TDMA system. The CVD system was tested for TEOS self-nucleation without the iron oxide core particle before the coating experiments. The coating chamber was kept at 300 ℃, and 7 slm of clean N_2 gas was injected as the purge gas next to the UV window. The TEOS vapor was injected by the N_2 carrier gas bubbling through the liquid precursor bubbler. The coating chamber was maintained at atmospheric pressure. Fig. 3.6 shows the raw particle counts of the SMPS results. When the UV lamp was turned on, almost no particles were detected up to 1.83 sccm of TEOS. The SMPS results indicated that no homogeneous nucleation of the silica was formed under the condition of TEOS flow rate up to 1.83 sccm.

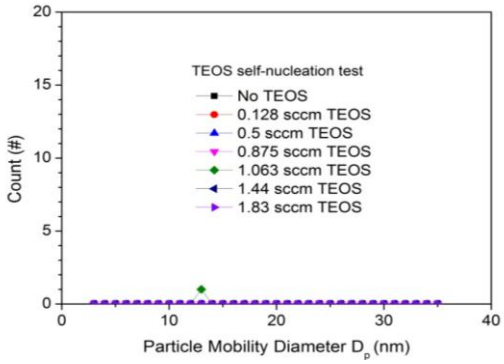

Figure 3.6 TEOS self-nucleation test: CVD chamber at 300 ℃, 7 slm of N_2 purge, no iron oxide aerosol, UV lamp on, varying TEOS flow rate.

The TEOS self-nucleation test confirmed that the TEOS flow rate (up to 1.83 sccm) was not high enough to form homogeneous nucleated silica particles with N_2 purge flow of 7 slm. When iron oxide nanoparticles were injected into the coating chamber, the dissociated TEOS radicals will condense on to the iron oxide nanoparticle surfaces, causing the diameter growth of the particles. The TDMA results showed the particle size distribution of silica-coated iron oxide nanoparticles with varying precursor and N_2 purge flow rates, as seen in Fig. 3.7. Negative iron oxide nanoparticles at a mobility diameter of 14 nm were selected by the first DMA. The unipolar charger was operated at a voltage of 1 kV. A neutralizer was used before the second DMA and negative particles were scanned by the second DMA.

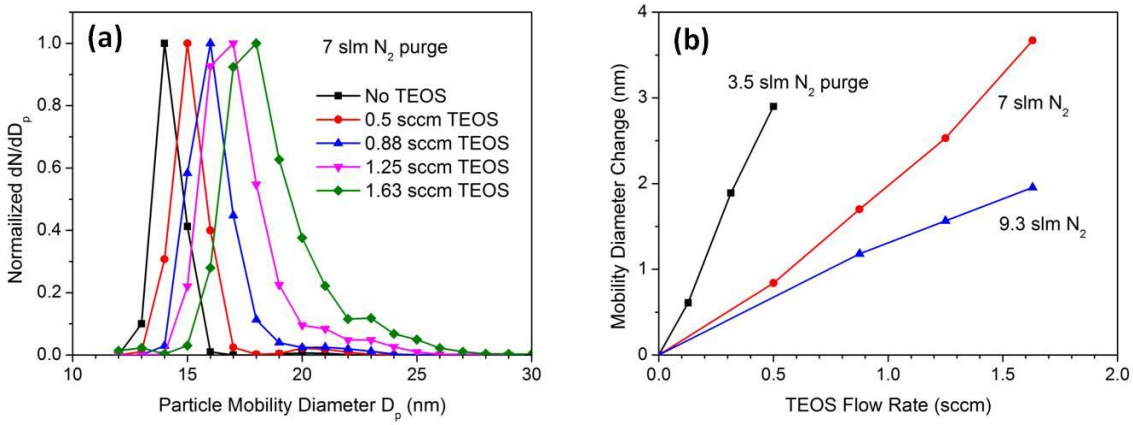

Figure 3.7 TDMA results of the silica coating: CVD chamber at 300 ℃, unipolar charger with an applied voltage of 1 kV; negative iron oxide particles were selected at a mobility diameter of 14 nm by the 1st DMA; with a neutralizer before the 2nd DMA, and negative particles were scanned by the 2nd DMA (a) varying TEOS flow rate, 7 slm of N_2 purge; (b) particle mobility diameter change with TEOS flow rate at 3.5, 7, and 9.3 slm N_2 purge.

As shown in Fig. 3.7(a), when no TEOS is injected, the size distribution shows as a monodisperse peak at 14 nm, and the particle size increases as the injected TEOS flow

rate increases. The particle mobility diameter change is determined by the shift in the particle mean diameter which is obtained by fitting the size distribution with Gaussian fit in Origin (Origin Lab). Fig. 3.7(b) summarizes the particle mobility diameter change with the TEOS flow rate at N_2 purge flow of 3.5, 7, and 9.3 slm. Half of the diameter change corresponds to the thickness of the silica coating. For all cases of the N_2 purge flow rate, the thickness of the silica coating increases with the TEOS flow rate. For the same TEOS flow rate, silica coating thickness increases as the purge flow decreases. This could be because reducing the N_2 purge flow leads to an increase in the residence time for silica growth inside the CVD chamber; thus, the silica coating thickness increases. The TDMA results indicate that the thickness of the silica coating can be tuned by controlling the TEOS flow rate and total residence time inside the coating chamber.

The TDMA system presents good opportunities for investigation of the relations between the thickness of the silica coating and experimental parameters, such as TEOS flow rate and N_2 purge flow. However, the particle concentration could decrease several orders of magnitude after size selection because of the use of two DMAs and two particle chargers. The DMA transfer function—the probability of the particles of a mobility diameter passing through the DMA—which is calculated using the equations developed by Knutson and Whitby [38], equals ~0.356 for particles of 14 nm. The charging efficiency of the neutralizer (bipolar charger) equals ~0.075 for particles of 14 nm [37]. Assuming the unipolar charger has a charging efficiency twice the bipolar charger efficiency, as shown in Fig. 3.2, the concentration of the size-selected particles decreases by ~3 orders of magnitude after the TDMA system. The low concentration of the

SPIO@SiO_2 synthesized when using the TDMA system causes hours of collection time to collect enough mass of particles for offline characterization. In addition, some self-nucleated silica particles were also detected by the TDMA. The homogeneous nucleation of the silica could be suppressed by increasing the N_2 purge and concentration of iron oxide core particles.

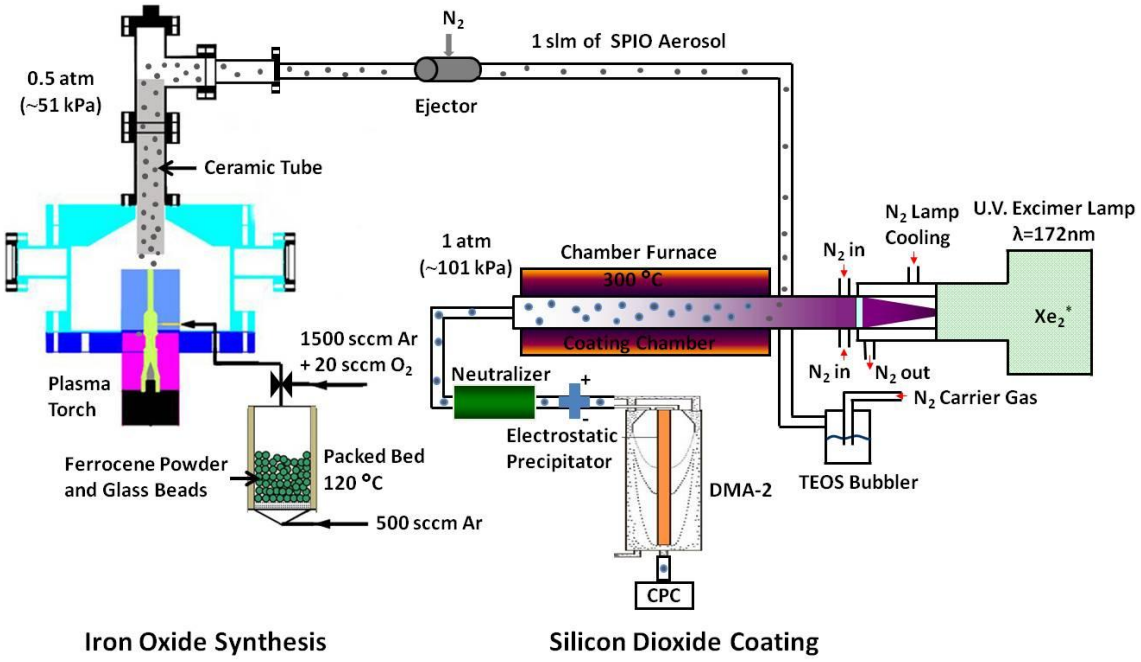

Figure 3.8 Polydisperse iron oxide coating at atmospheric pressure.

In order to increase the production rate of the silica-coated iron oxide nanoparticles and reduce the homogeneous nucleation of silica, polydisperse iron oxide nanoparticles that had been sampled from the plasma chamber using an N_2-driven ejector were sent directly into the coating chamber without size selection. The modified experimental setup is shown in Fig. 3.8. Polydisperse SPIO aerosol of 1 slm was

introduced into the CVD chamber together with the TEOS precursor. The coated particles were sampled to a SMPS system for online particle size distribution measurements.

The CVD system was tested for silica homogeneous nucleation again by the SMPS system. The CVD chamber was kept at 300 ℃ and N_2 purge of 3.5 slm was used as the main gas flow. Without injection of iron oxide nanoparticles, few particles were detected by SMPS, indicating that no self-nucleation of silica nanoparticles happened with TEOS flow rate up to 1.25 sccm, as shown in Fig. 3.9.

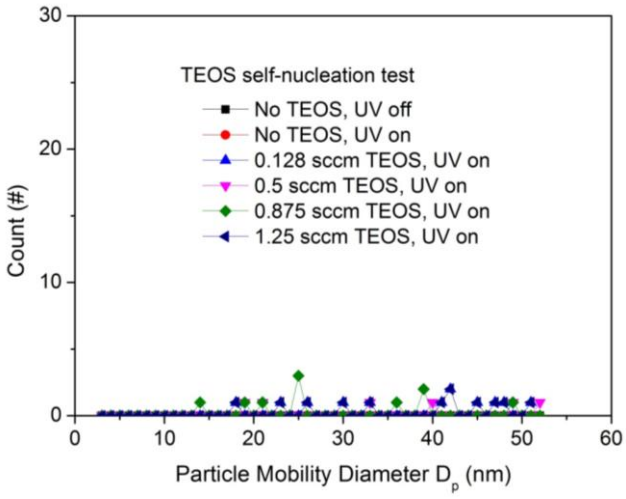

Figure 3.9 TEOS self-nucleation test at atmospheric pressure: CVD chamber at 300 ℃, no iron oxide aerosol, 3.5 slm of N_2 purge, UV lamp on, and varying TEOS flow rate.

The SMPS results of the size distribution of silica-coated iron oxide nanoparticles are shown in Fig. 3.10. When no TEOS precursor was injected, the size distribution of the bare (un-coated) iron oxide nanoparticles had a mode of ~11 nm. The size distribution of the coated particles gradually shifted to larger sizes as the TEOS precursor flow rate increased, indicating that the thickness of the silica coating increased with the TEOS flow rate. Small peaks at the lower sizes were detected when the TEOS flow rate increased to

0.688 and 0.875 sccm, which may indicate that homogeneous nucleation of silica particles occurred. The homogeneous nucleation process of silica particles strongly depends on the partial pressure of the TEOS vapor and O_2 inside the coating chamber. Without the injection of iron oxide aerosols, no homogeneous nucleation was observed with TEOS flow rate up to 1.25 sccm. When iron oxide aerosol was injected, homogeneous nucleation occurred at a lower TEOS flow rate. This may be caused by the residue O_2, H_2O, and CO_2 species produced from the plasma system.

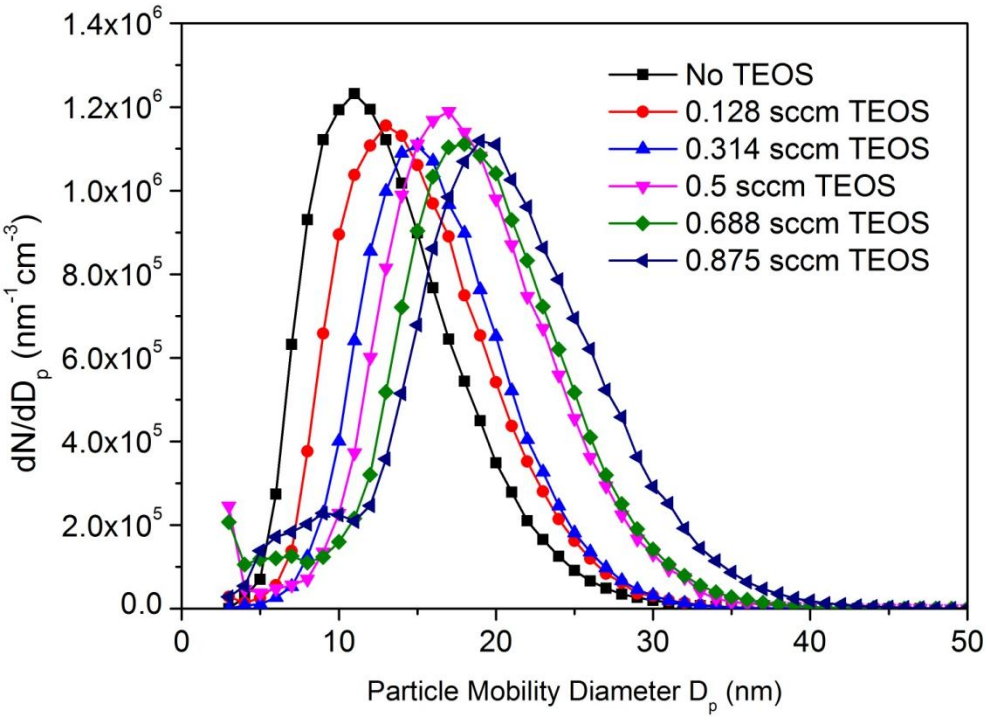

Figure 3.10 SMPS results of silica coating at atmospheric pressure: 1 slm of polydisperse plasma-synthesized SPIO aerosol, 3.5 slm of N_2 purge, UV lamp on, and varying TEOS flow rate.

The morphology of the core-shell structured silica-coated iron oxide nanoparticles was characterized by HRTEM, as shown in Fig. 3.11. The particles were collected on lacey carbon grids. The iron oxide core has a crystal structure, showing the crystal fringes

in the center, and the silica shell is amorphous. In Fig. 3.11(a), the particle was produced with TEOS flow rate of 0.314 sccm, the silica thickness is about 1–2 nm. The d-spacing, the distance between two fringes, is ~3.0 Å measured by Image J, which corresponds to the Fe_3O_4 (022) plane. As the TEOS flow rate increases to 0.5 sccm, the silica coating thickness increases to about 3–4 nm, as shown in Fig. 3.11(b). The HRTEM results confirm that the core-shell structured SPIO@SiO_2 NPs were achieved by photo-CVD and the thickness of the silica coating increased with the TEOS flow rate.

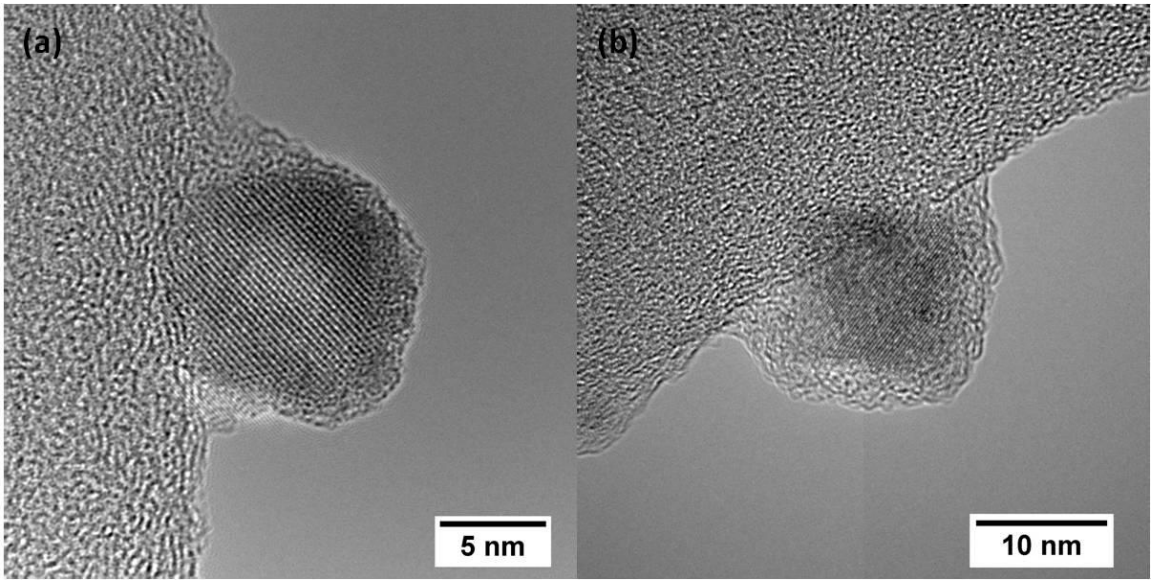

Figure 3.11 HRTEM images of SPIO@SiO_2 NPs produced at CVD chamber 300 ℃, 3.5 slm of N_2 purge and 1 slm of diluted SPIO aerosol: (a) 0.314 sccm TEOS; (b) 0.5 sccm TEOS.

The elemental composition of the core-shell structured particles was analyzed by EDS in the STEM mode. The iron oxide core has higher mass contrast compared to the amorphous silica shell, resulting in brighter color in the dark-field image shown in Fig. 3.12 (a). The EDS position scan was conducted at the center of the bright core labeled as the red circle in the image. The EDS spectrum is shown in Fig. 3.12(b). The C and Cu

signals are background signals from the TEM grid. Besides the background signals, Fe, Si and O were also detected. The EDS result is consistent with the expectation that the core-shell structured particle consists of iron oxide and silica.

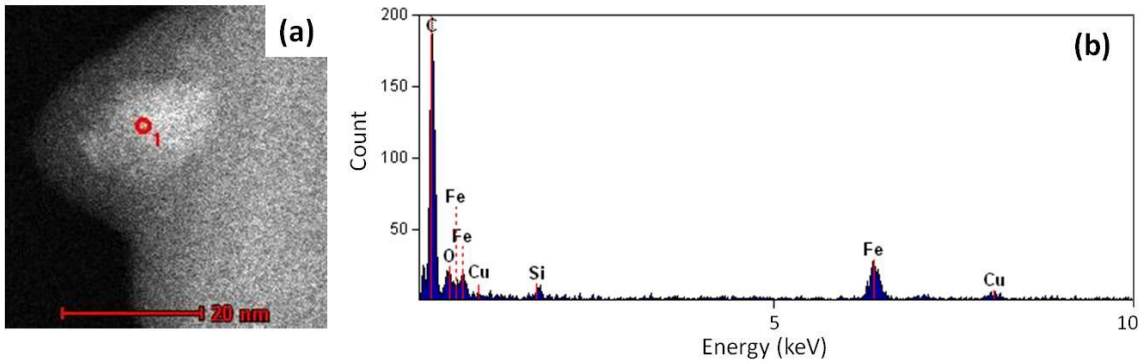

Figure 3.12 STEM analysis of SPIO@SiO_2 produced at CVD chamber 300 ℃, 3.5 slm of N_2 purge, 1 slm of diluted SPION aerosol injected into coating chamber, and 0.5 sccm of TEOS: (a) dark-field of STEM image of SPIO@SiO_2; (b) EDS position scan on the labeled circle.

To further increase the yield of silica-coated iron oxide nanoparticles, the process of low-pressure coating was investigated in order to produce enough mass of particles collected on stainless steel filters for FTIR analysis and magnetic property measurements. In this approach, the iron oxide aerosol was sampled directly into the CVD chamber without dilution. The coating chamber was kept at low pressure (~40–50 kPa), and a sampler collector located in the exhaust line was used to collect the final product. The modified experimental setup for low-pressure coating is shown in Fig. 3.13. Plasma-synthesized SPIO aerosol of ~9 slm controlled by a rotameter was introduced into the coating chamber for silica coating. N_2 purge of 3.5 slm was injected next to the UV window to keep the window clean. The final product was collected on stainless steel filters (400 × 400 mesh) for FTIR analysis.

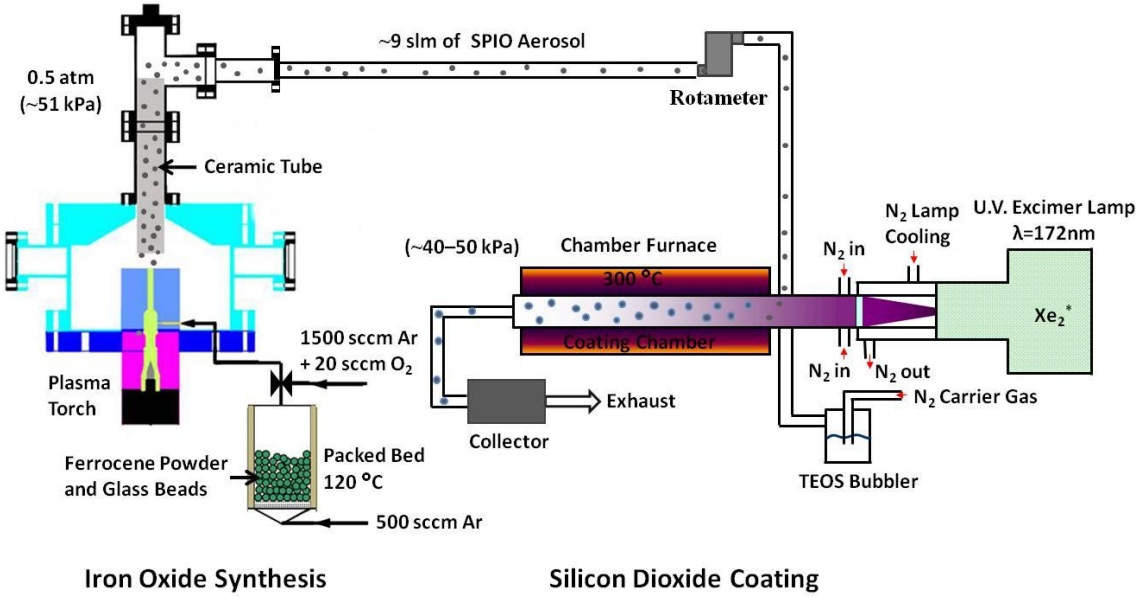

Figure 3.13 Experimental setup for low-pressure polydisperse coating.

The surface chemistry of the silica-coated iron oxide nanoparticles was characterized by FTIR, with particles collected on stainless steel mesh filters for about one hour for each case of the TEOS flow rate. The FTIR absorbance spectra of silica-coated and un-coated iron oxide nanoparticles are compared in Fig. 3.14. The spectrum of the bare iron oxide nanoparticles has no significant absorption peaks in the infrared region. For silica-coated iron oxide nanoparticles, Si–O–Si symmetric stretching modes at ~800 cm^{-1}, asymmetric stretching modes at ~1100 cm^{-1}, and the Si–OH stretching at ~970 cm^{-1} appear in the spectra. Silanol groups are also present on the surface of the coating, as evidenced by the broad peak centered ~3450 cm^{-1}, associated with the silanol O–H stretch. The C–H stretching modes at ~2800–3000 cm^{-1} and ~1300–1500 cm^{-1} come from C and H impurities on the silica surface. At TEOS flow rate of 0.23 sccm, the spectrum also shows a Si–O sub-oxide at ~1083 cm^{-1}. As the TEOS flow rate increases,

the intensity of the sub-oxide peak decreases, which indicates that the silica is closer to the stoichiometric ratio as the thickness of the silica coating increases.

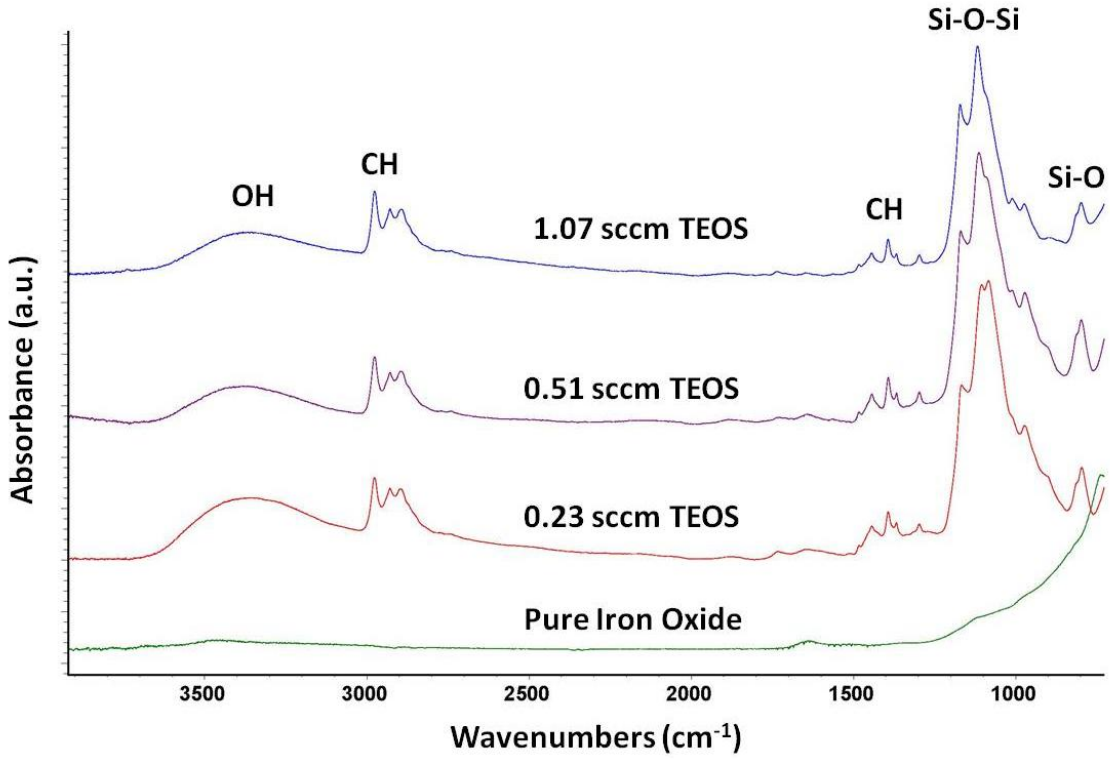

Figure 3.14 FTIR spectra of silica-coated iron oxide nanoparticles: CVD chamber at 300 ℃, 3.5 slm of N_2 purge, 9 slm of SPIO aerosol flow, and varying TEOS flow rate.

In order to investigate the magnetic properties of silica-coated iron oxide nanoparticles, the coated particles were collected on glass fiber filters after the coating chamber, and their magnetic properties were measured with VSM. In this experiment, the plasma-synthesized SPIO aerosol of 17 slm was introduced into the CVD chamber together with 3.7-sccm TEOS vapor and 3.5-slm N_2 purge. The temperature and pressure of the chamber were maintained at 300 ℃, and ~40–50 kPa, respectively.

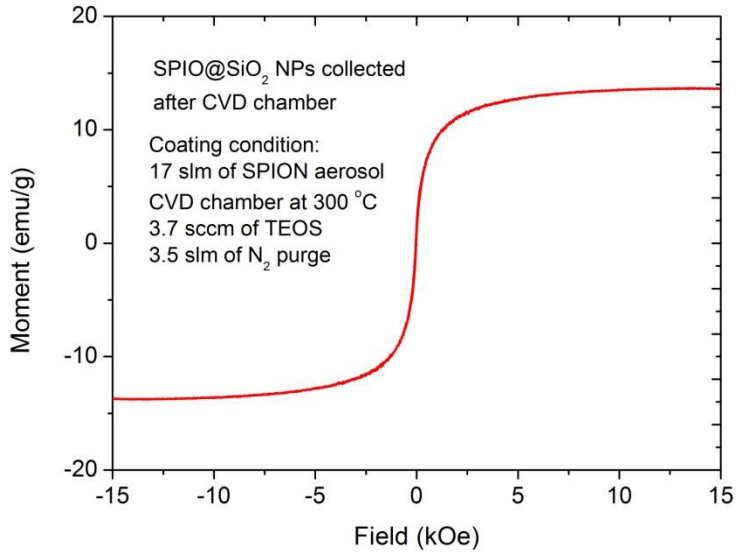

Figure 3.15 Hysteresis loop measured at room temperature for silica-coated iron oxide nanoparticles collected on the glass fiber filter.

Fig 3.15 shows the hysteresis loop of silica-coated iron oxide nanoparticles measured at room temperature. Both remanence and coercivity are close to zero indicating that the coated particles maintain the superparamagnetic property. The saturation magnetization was measured at ~13.66 emu/g, which was normalized by the total particle mass collected on the filter. For bare iron oxide nanoparticles, the best saturation magnetization was achieved at ~40.15 emu/g, as previously discussed in Chapter 2. The saturation magnetization of the coated particles is reduced, which could be due to the additional mass of the diamagnetic material (i.e., silica), which reduces the magnetization of the coated particles when normalized by total mass of the coated particles. These are preliminary results for magnetic measurements of the silica-coated nanoparticles. In order to study the effect of the silica coating on the magnetic properties, the measured magnetic moment could be normalized on a per mass base of iron [170] or

iron oxide [89]. The iron concentration in the silica-coated particles could be determined using a colorimetric method [170-173]. Ongoing study will investigate the effect of the silica coating thickness on the magnetic properties, and the stability of the silica-coated iron oxide nanoparticles dispersed in liquid solutions.

3.4 SUMMARY

Silica coating on iron oxide nanoparticles can be synthesized by a photo-induced chemical vapor deposition method. Both atmospheric and low pressure coating conditions were investigated and shown to produce silica coatings, as confirmed by EDS and FTIR analysis. TDMA and SMPS results combined with HRTEM images indicate that all particles are effectively coated with a continuous silica shell, and the silica coating thickness can be tuned to desired values, depending on the application, by varying the TEOS precursor flow rate and total residence time inside the coating chamber. Silica coatings are shown to decrease the saturation magnetization when determined on a total mass basis of the coated particles. More work could be done in the future to study the effect of the silica coating thickness on the magnetization of the iron oxide core particles, and the stability in liquid suspension.

Chapter 4 PEGylation of Gold-Decorated Silica Nanoparticles in Aerosol Phase

4.1 BACKGROUND

Gold nanostuctures are currently the subject of intense interest because of the surface plasmon resonance effect. The gold nanoparticles absorb radiation at specific wavelengths in the visible region [33], while gold nanoshells have absorption in the near-infrared wavelength region [34]. The surface plasmon resonance of gold nanoparticles and nanoshells enables laser-based imaging and heating for biomedical applications [29, 32, 131, 174-177]. Additionally, gold nanoparticles with diameters below about 5 nm have been shown to be effective catalysts. Combined with their absorption in the visible wavelength region, this makes gold nanoparticles a promising material for solar-driven photocatalysis [178-182].

The production of gold nanoparticles has mostly been accomplished using wet chemistry through the reduction of gold precursors [183-185]. Gas-phase synthesis of gold nanoparticles has been achieved by chemical vapor deposition using organometallic gold precursors [186-188]. Recently, Boies et al. demonstrated a unique gas-phase technique producing single crystal gold nanoparticles (< 10 nm), using a gold-coated platinum hot-wire evaporated at atmospheric pressure [189]. In this study, the gold hot-wire generator was used to generate gold nanoparticles as the source for decorating silica or silica-coated magnetic iron oxide nanoparticles.

Silica (SiO_2) has been widely used as substrates for gold nanoparticles or nanoshells, as its biocompatibility, dielectric properties, and high chemical and thermal stability make it an excellent choice for many applications [130-132, 190-192]. Synthesis of SiO_2@Au nanostructures is usually accomplished by means of wet chemistry [131, 132, 192-197]. Boies et al. reported an aerosol method for producing gold-decorated silica nanoparticles [198]. The core silica nanoparticles had a diameter in the range of 10–50 nm, with islands of gold nanoparticles of 1–3 nm in diameter on the surfaces.

The use of aerosol methods for multilayer nanoparticle synthesis has the potential advantage of being less prone to contamination from impurity residues than are liquid-phase methods. Also, aerosol methods do not require the use of surfactants (which typically must then be removed before addition of the next layer), and involve continuous flows with residence times lasting seconds, rather than multi-step batch processes with residence times lasting many hours or even days. These methods are also scalable to high production rates. However, for biomedical and many other potential applications, the desired final product remains nanoparticles in stable liquid (often aqueous) dispersion. Therefore, an important challenge for nanoparticle aerosol technology is to develop methods for transferring nanoparticles from the aerosol to the hydrosol phase.

One method for transferring nanoparticles from the aerosol phase to an aqueous dispersion is to coat them with a hydrophilic substance, such as polyethylene glycol (PEG). PEG is widely used to coat nanoparticles for biomedical applications because it is biocompatible and hydrophilic, which improves solubility, suppresses nanoparticle aggregation, reduces uptake by the reticuloendothelial system, and increasing blood

circulation time for drug delivery [175, 199]. If a robust method for PEGylating nanoparticles in the aerosol phase were available, the particles could readily be transferred into a stable aqueous dispersion before experiencing the aggregation that often accompanies particle collection as a dry powder. Thus, the advantages of aerosol processing could be realized, while still producing a liquid dispersion as end product.

Several studies have reported PEGylation of silica-gold nanostructures by means of wet chemistry [131, 132, 197, 200, 201]. To my knowledge, the only previous report of aerosol-phase PEGylation of nanoparticles of any substance appeared in the Ph.D. thesis of Calder [202], who developed a two-step chemical vapor deposition approach. In the first step, the nanoparticle is functionalized with a bifunctional reactant that attaches at one end to the nanoparticle surface while the other end has a terminal hydroxyl group. In the second step, ethylene oxide (EO) is introduced into the aerosol stream, which is then sent through a tube furnace. The EO reacts with the terminal hydroxyl group via a ring-opening insertion polymerization to grow PEG. Calder demonstrated this approach by PEGylating silicon nanoparticles, functionalized with ethylene glycol, and gold nanoparticles, functionalized with 2-mercaptoethanol (ME).

4.2 Gold Decoration on Silica Nanoparticles

Gold-decorated silica (SiO_2@Au) nanoparticles were synthesized using the method described by Boies et al. [198]. The decorated nanoparticles were used as the core particles for further gas-phase PEGylation. The gold decoration process also provided an important guideline to study the attachment of gold nanoparticles on silica-

coated magnetic iron oxide nanoparticles for synthesizing tri-layer gold-decorated silica-coated superparamagnetic iron oxide nanoparticles, which will be discussed in Chapter 5.

4.2.1 EXPERIMENTAL PROCEDURE

An experimental schematic for gas-phase synthesis of gold-decorated silica nanoparticles is shown in Figure 4.1. Silica nanoparticles are synthesized by thermal decomposition of tetraethylorthosilicate (TEOS) in a nitrogen atmosphere. In the experiments described here, TEOS vapor, at a flow rate of ~0.018 sccm, is generated by a bubbler, and is carried by 10 sccm of nitrogen into a decomposition furnace, where it mixes with 2.5 slm of nitrogen at a temperature of 900 ℃. This temperature is sufficiently high to decompose the TEOS presursor, leading to generation of SiO_2 nanoparticles by gas-phase nucleation. An additional 2 slm of nitrogen is added, providing some dilution so as to reduce agglomeration, before the flow enters a second-stage furnace, referred to as the "sintering furnace," which operates at 1200 °C, high enough to spheroidize any agglomerates.

Following the sintering furnace, the silica aerosol passes through a gold-coated platinum hot-wire generator where gold nanoparticles are generated. The platinum wire (Alfa Aesar, 0.404 mm in diameter) was coated by INCERTEC with soft gold with a thickness of 3 μm. The gold-coated platinum hot-wire was placed inside a 3-mm nozzle. As platinum has a higher melting temperature (~1768 ℃) than gold (~1064 ℃), the wire temperature can somewhat exceed the melting temperature of gold while still maintaining electrical resistive heating. The gold vapor generated from the wire, diffusing to colder

regions, undergoes homogeneous nucleation, producing gold nanoparticles. The size distribution of the gold nanoparticles can be controlled by varying the wire power and the flow rate of the nitrogen gas that passes over the wire [189]. The gold hot-wire generator chamber is followed by a gold decoration chamber, which controls the residence time for scavenging of the gold nanoparticles by the larger silica nanoparticles. Then, gold-decorated silica nanoparticles were sent to a sampling system for collection and characterization.

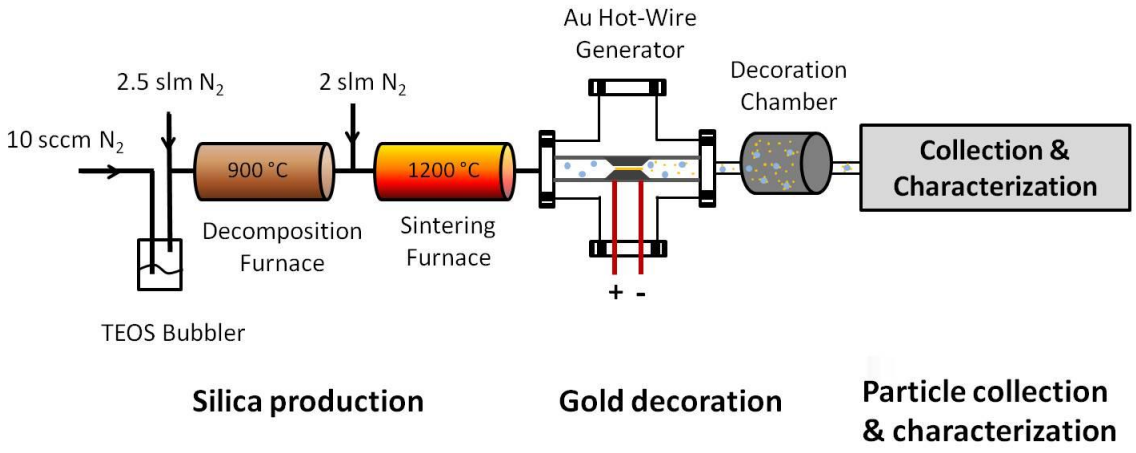

Figure 4.1 Schematic of experimental system for synthesis of gold-decorated silica nanoparticles.

The size distribution of pure gold nanoparticles was measured online by sending a pure nitrogen gas directly into the gold hot-wire chamber and sampling aerosol into a scanning mobility particle sizer system, as describe in Chapter 1, before the decoration chamber. Gold-decorated silica nanoparticles were collected onto lacey carbon TEM grids (Ted Pella 01890) using an electrostatic precipitator with an applied voltage of 3 kV after the neutralizer. These samples were characterized by high-resolution transmission electron microscopy (HRTEM), conducted on a Tecnai G^2 F30 electron microscope.

4.2.2 Experimental Results and Discussion

Each new section of gold-platinum hot wire, total length of ~5 cm, was wrapped with additional gold wire (Sigma-Aldrich, 0.25 mm in diameter) at two ends, leaving center length ~2 cm exposed in the gas stream for evaporation. An initial heating period of 2–3 hours for each new wire was needed to generate stable distribution of gold nanoparticles. The size distributions of gold nanoparticles generated by the gold hot-wire, shown in Figure 4.2, were measured by a SMPS system. The gold nanoparticle size distribution was controlled by two parameters: hot-wire voltage and N_2 flow rate passing over the hot wire. Fig. 4.2(a) shows that the gold nanoparticle size increases as hot-wire voltage increases for the same N_2 flow rate of 4.5slm. As voltage increases, the total hot-wire power increases resulting in a higher hot-wire temperature, which leads to a higher production of gold vapor and thus larger gold nanoparticle sizes. In Fig. 4.2(b), the hot-wire voltage is kept at 1.65 V, and gold nanoparticle size decreases as the N_2 flow rate increases from 2.5 to 4.5 slm. The decrease of gold nanoparticle size may be due to two causes. First, a higher N_2 flow rate corresponds to a higher cooling rate at the hot-wire surface, resulting in a lower hot-wire temperature: generating less gold vapor and forming smaller gold nanoparticles. Second, higher N_2 flow provides further dilution and suppression of the gold nanoparticle coagulation process, preventing larger gold nanoparticle formation. These results indicate that controlling the two experimental parameters can readily generate gold nanoparticles with particle sizes less than 5 nm.

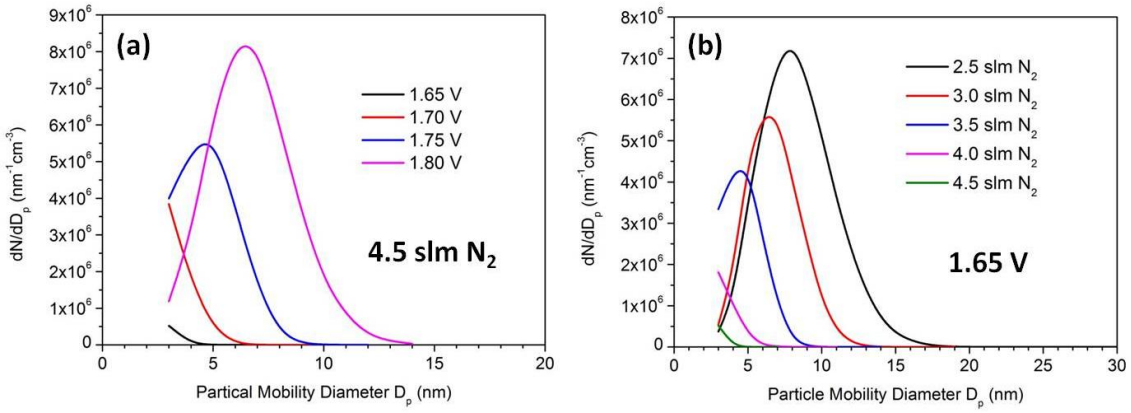

Figure 4.2 Gold nanoparticle size distributions measured by SMPS: (a) varying hot-wire applied voltage with N_2 flow rate of 4.5 slm; (b) varying N_2 flow rate passing through the hot-wire chamber with hot-wire applied voltage at 1.65 V.

The hot-wire power, used to produce gold-decorated silica nanoparticles, was fixed at 19.2 W and different flow rates of silica aerosol were sampled from the exit of the sintering furnace and then passed through both the hot-wire generator and decoration chambers. The decoration chamber was used to increase the residence time for particle–particle collisions. The collision frequency between two populations of particles is proportional to the particle concentrations and the collision kernel between these two populations, which is governed by Equation 4.1:

$$R_{ij} = \beta_{ij} n_i n_j \tag{4.1}$$

where R_{ij} is the collision frequency and β_{ij} is the collision kernel between particle entities i and j; n_i and n_j is the particle concentration for particle entities i and j, respectively. The collision kernel can be determined using the equations described by Gopalakrishnan et al. [203] for the transition regime:

$$H = \frac{12.566Kn_D^2 + 25.836Kn_D^3 + 56.204Kn_D^4}{1 + 3.502Kn_D + 7.211Kn_D^2 + 11.211Kn_D^3} \quad (4.2)$$

where H is the dimensionless collision kernel and Kn_D is the diffusive Knudsen number, which can be described as:

$$H = \frac{\beta_{ij} m_{ij}}{f_{ij}(a_i + a_j)^3} \quad (4.3)$$

$$Kn_D = \frac{\sqrt{k_B T m_{ij}}}{f_{ij}(a_i + a_j)} \quad (4.4)$$

where $m_{ij} = m_i\, m_j/(m_i + m_j)$ is the reduced mass and $f_{ij} = f_i\, f_j/(f_i + f_j)$ is the reduced friction factor; m_i, m_j, f_i, f_j are the masses and friction factors of particle entities i and j, respectively; k_B is Boltzmann's constant, T is the temperature, and a_i and a_j are the particle radius for particle entities i and j, respectively.

At standard condition (T = 293.15 K, pressure = 1 atm), the collision kernel between gold–gold, silica–silica, and gold–silica nanoparticles in the nitrogen gas can be calculated by Equations 4.2–4.4, assuming the gold particle radius is 1 nm and the silica particle radius is 10 nm:

$$\beta_{1\text{nm(Au)}-1\text{nm(Au)}} = 2.0 \times 10^{-16}\ \text{m}^3\text{s}^{-1},$$

$$\beta_{1\text{nm(Au)}-10\text{nm(SiO}_2\text{)}} = 4.2 \times 10^{-15}\ \text{m}^3\text{s}^{-1},$$

$$\beta_{10\text{nm(SiO}_2\text{)}-10\text{nm(SiO}_2\text{)}} = 1.5 \times 10^{-15}\ \text{m}^3\text{s}^{-1}$$

We can see that the collision kernel between gold–silica is about 21 times higher than that between gold–gold nanoparticles, which means that the small gold particles are more

likely to be scavenged by large silica nanoparticles, to become gold-decorated nanoparticles. As the silica nanoparticle concentration is not high (< 10^7 cm^{-3}), the agglomeration process between silica–silica nanoparticles inside the decoration chamber is small, and can be ignored here.

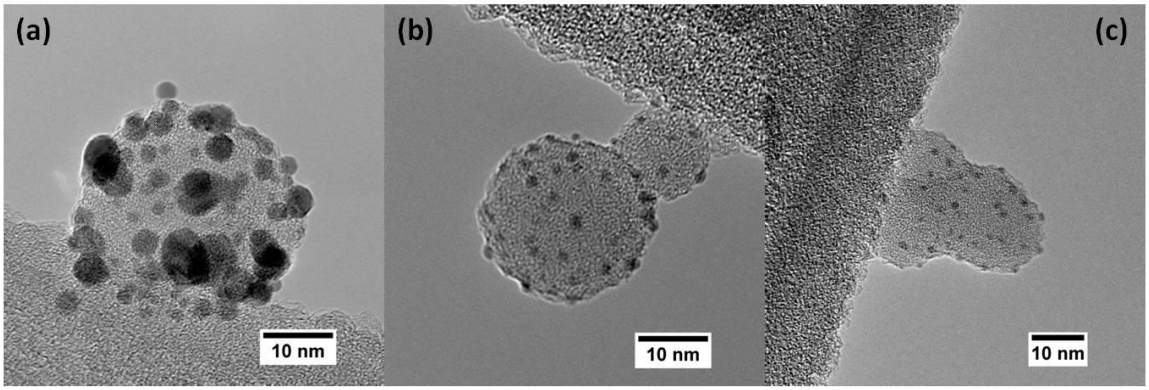

Figure 4.3 HRTEM images of gold-decorated silica nanoparticles produced at: (a) 1.7 slm; (b) 3.2 slm; and (c) 4.5 slm total silica aerosol flow passing through the Au hot-wire generator.

Figure 4.3 shows high resolution TEM (HRTEM) images of gold-decorated silica nanoparticles obtained with flow rates of 1.7 slm, 3.2 slm, and 4.5 slm, for which the corresponding residence times in the decoration chamber equalled 92, 49, and 35 seconds, respectively. The images clearly show the gold decoration, with gold nanoparticles appearing darker than silica due to their higher mass contrast. As the aerosol flow rate increases, the residence time correspondingly decreases, and the size of the gold nanoparticles is seen to decrease. In the 1.7 slm case, shown in Fig. 4.3(a), the residence time in the decoration chamber is relatively long, and the size distribution of the gold nanoparticles is broad, including some relatively large gold nanoparticles of 5–8 nm in diameter. In this case there is evidently some pile-up of gold nanoparticles on the

silica surface. For the two cases of higher flow rate, the gold nanoparticles are isolated on the silica surface and appear more monodisperse. Their mean diameter, as determined by image analysis (ImageJ software), equals approximately 3 nm in the 3.2-slm case, Fig. 4.3(b), and 1.5 nm in the 4.5-slm case, Fig. 4.3(c).

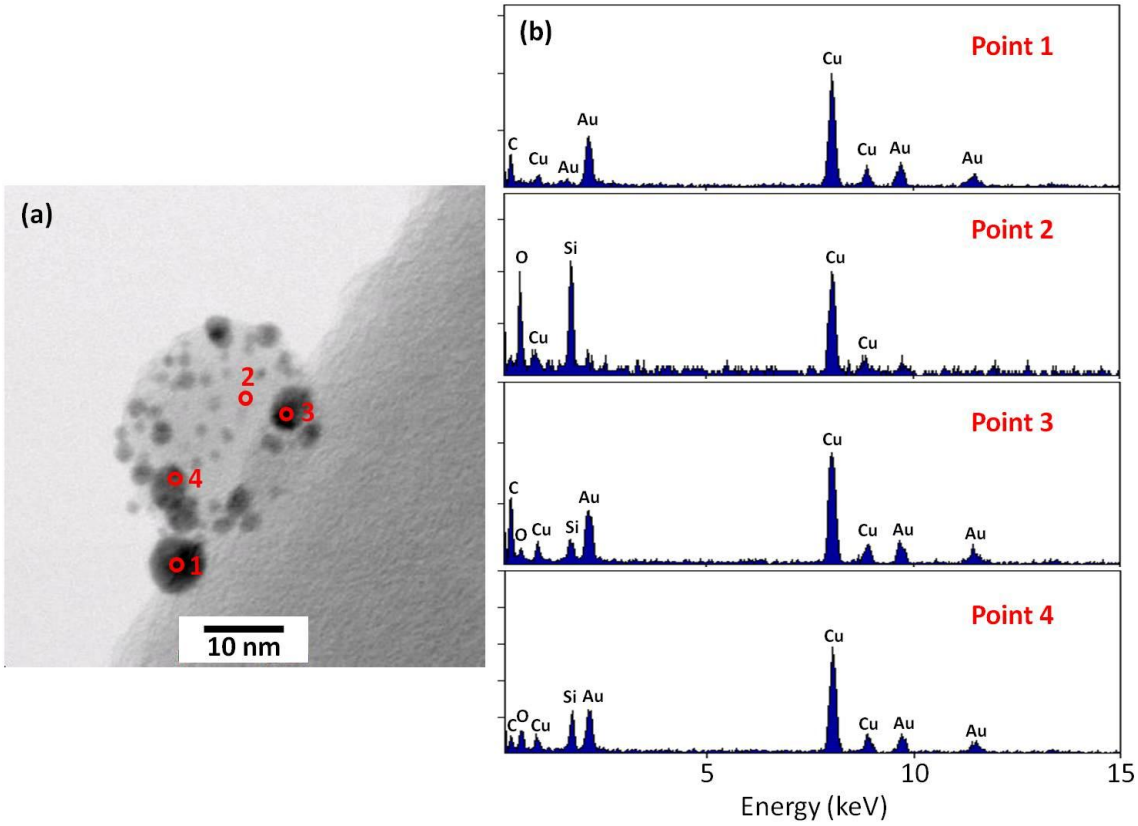

Figure 4.4 Gold-decorated silica nanoparticles: (a) bright-field STEM image; (b) EDS position scans at Points 1–4 labeled on the image.

Spatially resolved elemental analysis of the nanoparticles was obtained with the TEM operating in scanning TEM (STEM) mode, using energy dispersive X-ray analysis (EDS). Fig. 4.4(a) shows a bright-field STEM image of a nanoparticle produced using a flow rate of 1.7 slm, with four points on the particle surface labeled for EDS analysis.

Fig. 4.4(b) shows the corresponding EDS energy spectra. Point 1 is located on a small darker particle, and is located off the edge of the large lighter-color particle; Point 2 is a bare portion of the surface of the large lighter-color particle; and both Points 3 and 4 are on small darker particles that lie on the surface of the large lighter-color particle. As the TEM grid was composed of copper and carbon, signals attributed to both Cu and C were detected at all locations. At Point 1, other than the Cu and C background, only Au is detected; at Point 2, only Si and O are detected; and at both Points 3 and 4 all of Au, Si and O are detected. These results are consistent with the expectation that the particle in Fig. 4.4(a) consists of a silica nanoparticle decorated with smaller gold nanoparticles.

4.3 PEGYLATION OF GOLD-DECORATED SILICA NANOPARTICLES

In this section, the details of the sequential gas-phase processes for PEGylating gold-decorated silica nanoparticles are described. Silica nanoparticle synthesis, gold nanoparticle synthesis, gold decoration onto the silica surfaces, and PEGylation are all accomplished in a continuous gas stream. Synthesis of gold-decorated silica nanoparticle has been discussed in the previous section. The PEGylation reaction scheme, which extends Calder's approach to PEGylating isolated gold nanoparticles [202], is illustrated in Fig. 4.5.

First, the gold-decorated silica nanoparticles are surface-modified with hydroxyl groups by reacting with ME. Thiols are well known to attach to the gold surface by an Au-S covalent bond [204]. At temperatures around 225 ℃ the thiols form disulfides [202], which adsorb to the gold surface, providing a monolayer of thiolated roots for PEG

growth. Then EO vapor is injected into the aerosol stream and exposed to elevated temperatures, thereby opening the ring structure of the thiolated monolayer and facilitating PEG growth by polymerization.

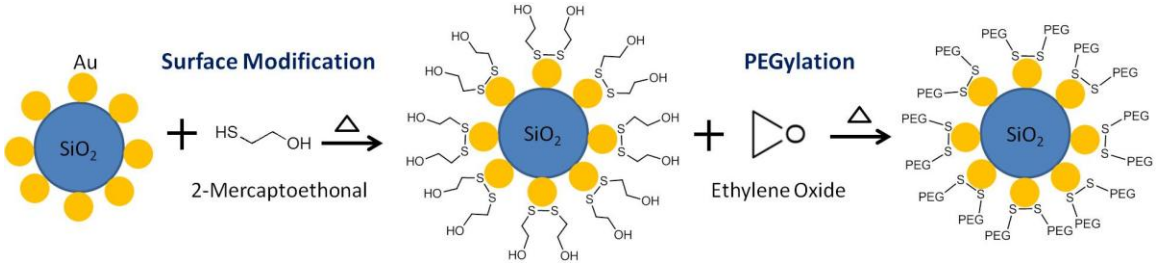

Figure 4.5 Reaction scheme for PEGylation of gold-decorated silica nanoparticles in the aerosol phase.

4.3.1 Experimental Procedure

The experimental setup used to produce SiO_2@Au@PEG nanoparticles is shown schematically in Fig. 4.6. The method used to produce an aerosol of gold-decorated silica nanoparticles is described by Boies et al. [198], as discussed in the previous section. In experiments conducted here, the tetraethylorthosilicate (TEOS) vapor (~0.018 sccm), which is carried by 10 sccm of nitrogen gas bubbling through the TEOS liquid bubbler, is mixed with 2.5 slm of nitrogen and sent into a decomposition furnace (900 ℃). An additional 2 slm of nitrogen is added before sending into the sintering furnace (1200 ℃) which spheroidizes any agglomerates.

Following the sintering furnace, the silica aerosol passes through a hot-wire chamber where gold nanoparticles are generated. The size distribution of the gold nanoparticles are controlled by adjusting the power of the wire and the flow rate of the nitrogen that passes over the wire, as previously described in Section 4.2.1. In the present

work, total nitrogen flow rate of ~4.5 slm set by the upstream conditions discussed above, was sending into the hot-wire chamber and the wire power was set to 19.2 W. The hot-wire chamber is followed by a gold decoration chamber, which increases the residence time for gold nanoparticle decoration on the larger silica nanoparticles.

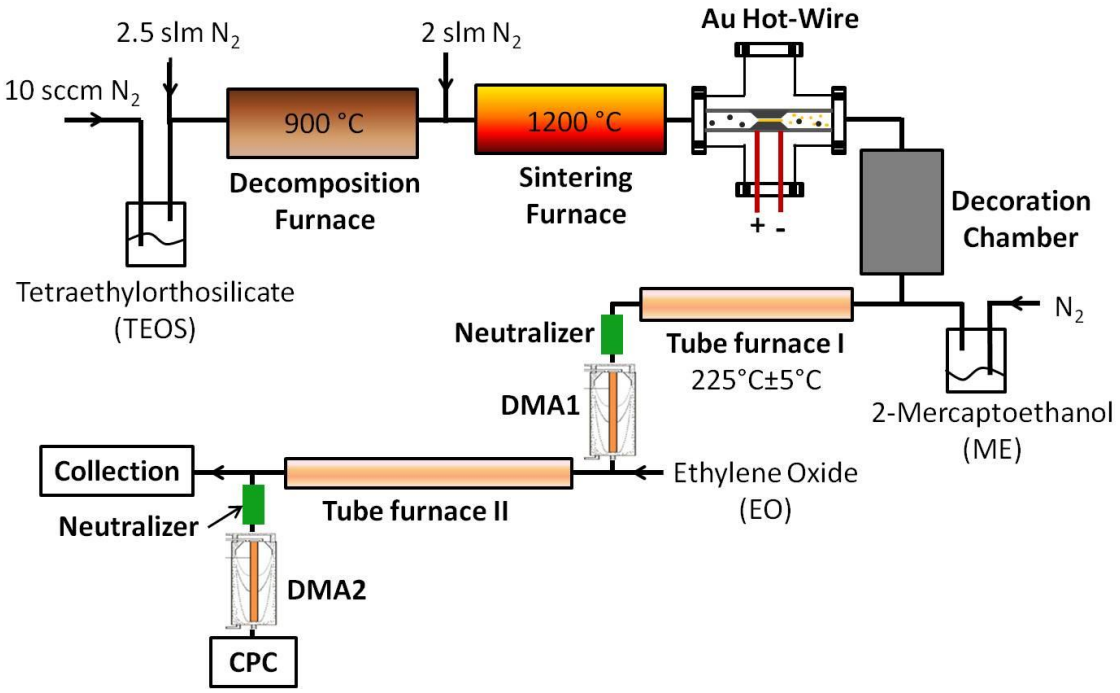

Figure 4.6 Schematic of experimental system for gas-phase synthesis of SiO_2@Au@PEG nanoparticles.

PEGylation of the gold-decorated silica nanoparticles is accomplished by means of the reaction scheme outlined in Fig. 4.5. The gold-decorated silica nanoparticles are functionalized with hydroxyl groups in a first tube furnace, set to 225±5 ℃, where ME vapor, generated by a bubbler, is introduced with 100 sccm of nitrogen carrier gas. The surface-modified nanoparticles together with EO vapor then flow through a second tube furnace, where PEGylation occurs. Final product is collected on stainless steel mesh and

silver filters (Sterlitech Corp.), as well as onto transmission electron microscopy (TEM) grids (Ted Pella 01890). Collected samples were characterized by TEM (Tecnai G ²F30), Fourier transform infrared spectroscopy (FTIR, Nicolet Magna 550), and X-ray photoelectron spectroscopy (XPS, Surface Science SSX-100).

Tandem differential mobility analysis was used to obtain online measurements of the increase in particle mobility diameter that occurred due to coating with PEG. The TDMA system consisted of two differential mobility analyzers, as described in Chapter 1, one upstream and the other downstream of the second tube furnace. Particles are charged to a known bipolar charge distribution before entering each DMA, using a neutralizer with a Po-210 radiation source. The first DMA passes only particles of specified mobility diameter. The second DMA, in series with a condensation particle counter, measures the size distribution of particles exiting the second furnace.

Experiments were conducted with variation of several operating parameters, including ME flow rates, EO flow rates, and temperatures of the second tube furnace.

4.3.2 Experimental Results and Discussion

For studies of the PEGylation process, the total aerosol flow was maintained at 4.5 slm as it passed through the hot-wire chamber, the decoration chamber, and the first tube furnace. At the exit of the first tube furnace, with the nanoparticles now surface-functionalized with ME, 1.0 slm of flow was sampled into the neutralizer and first DMA. The mobility-diameter-filtered output from the first DMA was then passed through the second tube furnace. Fig. 4.7 shows TDMA results for several cases where gold-

decorated nanoparticles with a mobility diameter of 39 nm were passed to the second tube furnace, whose temperature equaled 440 ℃±10 ℃. In Fig. 7(a), three scans are repeated under the same condition, with the EO vapor flow rate equaling 189 sccm; these three scans are also compared to the case without introduction of EO. The shift in the particle size distribution with introduction of EO is seen to be quite reproducible. The magnitude of the shift is characterized by fitting each of the main peaks to a Gaussian curve and then determining the shift in the peak of the Gaussian. (Small satellite peaks in the mobility distribution measurements are due to particles that are doubly charged by the neutralizer.) From this, introduction of 189 sccm of EO causes the particle mobility diameter to increase by approximately 9 nm. Assuming that these particles are spherical and that the diameter increase is due to PEGylation, this corresponds to a PEG coating thickness of ~4.5 nm, i.e., half the increase in diameter. Note that this figure represents the increase in particle mobility radius which does not necessarily equal the actual PEG chain size. As the EO flow rate increases, the particle size distribution shifts to the right, as seen in Fig. 7(b), indicating that the PEG coating thickness increases with increasing EO flow rate.

In addition to the EO flow rate, several other operating parameters affect the thickness of PEG coating. Fig. 4.8 shows the results of TDMA measurements of coating thickness, obtained in experiments in which the conditions varied included the temperature of the second tube furnace [Fig. 4.8(a)], the ME flow rate [Fig. 4.8(b)], and the presence or absence of the gold decoration chamber [Fig. 4.8(c)]. In all cases shown the mobility diameter selected by the first DMA (i.e., of the un-PEGylated particle)

equaled 39 nm, as in Fig. 4.7. In each case, the PEG thickness increased with EO flow rate, consistent with Fig. 4.7(b).

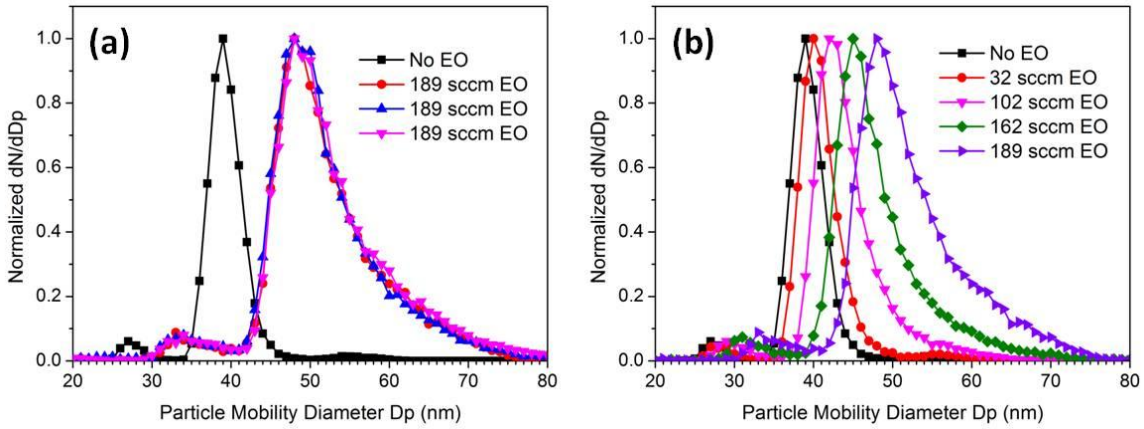

Figure 4.7 TDMA measurements of normalized particle size distributions of PEGylated gold-decorated silica nanoparticles: (a) repeated scans at 189 sccm of EO, compared to a case without introduction of EO; (b) with various EO flow rates.

For the experiments whose results are shown in Fig. 4.8(a), the temperature of the second tube furnace (i.e., the PEGylation temperature) was set to either 250, 340, or 440 ℃, while keeping other conditions the same (with the decoration chamber, and with 100 sccm of nitrogen carrier gas for ME). The results indicate that the PEGylation temperature is a critical parameter for PEG growth, with PEG growing much faster at 440 ℃ than at 250 ℃ or 340 ℃.

The ME flow rate is proportional to the flow rate of nitrogen in which the ME is carried. In Fig. 4.8(b), results of experiments are compared in which two different flow rates of N_2 carrier gas for delivering ME vapor were used, with presence of the decoration chamber and with PEGylation temperature at 440 ℃. Doubling the ME flow rate is seen to double (or slightly more than double) the coating thickness. Presumably

increasing the ME flow rate results in creation of more Au–S bonds, providing a greater density of terminal hydroxyl groups for initiation of PEGylation, and evidently, this in turn causes the coating thickness to increase. As discussed by Jokerst et al. [175], conditions of relatively low PEG grafting density lead to a "mushroom" conformation in which the PEG chains spread over the nanoparticle surface, while conditions of high grafting density produce a "brush-type" arrangement in with the PEG chains stick straight out from the particle surface. Thus, for the same PEG chain length (which is presumably related to the EO flow rate), a higher density of terminal hydroxyl groups that serve as PEGylation sites leads to a larger particle mobility diameter (hence, coating thickness), which is what is measured by TDMA.

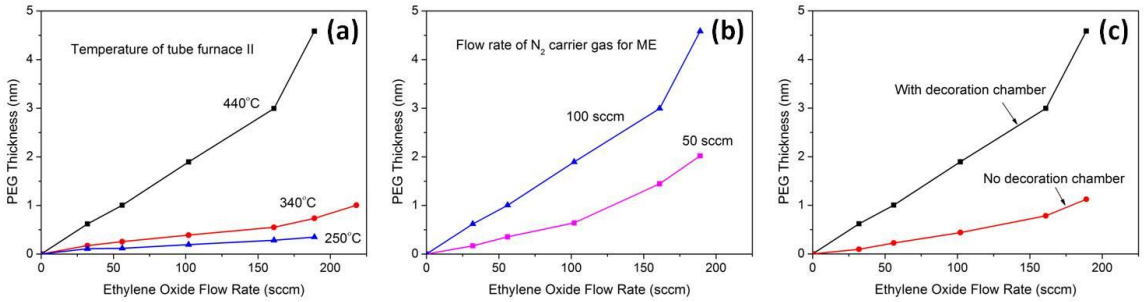

Figure 4.8 TDMA measurements of PEG coating thickness vs. EO flow rate: (a) with varying PEGylation temperature; (b) with varying ME carrier gas flow rate; (c) with/without inclusion of decoration chamber.

Fig. 4.8(c) shows the effect of including the decoration chamber, with experiments conducted using 100 sccm of nitrogen carrier gas for ME and the PEGylation temperature at 440 ℃. The decoration chamber provides longer residence time for the silica nanoparticles to scavenge the gold nanoparticles that are generated in the hot-wire chamber. While some degree of decoration is achieved by simply mixing the

silica and gold nanoparticles within the hot-wire chamber, adding the decoration chamber increases the gold nanoparticle decoration density [198]. Thus, similarly as in the case of increasing the ME flow rate, the density of available sites for initiation of PEGylation is increased by adding the decoration chamber. Consistent with this interpretation, Fig. 4.8(c) shows that the coating thickness is increased by adding the decoration chamber, for the same EO flow rate.

The chemical composition of the SiO_2@Au@PEG nanoparticles was characterized by means of EDS, XPS, and FTIR spectroscopy. Results shown are all for cases in which the decoration chamber was used, the flow rate of nitrogen carrier gas for the ME was 100 sccm, and the PEGylation temperature was 440 ℃.

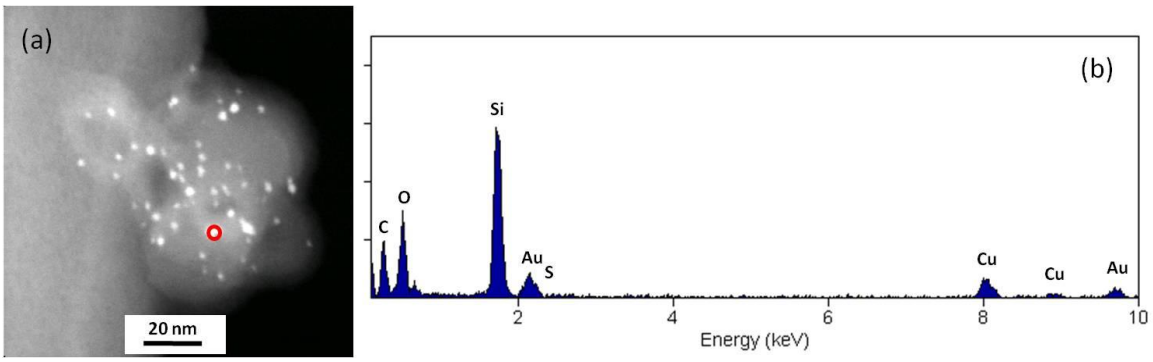

Figure 4.9 PEGylated gold-decorated silica nanoparticle: (a) dark-field STEM image; (b) EDS position scan of point labeled on image.

Fig. 4.9 shows a dark-field STEM image together with an EDS position scan of a PEGylated gold-decorated silica nanoparticle, obtained with an EO flow rate of 189 sccm**.** In dark-field STEM, the gold nanoparticles appear as bright dots. The EDS scan shown was carried out on one such bright dot, indicated by the red circle on the image. The results clearly show signals of Si, O, and Au, as expected for a gold-

decorated silica nanoparticle. A PEG coating is expected to produce signals from C and O, but, as carbon is present in the TEM grid and oxygen in the silica, EDS by itself cannot confirm the presence of PEG. Moreover, a signal from sulfur, expected from the thiol attachment to the gold, was too weak to be detected in the EDS scan, and therefore, requires confirmation by additional diagnostics.

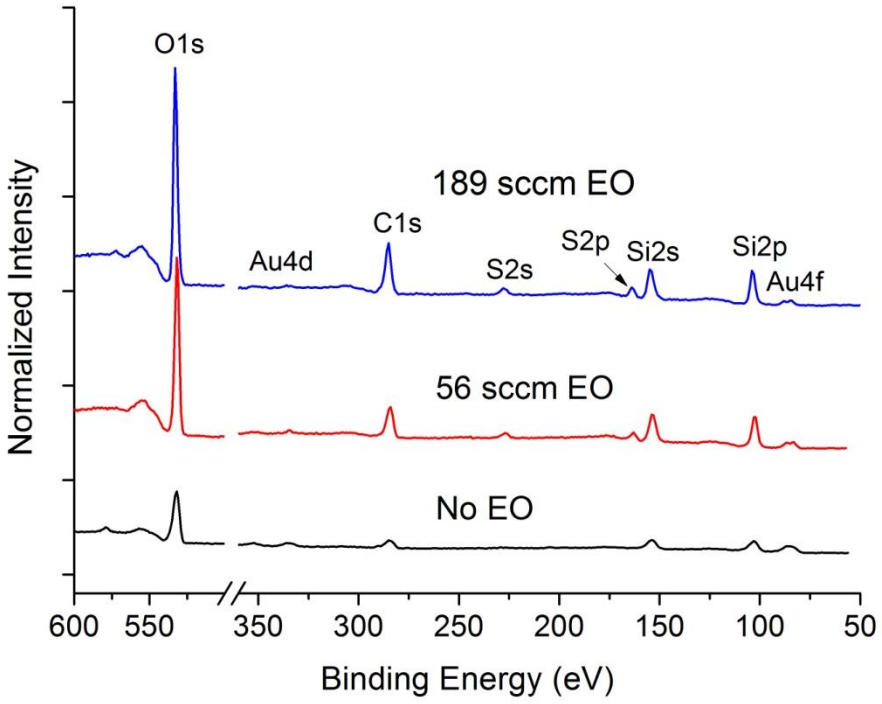

Figure 4.10 XPS survey scans of gold-decorated silica nanoparticles for various EO flow rate.

XPS elemental analyses were conducted of particles collected on silver membrane filters. Fig. 4.10 shows results for EO flow rates of 0, 56, and 189 sccm. Each scan is normalized by the Au 4f signal. As EO flow rate increases from 56 sccm to 189 sccm, the Si (2s and 2p) and S (2s and 2p) signal intensities are relatively unaffected, while the C 1s and O 1s signal intensities increase. This result is consistent with the TDMA results

showing that increasing the EO flow rate causes the coating thickness to increase. It should be noted that for the case of zero EO flow rate, where a thiolated monolayer is expected, some damage of the sample filters was observed after XPS analysis. The weakness of the sulfur signal in this case may have been at least partially caused by desorption of the monolayer thiol groups under X-ray radiation during XPS analysis.

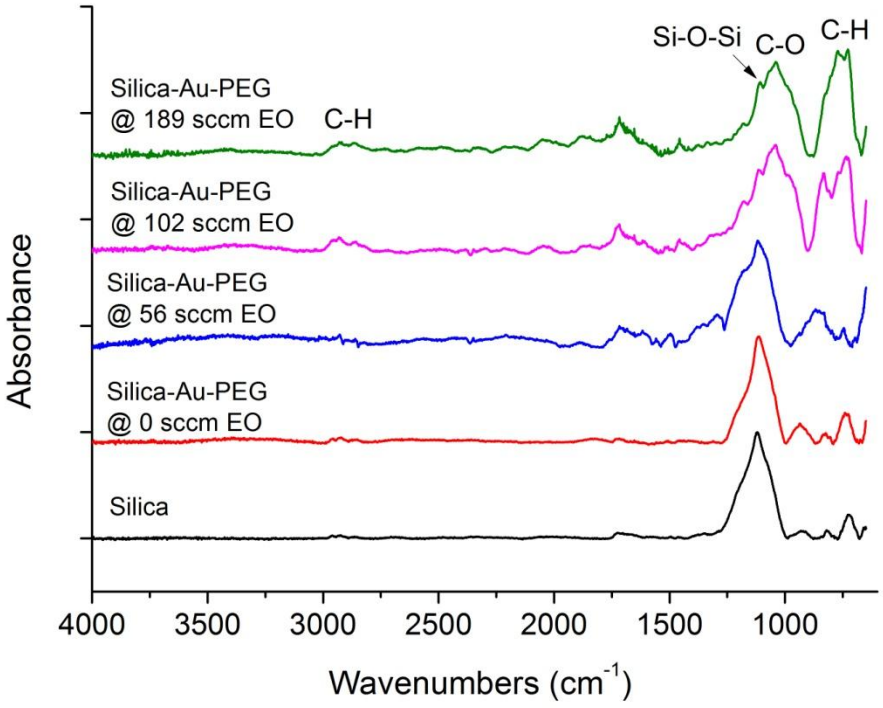

Figure 4.11 FTIR spectra of samples collected on stainless steel mesh.

The surface chemistry of the PEGylated particles was characterized by FTIR, as shown in Fig. 4.11. The signal associated with the Si–O–Si asymmetric stretching mode (~1110 cm^{-1}) shows for the case of pure silica as well as for all of the PEGylated gold-decorated nanoparticle samples. As the EO flow rate increases, the signal intensities of

the C–H stretching mode (2800-3000 cm^{-1}) and C–O stretching mode (~1040 cm^{-1}) increase, again consistent with the observation that PEG coating thickness increases with increasing EO flow rates.

4.4 SUMMARY

In summary, gold-decorated silica nanoparticles are obtained using the method developed by Boies et al. [198]. Different sizes of gold nanoparticles can be generated by controlling the power of the hot wire and the total gas flow rate over the wire. PEGylation has been achieved using a two-step aerosol process. In the first step, gold nanoparticles decorating the silica surface serve as sites for functionalization with a bifunctional reactant, 2-mercaptoethanol, at a temperature around 225 ℃, with a thiol group attaching to the gold nanoparticle and a terminal hydroxyl group at the other end. Ethylene oxide vapor is then introduced into the aerosol stream, and, at a temperature around 440 ℃, reacts with the hydroxyl group via a ring-opening polymerization to grow PEG. Increasing the ethylene oxide flow rate increases the PEG coating thickness. For given ethylene oxide flow rate, conditions that increase the surface density of sites available for PEGylation also cause coating thickness to increase, apparently because they lead to a more brush-type as opposed to mushroom configuration.

Chapter 5 Gas-Phase Synthesis of Gold-Decorated Silica-Coated Magnetic Iron Oxide Nanoparticles

5.1 BACKGROUND

Recently, multi-component nanoparticles have become very attractive, because they are able to combine multiple functions within one single unit. A tri-layer biofunctional magnetic/plasmonic nanoparticle contains a superparamagnetic iron oxide core (γ-Fe_2O_3 or Fe_3O_4), a continuous dielectric silica inner layer, and a gold outer layer. The magnetic core provides enhanced MRI for tumor detection and localized magnetic heating for hyperthermia therapy. The biocompatible silica layer reduces the coalescence of magnetic core particles and improves the chemical and thermal stabilities. The gold layer, which could be either a continuous gold shell or gold decoration on the surface, can be used for optical imaging and tumor destruction through laser ablation, due to the surface plasmon effect [33, 34]. These SPIO@SiO_2@Au tri-layer nanoparticles can serve both for cancer diagnostics and therapeutics [205-207].

Several groups reported synthesis of two-component gold-coated iron oxide (Fe_3O_4 or γ-Fe_2O_3) nanoparticles through wet chemistry methods [208-212]. Stoeva et al. [213] and Kim et al. [214] established synthesis of tri-layer nanoparticles composed of a silica core decorated with Fe_3O_4 nanoparticles and coated in a dense shell of gold nanoparticles. A few groups reported synthesis of "core-shell" structured SPIO@SiO_2@Au tri-layer nanoparticles associated with both magnetic and optical

properties. Salgueiriño-Maceira et al. established a structure consisting of a magnetic core, which contains several Fe_3O_4/γ-Fe_2O_3 nanoparticles of 8–10 nm, a silica inner shell with thickness of 80 nm, and a monolayer of gold nanoparticles of 15 nm [205]. Ji et al. also reported a similar structure with a SPIO-silica core (~70 nm), a gold nanoshell, (~8 nm), and biocompatible polyethylene glycol (PEG_{5000}) coatings on the surface [206]. Park et al. demonstrated the synthesis of nanocomposites of γ-Fe_2O_3 coated with silica and decorated with gold nanoparticles of 6 nm, using commercial superparamagnetic iron oxide nanoparticles of 12 nm as the magnetic core particles [207]. These nanocomposites had an overall diameter ~82 nm.

All currently reported SPIO@SiO_2@Au tri-layer nanostructures have been synthesized using wet chemistry with total nanoparticle size up to hundreds of nanometers. For biomedical applications, the overall size of the nanoparticles must be smaller than 100 nm [6, 215]. Gas-phase approaches show advantages for manufacturing multi-component nanoparticles with higher yield and better control of impurities and dimension of each layer. In Chapter 3, I have demonstrated our capability to coat superparamagnetic iron oxide nanoparticles with controllable thickness of silica, ranging from sub-nanometer to several nanometers, through a gas-phase photo-CVD method. Gold-decoration on silica nanoparticles was also successfully achieved using the approach developed by Boies et al. [198], as described in Chapter 4. In this chapter, the details of gold decoration on silica-coated magnetic iron oxide nanoparticles are described, which is the first approach for synthesis of SPIO@SiO_2@Au tri-layer nanoparticles through a series of gas-phase processes.

5.2 EXPERIMENTAL PROCEDURE

A schematic of the experimental system used to produce tri-layer SPIO@SiO_2@Au nanostructures is shown in Fig. 5.1. The details of the synthesis of superparamagnetic iron oxide nanoparticles and silica-coated iron oxide nanoparticles have been described in Chapter 2 and Chapter 3. The plasma torch was running at a current of 250 A, using 30 slm of argon and 5 slm of helium as the plasma gases. Iron precursor—ferrocene vapor—at a flow rate of ~7 sccm, was delivered by an argon carrier gas of 500 sccm passing through the precursor packed bed, which was heated to 120 ℃. A dilution argon gas of 1500 sccm and an additional oxygen gas of 20 sccm, introduced after the ferrocene precursor chamber, were injected into the plasma torch together with the ferrocene vapor. The plasma chamber was maintained at ~51 kPa. The produced iron oxide aerosol was extracted using an ejector driven by high-pressure nitrogen gas (~400 kPa). Only 1 slm of the diluted iron oxide aerosol was sampled into the photo-CVD chamber for silica coating and further gold decoration.

The photo-CVD chamber was maintained at 300 ℃. A purge flow of 3.5-slm nitrogen gas was injected into the CVD chamber, to keep the UV window clean from particle deposition. Silica precursor—TEOS vapor—was carried in a nitrogen gas bubbling through a liquid bubbler maintained in water bath at room temperature. The synthesized SPIO@SiO_2 nanoparticles were introduced directly into the gold hot-wire generator and decoration chamber for gold decoration. The final product was sampled into an SMPS system for on-line particle size distribution measurements. Particles were also collected on TEM lacy carbon grids (Ted Pella 01890) by an electrostatic

precipitator with an applied voltage at 3 kV located after the neutralizer. Particle morphology was characterized by high-resolution transmission electron microscopy (HRTEM), conducted on a Tecnai G^2 F30 electron microscope.

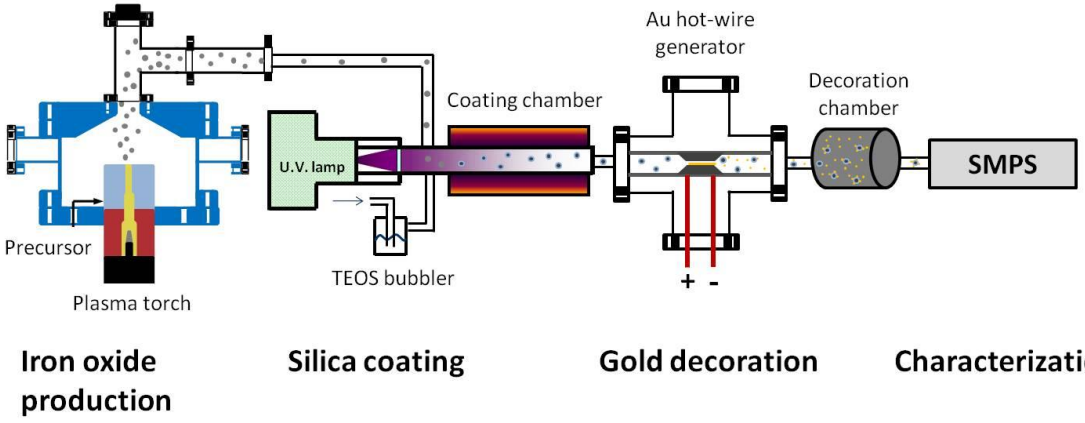

Figure 5.1 Experimental schematic for gas-phase synthesis of SPIO@SiO_2@Au tri-layer nanoparticles.

5.3 Experimental Results and Discussion

Without any injection of precursors (ferrocene and TEOS) and gold particle production (gold hot-wire power off), residue particles detected by SMPS in all cases were negligible in the gas lines, both for those with, and those without the decoration chamber cases, as shown in Fig. 5.2(a). From the previous section, I have shown that the size of the gold nanoparticles generated by the gold hot-wire generator can be controlled to diameters even smaller than 3 nm, a size that is under the SMPS detection limit. Fig. 5.2(b) shows the SMPS results of the pure gold nanoparticle size distribution with the presence and absence of the decoration chamber. Without the decoration chamber, almost

no gold nanoparticles were detected by SMPS at total N_2 flow rate of 4.5 slm when the hot-wire power was set at ~22.8 W, indicating that gold nanoparticles produced at the power of 22.8W were smaller than 3 nm. When the aerosol flow passed through the decoration chamber, lots of particles were detected at the same hot-wire power and total N_2 flow rate, which may indicate that small gold particles (< 3 nm), undetectable without the decoration chamber, form agglomerates in the decoration chamber and become large enough to be detected by the SMPS system. The agglomeration process of gold nanoparticles can be suppressed by shortening the residence time (i.e., without the decoration chamber) and decreasing the particle concentration (i.e., reducing the gold hot-wire power). Fig. 5.2(b) confirms that the detected particle concentration of gold agglomerate decreases when the hot-wire power reduced to ~20.5 W.

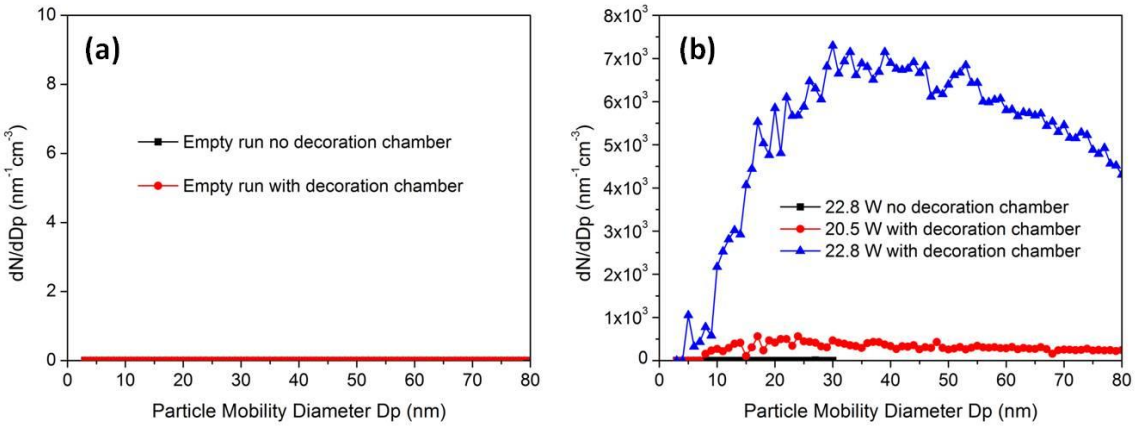

Figure 5.2 SPMS size distribution measurements: (a) empty run testing gas line contamination; (b) decoration chamber effect on pure gold nanoparticle size distribution.

SPIO@SiO_2 nanoparticles were introduced to the gold hot-wire generator and decoration chamber for gold decoration. The size distribution of gold-decorated silica-

coated superparamagnetic iron oxide nanoparticles were measured online with SMPS, as shown in Fig. 5.3. Each size distribution was normalized by the maximum concentration.

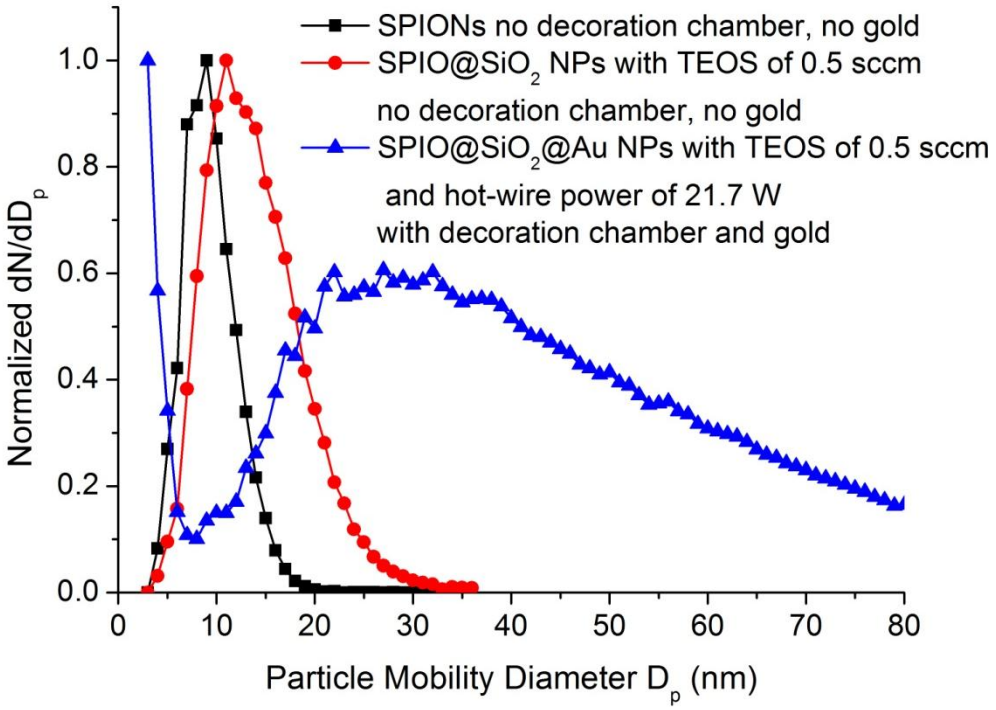

Figure 5.3 SMPS size distribution measurements of SPIO, SPIO@SiO_2, and SPIO@SiO_2@Au nanoparticles.

Without the decoration chamber and hot-wire power, we can see that the peak of the particle size distribution of bare SPIONs (fitted by LogNormal in Origin) is ~9 nm, while the peak of the size distribution of SPIO@SiO_2 nanoparticles increases ~5 nm with a TEOS flow rate of 0.5 sccm injected into the CVD chamber, corresponding to a silica thickness of ~2.5 nm. When gold hot-wire power operated at ~21.7 W and particles passed through the decoration chamber, the size distribution became broader and some small particles (< 5 nm) were also detected. These small particles could be residual gold agglomerates and the broader size distribution may be due to gold or SPIO@SiO_2 particle

agglomeration inside the decoration chamber. These are preliminary results for gold decoration on silica-coated iron oxide nanoparticles. Future study needs to further investigate the agglomeration process of pure core (SPIO@SiO_2) and gold particles inside the decoration chamber, the effect of core and gold particle sizes, and residence time on the gold coverage density on silica surfaces, and the effect of particle charges on particle collision inside the decoration chamber.

HRTEM images of SPIO@SiO_2@Au tri-component nanoparticles are shown in Fig. 5.4. These particles were collected on carbon grid. Iron oxide core nanoparticles (~8–10 nm) with crystal fringes are coated in the amorphous silica shell, labeled in the images. Small gold nanoparticles (~2–4 nm), shown as small darker dots due to their higher mass contrast, dispersed on the silica surfaces, indicating these particles had a three-layer structure.

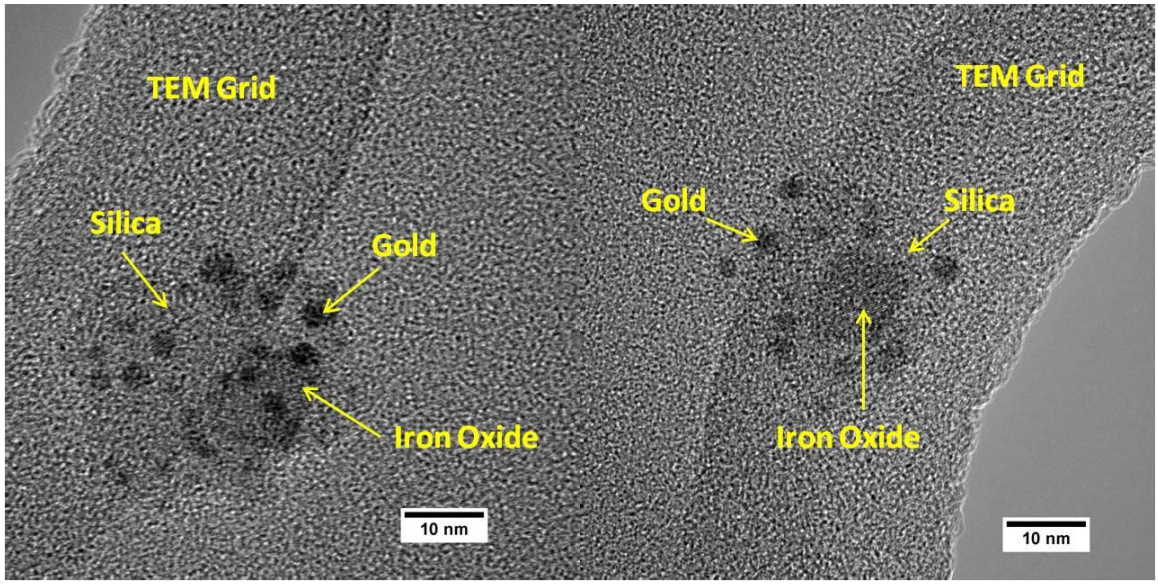

Figure 5.4 HRTEM images of SPIO@SiO_2@Au produced at TEOS flow rate of 0.5 sccm and gold hot-wire power of 21.7 W.

The elemental information of the three component nanoparticles was confirmed by EDS analysis in the STEM mode. The high resolution dark-field STEM image is shown in Fig. 5.5(a). Gold particles have higher mass contrast compared to iron oxide and silica, shown as small brighter dots in the image. The EDS position scans were conducted on Point 1 and 2, where Point 1 is on the core particle and Point 2 is on the small brighter dot, as labeled in red circles. The results of the EDS scans are shown in Fig. 5.5(b). Carbon signal from background of the TEM grid appears in both scans. As expected, at Point 1—the center core of silica-coated iron oxide nanoparticle—Fe, Si, and O signals were detected; at Point 2—gold particle on silica surface—Au, Si, and O signals were detected. These HRTEM and EDS results confirmed that these particles were gold-decorated silica-coated iron oxide nanonparticles.

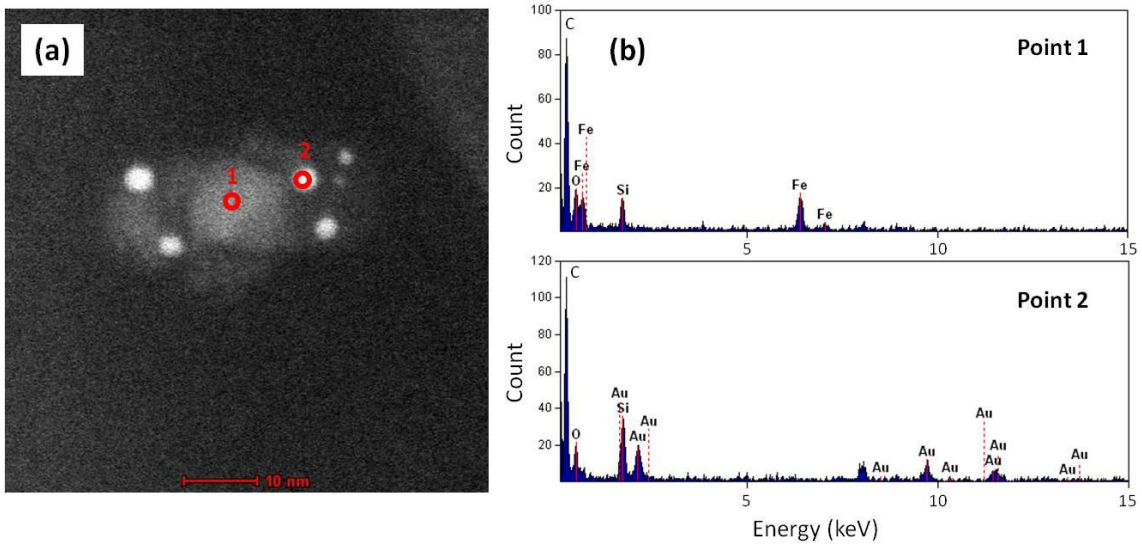

Figure 5.5 (a) Dark-field STEM image of SPIO@SiO_2@Au produced at TEOS flow rate of 0.5 sccm and gold hot-wire power of 21.7 W; (b) EDS results of Point 1 and 2 labeled in the image.

5.4 SUMMARY

In summary, preliminary results show that tri-component SPIO@SiO_2@Au nanoparticles has been achieved through a series of sequential gas-phase processes. Each component was synthesized in separate reaction chambers. The SPIONs were first produced by a thermal plasma, then coated with silica in the photo-CVD chamber, decorated with gold nanoparticles at the end by passing through the gold hot-wire generator and the decoration chamber. The morphology and elemental information of the synthesized tri-component nanoparticles were confirmed by HRTEM and EDS analysis. Future work will further explore the synthesis process of tri-layer SPIO@SiO_2@Au nanoparticles, such as dimension control of each component, control of gold coverage density on silica surfaces, the magnetic and optical properties of the tri-layer nanoparticles, and particle collection and dispersion in liquid solutions.

Chapter 6 Summary and Future Recommendations

6.1 SUMMARY

In summary, I described a gas-phase method for fabricating multi-layer structured multifunctional nanoparticles (SPIO@SiO_2@Au), which consist of a superparamagnetic iron oxide core, a continuous silica shell, and an outer layer decorated with gold nanoparticles. The gold and silica surfaces can serve for different surface functionalizations in future biomedical studies. Gas-phase PEGylation was investigated to grow hydrophilic polyethylene glycol coating on gold-decorated silica nanoparticles. The polyethylene glycol coating improves the biocompatibility and solubility of synthesized particles for biomedical applications.

Superparamagnetic iron oxide nanoparticles were synthesized by a DC thermal plasma using ferrocene as the iron precursor. Preliminary results found that the magnetic properties of synthesized products were strongly affected by the plasma type, plasma power, and ceramic tube position above the nozzle exit. Optimum SPIONs were obtained in an argon/helium plasma with the ceramic tube located at ~5 cm above the nozzle exit. An additional argon dilution of 1.5 slm injected downstream of the ferrocene packed bed decreased clogging inside the precursor delivery line. The particle size distribution and morphology of the synthesized particles were characterized by an online scanning mobility particle sizer system, and offline high-resolution TEM with particles collected on TEM grids. Results showed that the primary crystalline size of plasma-synthesized

nanoparticles was ~5–8 nm. The XRD and VSM results showed that the chemical phase composition and magnetic properties of the iron oxide nanoparticles were affected by the O_2 flow rates. Based on the VSM results, the synthesized nanoparticles exhibit superparamagnetism at room temperature. The best saturation magnetization (~40 emu/g) was achieved with an oxygen flow rate of 20 sccm, and these particles mainly contain the Fe_3O_4 phase.

Silica coating on iron oxide nanoparticles was obtained through a photo-induced CVD method using TEOS as the silica precursor. Iron oxide aerosols were sampled into the coating chamber by a nitrogen-driven ejector. The CVD chamber was set at 300 ℃. The TDMA and SMPS results showed that the silica thickness could be tuned between sub-nanometer to several nanometers by controlling the TEOS flow rates and total residence time inside the CVD chamber. High-resolution TEM and EDS results showed that the synthesized particles had a core-shell structure: a crystal iron oxide core and an amorphous silica shell. The surface chemistry of the synthesized particles was analyzed by FTIR. In the absorption spectra, the silica representative peaks (800, 970, and 1100 cm^{-1}) and hydroxyl groups (3450 cm^{-1}), as well as some C–H contamination peaks (2800–3000 cm^{-1} and 1300–1500 cm^{-1}), were observed for coated particles. The FTIR spectra also showed that the silica grew closer to the stoichiometric ratio as the coating thickness increased. The VSM measurements showed that the silica-coated iron oxide nanoparticles maintained superparamagnetism. Preliminary results showed that the saturation magnetization of silica-coated nanoparticles decreased compared to bare iron oxide nanoparticles that were collected directly from the plasma reactor. The

magnetization decreased because of the presence of the diamagnetic silica coating, since the hysteresis loops had been normalized by the total mass of particles collected on the filter. Continued study needs to further investigate the effect of the silica thickness on magnetic properties on a per-unit-mass base of iron or iron oxide.

PEGylation on gold-decorated silica nanoparticles was achieved by a two-step gas-phase process. The gold-decorated silica nanoparticles were synthesized with a gold hot-wire generator and a decoration chamber. The gold nanoparticle size could be controlled by the hot-wire power and total gas flow rate passing through the gold hot-wire chamber. Gas-phase PEGylation was investigated by first modifying the gold-decorated silica nanoparticles with hydroxyl groups using 2-mercaptoethanol; these surface modified nanoparticles were further reacted with ethylene oxide vapor at elevated temperatures to grow polyethylene glycol chains. TDMA results showed that the PEG thickness increased with the PEGylation temperature, ethylene oxide flow rates, and gold decoration density. EDS and XPS measurements, which showed Si, O, Au, and S signals, confirmed the elemental composition of the PEGylated particles.

Preliminary experiments in a series of sequential gas-phase processes achieved tri-layer SPIO@SiO_2@Au nanoparticles: the superparamagnetic iron oxide core synthesized in the thermal plasma chamber, silica coating grown in the photo-CVD chamber, and the gold decoration fabricated in the gold hot-wire and decoration chambers. High-resolution TEM results confirmed that the collected particles had a tri-component structure, containing an iron oxide crystal core, an intermediate amorphous silica shell, and small gold nanoparticles on the silica surface. EDS analysis showed the

presence of Fe, O, Si, and Au, as expected. Continued research will further study the stability of the synthesized particles dispersed in liquid solutions, the effect of silica coating in magnetic heating experiments, and the effect of gold nanoparticle sizes on optical properties. The tri-layer nanoparticles can be further coated with hydrophilic polyethylene glycol by a two-step gas-phase PEGylation method, as described in Chapter 4, to improve the biocompatibility and solubility of the synthesized particles.

6.2 Recommendations for Future Study

6.2.1 Improvements of Particle Synthesis Processes

Several improvements can be found to optimize the particle production rate. First, the particle production rate can be further improved by reducing the particle loss in the lines. Particles were observed deposited on the walls of the plasma reactor and downstream in the exhaust cooling sections, as seen in Fig. 6.1. Since the plasma reactor operates at high temperature, the particle loss is mainly due to the thermophoretic force which is proportional to the temperature gradient. Thus, redesigning the plasma chamber with a modified inner contour can reduce the particle deposition. Moreover, since the particles are in nano-size, the particle diffusion loss is also significant. Shortening the delivery lines between each synthesis chamber or providing additional heating around the delivery tubes will reduces the diffusion loss of particles in the delivery lines. In heating the delivery tubes, the wall temperature rises higher than the gas temperature inside. The

thermophoretic force will push the particles into the center of the pipe, reducing particle diffusion loss to the walls.

In the CVD coating process, only a small fraction of the plasma-synthesized SPIO aerosol was sampled into the CVD chamber to study the silica coating process. For a continuous particle production, it is desirable to send the whole plasma aerosol stream of ~37 slm into the CVD chamber to achieve a high production rate of SPIO@SiO_2 NPs. Thus, the coating chamber can be designed to be larger for high flow rate production with enough residence time, or multiple lamps (e.g., one close to the inlet and the other one close to the outlet of the CVD chamber) can be used to provide enough energy for coating processes with a high flow rate and a high particle concentration.

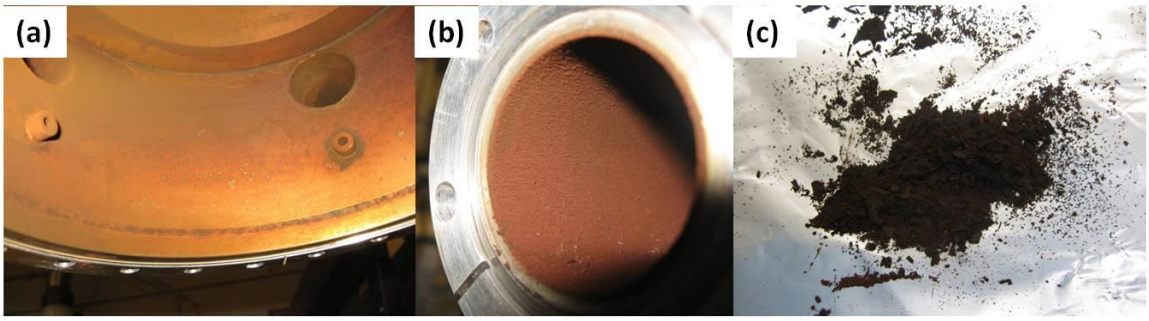

Figure 6.1 Particle deposition: (a) inside wall of the plasma chamber; (b) inside wall of the cooling section in the exhaust line; and (c) powder on aluminum foil, scratched from (a) and (b).

6.2.2 Particle Collection

The synthesized nanoparticles must be collected and dispersed into liquid solution (i.e., water), for further surface biofunctionalization and biomedical testing. Collecting aerosol particles on filters and then dispersing the collected particles into liquid solution by sonication is a simple process; however, the collection efficiency of this method is not

only limited by the filter collection and efficiency, but also the efficiency of the dispersion process, since particles are trapped inside the filter causing difficulties for particle retrieval. Moreover, particles easily form agglomerates on filters during the collection process and these agglomerates are difficult to break apart and disperse in the liquid solution. Designing an aerosol collection system to collect and disperse the synthesized nanoparticles directly into water will greatly improve the collection process.

One possible collection approach is to enlarge the nanoparticles into micron size by water condensation and then collect the micron-sized particles with an impactor, as seen in Fig. 6.2. The water condensation could be achieved by two methods. In Fig. 6.2(a), the gas-phase synthesized nanoparticles pass through a water-based growth tube, which consists of two regions, a cold and a heated region. Water vapor can diffuse through the wick into the central aerosol-stream tube, while aerosol nanoparticles cannot pass through the wick. Aerosol particles are cooled down upon passing through the cold region. In the heated region, the mass diffusivity of water is greater than the thermal diffusivity of the aerosol, thus water vapor molecules diffuse faster through the wick into the center tube, resulting in a supersaturated region in the center tube. In this region, the water vapor condenses on the cold nanoparticles that grow into micron-size droplets. After passing through the growth tube, the micron-size water droplets, which encapsulate the synthesized nanoparticles, are impacted into a water solution by inertia. The growth rate of the water droplets inside the growth tube is determined by the saturation ratio. The saturation ratio is controlled by the dimensions of the growth tube and the difference in temperature between the cold and heated regions. Supersaturation can be also achieved

by mixing the synthesized nanoparticles with saturated hot water vapor, such as steam, as shown in Fig. 6.2(b). Water vapor will condense on the cold nanoparticle surface resulting in particle growth. Then, the water-encapsulated particles can be collected into the liquid solution with an impactor.

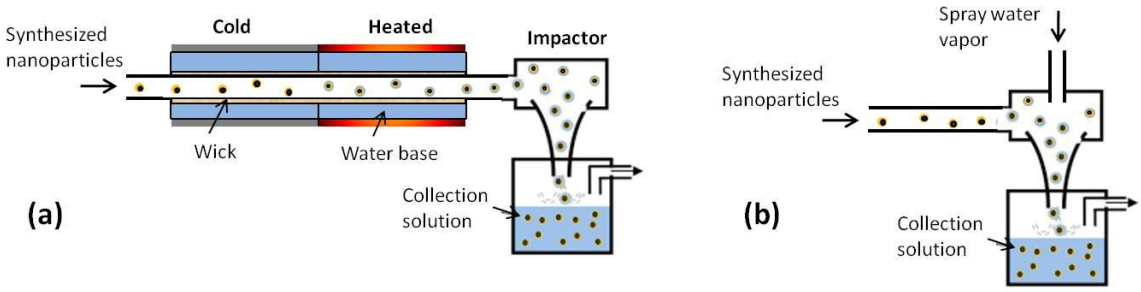

Figure 6.2 Nanoparticle collection by water condensation; supersaturation is achieved by (a) experiencing cold and heated region; (b) mixing with hot water vapor.

Another way to collect aerosol particles is by electrostatic force. In this method, the synthesized nanoparticles should first be charged (e.g. negative), and then passed through an electric field. If the collection solution is positioned at one electrode side (e.g., positive), the particles will be collected by the electrostatic force. A preliminary experiment was carried out to study collection efficiency using an electric field. A schematic of the aerosol collection system is shown in Fig. 6.3. Silica nanoparticles synthesized by thermal decomposition of TEOS precursor were used as the test particles. A bipolar charger (Po-210) was used to charge the particles. A glass bottle filled with water solution was used to collect the silica particles. Two electrodes were installed inside the glass bottle: the negative electrode positioned above the water surface and the positive one located inside the water solution. A high voltage D.C. power supply

(BERTAN model 205B-10R) was used to apply DC voltage between the electrodes. When negatively charged particles enter the glass bottle, the electrostatic force attracts them into the water solution. The inlet tube, a stainless steel tube with an outer diameter of D, is located at 2.5 cm from the water surface. A SMPS system was used inline to detect the uncollected particles. The preliminary test investigated the effect of the applied voltage and inlet tube diameter.

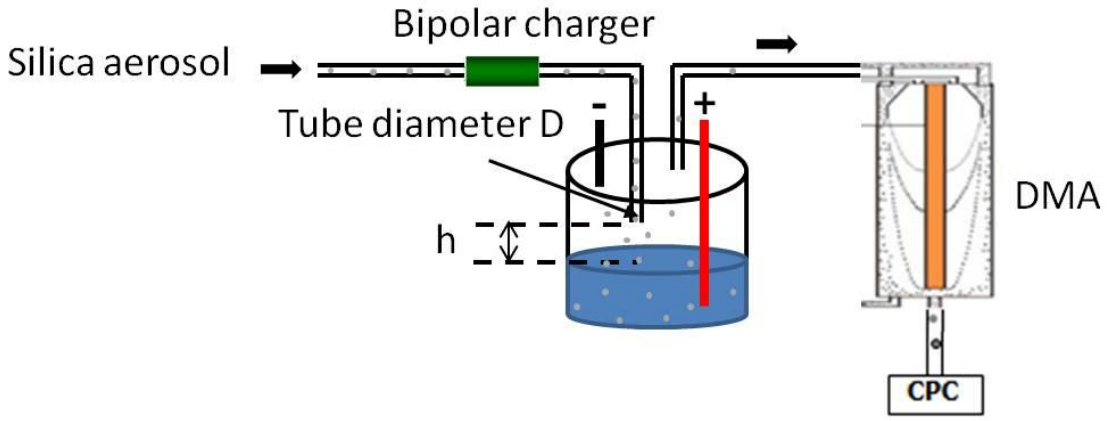

Figure 6.3 Schematic of an aerosol collection system using electrostatic force.

Both 6.4-mm and 25.4-mm stainless steel tubes were tested for use as inlet tubing. An applied voltage of 0–8 kV was studied for use in particle collection. Fig. 6.4 shows the SMPS results of particle size distributions for uncollected particles detected in the outlet. For both tube sizes, the detected particle concentration decreases as the applied voltage increases. The penetration efficiency (P) is defined as the fraction of the total number (or mass) of particles that pass through the electric field. Here, an assumption is made that $P = 1$ for the zero-voltage case. The number (or mass) collection efficiency equals $1 - P$. At an applied voltage of 8 kV, the calculated number collection efficiency

is ~64% for the 6.4-mm tube, ~89% for the 25.4-mm tube; the calculated mass collection efficiency is ~31% for the 6.4-mm tube, ~59% for the 25.4-mm tube. The SMPS results indicate that the collection efficiency increases as the applied voltage increases. The collection efficiency also increases as the inlet tube size increases, which may be because as the inlet size increases, the residence time increases, resulting in a longer interaction time between the charged particles and the electric field. These are preliminary test results, which may be helpful for design of future aerosol collector systems. Several improvements to particle collection include improving the particle charging efficiency and increasing the collection time. In order to achieve high collection efficiency, it is preferable to charge particles unipolarly. Thus, a unipolar charger can be used for particle charging, for example, by using a corona discharge. Particle charging and collection can occur in a chamber similar to a wet electrostatic precipitator [216]. In addition, a small water pump can be used for water recirculation to extend the collection time and raise particle concentration in the water solution.

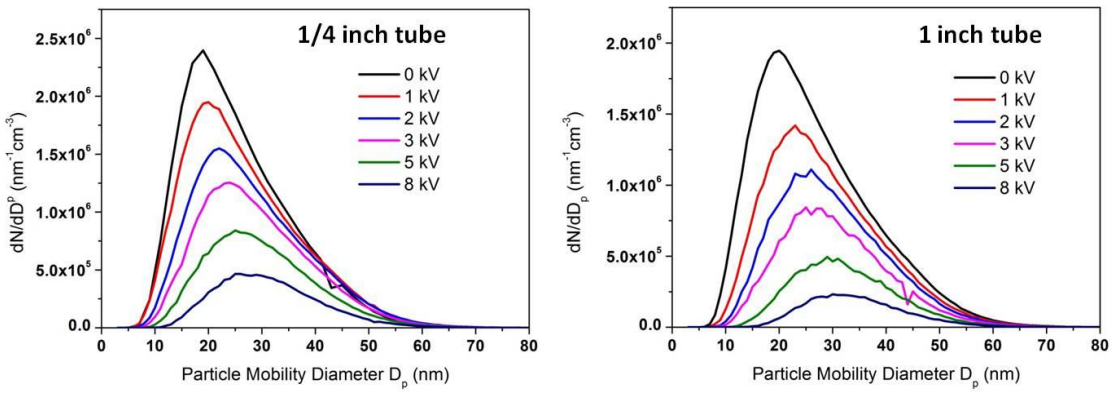

Figure 6.4 SMPS results of uncollected particles at varying voltages.

6.2.3 CONTINUOUS GOLD COATING

In Chapters 4 and 5, I described gold decoration on both silica and silica-coated magnetic iron oxide nanoparticles. These are isolated gold particles on silica surfaces. As mentioned in Chapter 1, small gold nanoparticles absorb radiation in the visible wavelength region. As isolated gold particles form a continuous gold shell, the absorption region moves into the near infrared (NIR). Since biological tissues have a low absorption in this region [176], the gold-coated particles are useful for in vivo hyperthermia. Future research can explore the synthesis of a continuous gold shell.

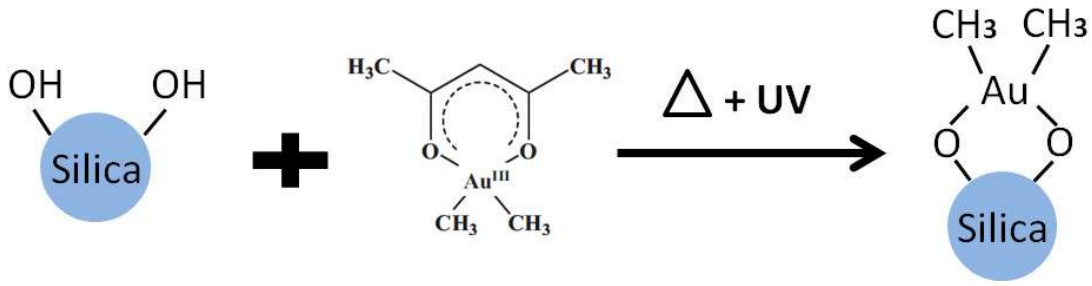

Figure 6.5 Reaction scheme for photo-CVD coating of continuous gold on silica NPs.

The photo-CVD method has been successfully used to grow organic coating on NaCl and Al nanoparticles [76], silica coating on Ag nanoparticles [43], and silica coating on superparamagnetic iron oxide nanoparticles (see Chapter 3). As seen in Fig. 6.5, a reasonable idea would be to explore the continuous gold coating via photo-CVD by dissociating a gold precursor in gas phase and forming a continuous gold layer on preexist core particles, such as silica nanoparticles. Okumura et al. reported the use of dimethyl gold acetylacetonate ($Me_2Au(acac)$) as the gold precursor for deposition of gold nanoparticlcles on the SiO_2 surface by physical adsorption and thermal decomposition of

the organometallic gold precursor [187]. $Me_2Au(acac)$ has a reasonable high vapor pressure and can be used as the gold precursor in the photo-CVD process. When the energy of the photons emitted by the UV lamp is high enough to dissociate the $Me_2Au(acac)$ precursor, gold films will grow on silica particles by means of chemical vapor deposition. The CVD temperature, precursor flow rates, and total residence time inside the CVD chamber, are some of the parameters that can be investigated for study of the gold shell growth on silica nanoparticles.

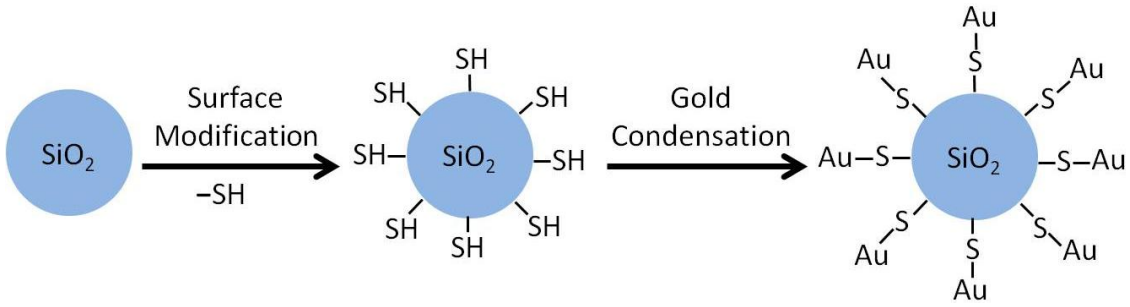

Figure 6.6 Reaction scheme for growth of continuous gold on silica NPs.

A continuous gold shell can potentially also be achieved on silica-based nanoparticles by a two-step gas-phase process, as shown in Fig. 6.6. In the first step, the silica particles are surface modified with a layer of thiol (–SH) groups. For example, (3-Mercaptopropyl)trimethoxysilane ($HS(CH_2)_3Si(OCH_3)_3$) can be used as the thiol precursor; it attaches to the silica surfaces by chemical reaction. Thiols are known to form covalent bonds with gold. In the second step, the surface-modified particles are mixed with gold vapor, which can be generated either through a high temperature furnace or a gold hot-wire generator, as discussed in previous chapters. Gold atoms or small gold particles will attach to the –SH groups forming a continuous gold layer. With such a two-

step gas-phase method, control of the temperature of the mixing process of –SH surface modified particles with gold vapor (or small gold particles) may be critical, since high temperatures could result in desorption of the –SH bonds from the surface of the particles.

References

1. N. A. Spaldin, Magnetic materials: fundamentals and device applications, 2003, Cambridge University Press.

2. R. M. Cornell and U. Schwertmann, The iron oxides: structure, properties, reactions, occurrences and uses, 2nd edn., 2003, Wiley-VCH, Weinheim.

3. M. A. Willard, L. K. Kurihara, E. E. Carpenter, S. Calvin, and V. G. Harris, "Chemically prepared magnetic nanoparticles," *International Materials Reviews*, 2004. **49**(3–4):125–170.

4. A.-H. Lu, E. L. Salabas, and F. Schüth, "Magnetic nanoparticles: synthesis, protection, functionalization, and application," *Angewandte Chemie International Edition*, 2007. **46**(8):1222–1244.

5. Q. A. Pankhurst, J. Connolly, S. K. Jones, and J. Dobson, "Applications of magnetic nanoparticles in biomedicine," *Journal of Physics D: Applied Physics*, 2003. **36**:R167–R181.

6. A. K. Gupta and M. Gupta, "Synthesis and surface engineering of iron oxide nanoparticles for biomedical applications," *Biomaterials*, 2005. **26**:3995–4021.

7. S. Laurent, D. Forge, M. Port, A. Roch, C. Robic, L. V. Elst, and R. N. Muller, "Magnetic iron oxide nanoparticles synthesis, stabilization, vectorization, physicochemical characterizations, and biological applications," *Chemistry Review*, 2008. **108**(6):2064–2110.

8. J. Gao, H. Gu, and B. Xu, "Multifunctional magnetic nanoparticles: design, synthesis, and biomedical applications," *Accounts of Chemical Research*, 2009. **42**(8):1097–1107.

9. R. Hao, R. Xing, Z. Xu, Y. Hou, S. Gao, and S. Sun, "Synthesis, functionalization, and biomedical applications of multifunctional magnetic nanoparticles," *Advanced Materials*, 2010. **22**(25):2729–2742.

10. J. Ward, K. S. Naik, J. A. Guthrie, D. Wilson, and P. J. Robinson, "Hepatic lesion detection: comparison of MR imaging after the administration of superparamagnetic iron oxide with dual-phase CT by using alternative-free

response receiver operating characteristic analysis," *Radiology*, 1999. **210**(2):459–466.

11. K. D. Hagspiel, K. F. Neidl, A. C. Eichenberger, W. Weder, and B. Marincek, "Detection of liver metastases: comparison of superparamagnetic iron oxide-enhanced and unenhanced MR imaging at 1.5 T with dynamic CT, intraoperative US, and percutaneous US," *Radiology*, 1995. **196**(2):471–478.

12. K. Hekimoglu, Y. Ustundag, A. Dusak, B. Kalaycioglu, H. Besir, H. Engin, and O. Erdem, "Small colorectal liver metastases: detection with SPIO-enhanced MRI in comparison with gadobenate dimeglumine-enhanced MRI and CT imaging," *European Journal of Radiology*, 2011. **77**(3):468–472.

13. A. Muhi, T. Ichikawa, U. Motosugi, H. Sou, H. Nakajima, K. Sano, M. Sano, S. Kato, T. Kitamura, Z. Fatima, K. Fukushima, H. Iino, Y. Mori, H. Fujii, and T. Araki, "Diagnosis of colorectal hepatic metastases: comparison of contrast-enhanced CT, contrast-enhanced US, superparamagnetic iron oxide-enhanced MRI, and gadoxetic acid-enhanced MRI," *Journal of Magnetic Resonance Imaging*, 2011. **34**(2):326–335.

14. S. Kumano, T. Murakami, T. Kim, M. Hori, A. Okada, T. Sugiura, Y. Noguchi, S. Kawata, K. Tomoda, and H. Nakamura, "Using superparamagnetic iron oxide-enhanced MRI to differentiate metastatic hepatic tumors and nonsolid benign lesions," *American Journal of Roentgenoloty*, 2003. **181**(5):1335–1339.

15. I. Rabias, D. Tsitrouli, E. Karakosta, T. Kehagias, G. Diamantopoulos, M. Fardis, D. Stamopoulos, T. G. Maris, P. Falaras, N. Zouridakis, N. Diamantis, G. Panayotou, D. A. Verganelakix, G. I. Drossopoulou, E. C. Tsilibari, and G. Paravassiliou, "Rapid magnetic heating treatment by highly charged maghemite nanoparticles on Wistar rats exocranial glioma tumors at microliter volume," *Biomicrofluidics*, 2010. **4**(2):024111.

16. K. Maier-Hauff, F. Ulrich, D. Nestler, H. Niehoff, P. Wust, B. Thiesen, H. Orawa, V. Budach, and A. Jordan, "Efficacy and safety of intratumoral thermotherapy using magnetic iron-oxide nanoparticles combined with external beam radiotherapy on patients with recurrent glioblastoma multiforme," *Journal of Neuro-Oncology*, 2011. **103**(2):317–324.

17. P. Landon, P. J. Collier, A. J. Papworth, C. J. Kiely, and G. J. Hutchings, "Direct formation of hydrogen peroxide from H_2/O_2 using a gold catalyst," *Chemical Communications*, 2002. (18):2058–2059.

18. M. Haruta, "Catalysis of gold nanoparticles deposited on metal oxides," *Cattech*, 2002. **6**(3):102−115.

19. A. Corma and H. Garcia, "Supported gold nanoparticles as catalysts for organic reactions," *Chemical Society Reviews*, 2008. **37**(9):2096−2126.

20. M. C. Daniel and D. Astruc, "Gold nanoparticles: assembly, supramolecular chemistry, quantum-size-related properties, and applications toward biology, catalysis, and nanotechnology," *Chemical Reviews*, 2004. **104**(1):293−346.

21. S. Paul, C. Pearson, A. Molloy, M. A. Cousins, M. Green, S. Kolliopoulou, P. Dimitrakis, P. Normand, D. Tsoukalas, and M. C. Petty, "Langmuir-Blodgett film deposition of metallic nanoparticles and their application to electronic memory structures," *Nano Letters*, 2003. **3**(4):533−536.

22. X. Luo, A. Morrin, A. J. Killard, and M. R. Smyth, "Application of nanoparticles in electrochemical sensors and biosensors," *Electroanalysis*, 2006. **18**(4):319−326.

23. K. Sokolov, M. Follen, J. Aaron, I. Pavlova, A. Malpica, R. Lotan, and R. Richards-Kortum, "Real-time vital optical imaging of precancer using anti-epidermal growth factor receptor antibodies conjugated to gold nanoparticles," *Cancer Research*, 2003. **63**(9):1999−2004.

24. P. K. Jain, K. S. Lee, I. H. El-Sayed, and M. A. El-Sayed, "Calculated absorption and scattering properties of gold nanoparticles of different size, shape, and composition: applications in biological imaging and biomedicine," *The Journal of Physical Chemistry B*, 2006. **110**(14):7238−7248.

25. R. Goel, N. Shah, R. Visaria, G. F. Paciotti, and J. C. Bischof, "Biodistribution of TNF-alpha coated gold nanoparticles in an in vivo model system," *Nanomedicine*, 2009. **4**(4):401−410.

26. I. H. El-Sayed, X. Huang, and M. A. El-Sayed, "Surface plasmon resonance scattering and absorption of anti-EGFR antibody conjugated gold nanoparticles in cancer diagnostics: applications in oral cancer," *Nano Letters*, 2005. **5**(5):829−834.

27. R. Popovtzer, A. Agrawal, N. A. Kotov, A. Popovtzer, J. Balter, T. E. Carey, and R. Kopelman, "Targeted gold nanoparticles enable molecular CT imaging of cancer," *Nano Letters*, 2008. **8**(12):4593–4596.

28. G. Peng, U. Tisch, O. Adams, M. Hakim, N. Shehada, Y. Y. Broza, S. Billan, R. Abdah-Bortnyak, A. Kuten, and H. Haick, "Diagnosing lung cancer in exhaled breath using gold nanoparticles," *Nature Nanotechnology*, 2009. **4**(10):669–673.

29. L. R. Hirsch, R. J. Stafford, J. A. Bankson, S. R. Sershen, B. Rivera, R. E. Price, J. D. Hazle, N. J. Halas, and J. L. West, "Nanoshell-mediated near-infrared thermal therapy of tumors under magnetic resonance guidance," *Proceedings of the National Academy of Sciences*, 2003. **100**(23):13549–13554.

30. D. P. O'Neal, L. R. Hirsch, N. J. Halas, J. D. Payne, and J. L. West, "Photo-thermal tumor ablation in mice using near infrared-absorbing nanoparticles," *Cancer Letters*, 2004. **209**(2):171–176.

31. I. H. El-Sayed, X. Huang, and M. A. El-Sayed, "Selective laser photo-thermal therapy of epithelial carcinoma using anti-EGFR antibody conjugated gold nanoparticles," *Cancer Letters*, 2006. **239**(1):129–135.

32. X. Huang, P. K. Jain, I. H. El-Sayed, and M. A. El-Sayed, "Plasmonic photothermal therapy (PPTT) using gold nanoparticles," *Lasers in Medical Science*, 2008. **23**(3):217–228.

33. S. Link and M. A. El-Sayed, "Size and temperature dependence of the plasmon absorption of colloidal gold nanoparticles," *Journal of Physical Chemistry B*, 1999. **103**(21):4212–4217.

34. C. Loo, A. Lin, L. Hirsch, M.-H. Lee, J. Barton, N. Halas, JenniferWest, and R. Drezek, "Nanoshell-enabled photonics-based imaging and therapy of cancer," *Technology in Cancer Research & Treatment*, 2004. **3**(1):33–40.

35. A. Wiedensohler, "An approximation of the bipolar charge distribution for particles in the submicron size range," *Journal of Aerosol Science*, 1988. **19**(3):387–389.

36. M. D. Allen and O. G. Raabe, "Slip correction measurements of spherical solid aerosol particles in an improved millikan apparatus," *Aerosol Science and Technology*, 1985. **4**(3):269–286.

37. TSI, Series 3080 electrostatic classifiers operation and service manual, 2008.

38. E. O. Knutson and K. T. Whitby, "Aerosol classification by electric mobility: apparatus, theory, and applications," *Aerosol Science*, 1975. **6**(6):443–451.

39. B. Y. H. Liu, D. Y. H. Pui, K. T. Whitby, D. B. Kittelson, Y. Kousaka, and R. L. McKenzie, "The aerosol mobility chromatograph: a new detector for sulfuric acid aerosols," *Atmospheric Environment* 1978. **12**(1–3):99–104.

40. P. H. McMurry, H. Takano, and G. R. Anderson, "Study of the ammonia (gas)-sulfuric acid (aerosol) reaction rate," *Environmental Science & Technology*, 1983. **17**(6):347–352.

41. D. J. Rader and P. H. McMurry, "Application of the tandem differential mobility analyzer to studies of droplet growth or evaporation," *Journal of Aerosol Science*, 1986. **17**(5):771–787.

42. B. Zhang, Y.-C. Liao, S. Girshick, and J. Roberts, "Growth of coatings on nanoparticles by photoinduced chemical vapor deposition," *Journal of Nanoparticle Research*, 2008. **10**(1):173–178.

43. A. M. Boies, J. T. Roberts, S. L. Girshick, B. Zhang, T. Nakamura, and A. Mochizuki, "SiO_2 coating of silver nanoparticles by photoinduced chemical vapor deposition," *Nanotechnology*, 2009. **20**(29):295604.

44. D. Sun and Y. Yu, "Superparamagnetic iron oxide nanoparticle 'theranostics' for multimodality tumor imaging, gene delivery, targeted drug and prodrug delivery," *Expert Review of Clinical Pharmacology*, 2010. **3**(1):117–130.

45. A. J. Cole, V. C. Yang, and A. E. David, "Cancer theranostics: the rise of targeted magnetic nanoparticles," *Trends in Biotechnology*, 2011. **29**(7):323–332.

46. F. M. Kievit and M. Zhang, "Surface engineering of iron oxide nanoparticles for targeted cancer therapy," *Accounts of Chemical Research*, 2011. **44**(10):853–862.

47. J.-R. Jeong, S.-J. Lee, J.-D. Kim, and S.-C. Shin, "Magnetic properties of γ-Fe_2O_3 nanoparticles made by coprecipitation method," *Physica Status Solidi (b)*, 2004. **241**(7):1593–1596.

48. G. F. Goya and M. P. Morales, "Field dependence of blocking temperature in magnetite nanoparticles," *Journal of Metastable and Nanocrystalline Materials*, 2004. **20–21**:673–678.

49. E. D. Smolensky, H.-Y. E. Park, T. S. Berquo, and V. C. Pierre, "Surface functionalization of magnetic iron oxide nanoparticles for MRI applications-effect of anchoring group and ligand exchange protocol," *Contrast Media & Molecular Imaging*, 2010. **6**(4):189–199.

50. A. Teleki, M. Suter, P. R. Kidambi, O. Ergeneman, F. Krumeich, B. J. Nelson, and S. E. Pratsinis, "Hermetically coated superparamagnetic Fe_2O_3 Particles with SiO_2 nanofilms," *Chemistry of Materials*, 2009. **21**(10):2094–2100.

51. S. Calder, A. Boies, P. Lei, S. Girshick, and J. Roberts, "Photo-assisted hydrosilylation of silicon nanoparticles: dependence of particle size on grafting chemistry," *Chemistry of Materials*, 2011. **23**(11):2917–2921.

52. T. Yoshida and K. Akashi, "Preparation of ultrafine iron particles using an RF plasma," *Transactions of Japan Institute of Metals*, 1981. **22**(6):371–378.

53. S. L. Girshick, C.-P. Chiu, R. Muno, C. Y. Wu, L. Yang, S. K. Singh, and P. H. McMurry, "Thermal plasma synthesis of ultrafine iron particles," *Journal of Aerosol Science*, 1993. **24**(3):367–382.

54. C. Chou and J. Philips, "Plasma production of metallic nanoparticles," *Journal of Material Research*, 1992. **7**(8):2107–2113.

55. D. Vollath, D. V. Szabo, R. D. Taylor, J. O. Willis, and K. E. Sickafus, "Synthesis and properties of nanocrystalline superparamagnetic γ-Fe_2O_3," *NanoStructured Materials*, 1995. **6**(5–8):941–944.

56. D. Vollath, D. V. Szabo, R. D. Taylor, and J. O. Willis, "Synthesis and magnetic properties of nanostructured maghemite," *Journal of Material Research*, 1997. **12**(8):2175-2182.

57. R. Kalyanaraman, S. Yoo, M. S. Krupashankara, T. S. Sudarshan, and R. J. Dowding, "Synthesis and consolidation of iron nanopowders," *Nanostructured Materials*, 1998. **10**(8):1379–1392.

58. C. Janzen, H. Wiggers, J. Knipping, and P. Roth, "Formation and in situ sizing of gamma-Fe_2O_3 nanoparticles in a microwave flow reactor," *Journal of Nanoscience and Nanotechnology*, 2001. **1**(2):221–225.

59. S.-Z. Li, Y. C. Hong, H. S. Uhm, and Z.-K. Li, "Synthesis of nanocrystalline iron oxide particles by microwave plasma jet at atmospheric pressure," *Japanese Journal of Applied Physics*, 2004. **43**:7714–7717.

60. L. Zajíčková, P. Synek, O. Jašek, M. Eliáš, B. David, J. Buršík, N. Pizúrová, R. Hanzlíková, and L. Lazar, "Synthesis of carbon nanotubes and iron oxide nanoparticles in MW plasma with $Fe(CO)_5$ in gas feed," *Applied Surface Science*, 2009. **255**(10):5421–5424.

61. B. David, N. Pizúrová, O. Schneeweiss, V. Kudrle, O. Jašek, and P. Synek, "Iron-based nanopowders containing alfa-Fe, Fe_3C, and gamma-Fe particles synthesised in microwave torch plasma and investigated with Mossbauer Spectroscopy," *Japanese Journal of Applied Physics*, 2011. **50**(8):08JF11.

62. P. Synek, O. Jašek, L. Zajíčková, B. David, V. Kudrle, and N. Pizúrová, "Plasmachemical synthesis of maghemite nanoparticles in atmospheric pressure microwave torch," *Materials Letters*, 2011. **65**(6):982–984.

63. I. Bica, "Nanoparticle production by plasma," *Materials Science and Engineering*, 1999. **B68**(1):5–9.

64. C. Balasubramaniam, Y. B. Khollam, I. Banerjee, P. P. Bakare, S. K. Date, A. K. Das, and S. V. Bhoraskar, "DC thermal arc-plasma preparation of nanometric and stoichiometric spherical magnetite (Fe_3O_4) powders," *Materials Letters*, 2004. **58**(30):3958–3962.

65. I. Banerjee, Y. B. Khollam, S. K. Mahapatra, A. K. Das, and S. V. Bhoraskar, "Study of the effect of plasma-striking atmosphere on Fe-oxidation in thermal dc arc-plasma processing," *Journal of Vacuum Science & Technology A*, 2010. **28**(6):1399–1403.

66. C. Chazelas, J. F. Coudert, J. Jarrige, and P. Fauchais, "Synthesis of ultra fine particles by plasma transferred arc: Influence of anode material on particle properties," *Journal of the European Ceramic Society*, 2006. **26**(16):3499–3507.

67. I. Banerjee, Y. B. Khollam, C. Balasubramanian, R. Pasricha, P. P. Bakare, K. R. Patil, A. K. Das, and S. V. Bhoraskar, "Preparation of γ-Fe_2O_3 nanoparticles using DC thermal arc-plasma route, their characterization and magnetic properties," *Scripta Materialia*, 2006. **54**(1):1235–1240.

68. V. Subramanian, R. Baskaran, and H. Krishnan, "Thermal plasma synthesis of iron oxide aerosols and their characteristics," *Aerosol and Air Quality Research*, 2009. **9**(2):172–186.

69. D. N. McIlroy, D. Zhang, M. G. Norton, W. L. O'Brien, M. M. Schwickert, and G. R. Harp, "Synthesis and reactivity of Fe nanoparticles embedded in a semi-insulating matrix," *Journal of Applied Physics*, 2000. **87**(10):7213–7217.

70. D. N. McIlroy, J. Huso, Y. Kranov, J. Marchinek, C. Ebert, S. Moore, E. Marji, R. Gandy, Y.-K. Hong, M. G. Norton, E. Cavalieri, R. Benz, B. L. Justus, and A. Rosenberg, "Nanoparticle formation in microchannel glass by plasma enhanced chemical vapor deposition," *Journal of Applied Physics*, 2003. **93**(9):5643–5649.

71. A. Kouprine, F. Gitzhofer, M. Boulos, and T. Veres, "Synthesis of ferromagnetic nanopowders from iron pentacarbonyl in capacitively coupled RF plasma," *Carbon*, 2006. **44**(13):2593–2601.

72. V. Panchal, M. Neergat, and U. Bhandarkar, "Synthesis and characterization of carbon coated nanoparticles produced by a continuous low-pressure plasma process," *Journal of Nanoparticle Research*, 2011. **13**(9):3825–3833.

73. V. Panchal, G. Lahoti, U. Bhandarkar, and M. Neergat, "The effects of process parameters on yield and properties of iron nanoparticles from ferrocene in a low-pressure plasma," *Journal of Physics D: Applied Physics*, 2011. **44**(34):345205.

74. D. J. Dunlop and Ö. Özdemir, Rock magnetism: fundamentals and frontiers, 1997, Cambridge University Press.

75. Q. H. Powell, G. P. Fotou, T. T. Kodas, and B. M. Anderson, "Synthesis of alumina- and alumina/silica-coated titania particles in an aerosol flow reactor," *Chemistry of Materials*, 1997. **9**(3):685–693.

76. B. Zhang, Thermal plasma synthesis and photoinduced coating of aluminum nanoparticles, Ph.D. thesis, 2007, University of Minnesota.

77. R. Jain, S. L. Girshick, J. V. Heberlein, R. Mukherjee, B. Zhang, T. Nakamura, and A. Mochizuki, "Direct synthesis of yttrium aluminum garnet particles in an inductively coupled radio-frequency plasma system," *Plasma Chemistry and Plasma Processing*, 2010. **30**(6):795–811.

78. M. J. S. Monte, L. M. N. B. F. Santos, M. Fulem, J. M. S. Fonseca, and C. A. D. Sousa, "New static apparatus and vapor pressure of reference materials: naphthalene, benzoic acid, benzophenone, and ferrocene," *Journal of Chemical & Engineering Data*, 2006. **51**(2):757–766.

79. D. J. Hansen, Characterization of an argon-hydrogen thermal plasma expansion reactor used for nanoparticle synthesis, M.S. thesis, 1995, University of Minnesota.

80. A. Gidwani, Studies of flow and particle transport in hypersonic plasma particle deposition and aerodynamic focusing, Ph.D. thesis, 2003, University of Minnesota.

81. X. Wang, J. Hafiz, R. Mukherjee, T. Renault, J. Heberlein, S. L. Girshick, and P. H. McMurry, "System for in-situ characterization of nanoparticles synthesized in a thermal plasma process," *Plasma Chemistry and Plasma Processing*, 2005. **25**(5):439–453.

82. S. K. Friedlander and C. S. Wang, "The self-preserving particle size distribution for coagulation by Brownian motion," *Journal of Colloid and Interface Science*, 1966. **22**(2):126–132.

83. M. J. Benitez, D. Mishra, P. Szary, G. A. B. Confalonieri, M. Feyen, A. H. Lu, L. Agudo, G. Eggeler, O. Petracic, and H. Zabel, "Structural and magnetic characterization of self-assembled iron oxide nanoparticle arrays," *Journal of Physics: Condensed Matter*, 2011. **23**:126003.

84. H. Danan, A. Herr, and A. J. P. Meyer, "New determinations of the saturation magnetization of nickel and iron," *Journal of Applied Physics*, 1968. **39**(2):669–670.

85. A. E. Bberkowitz, W. J. Schuele, and P. J. Flanders, "Influence of crystallite size on the magnetic properties of acicular γ-Fe_2O_3 particles," *Journal of Applied Physics*, 1968. **39**(2):1261–1263.

86. J. M. D. Coey, "Nonlinear spin arrangement in ultrafine ferrimagnetic crystallites," *Phisical Review Letters*, 1971. **27**(17):1140–1142.

87. J. Frenkel and J. Doefman, "Spontaneous and induced magnetisation in ferromagnetic bodies," *Nature*, 1930. **126**:274–275.

88. D. Li, W. Y. Teoh, C. Selomulya, R. C. Woodward, P. Munroe, and R. Amal, "Insight into microstructural and magnetic properties of flame-made γ-Fe_2O_3 nanoparticles," *Journal of Materials Chemistry*, 2007. **17**:4876–4884.

89. E. D. Smolensky, M. C. Neary, Y. Zhou, T. S. Berquo, and V. C. Pierre, "Fe_3O_4@organic@Au: core–shell nanocomposites with high saturation magnetisation as magnetoplasmonic MRI contrast agents," *Chemical Communications*, 2011. **47**:2149–2151.

90. D. J. Dunlop, "Transition warming and cooling remanences in magnetite," *Journal of Geophysical Research*, 2007. **112**:B11103.

91. E. J. W. Verwey, "Electronic conduction of magnetite (Fe_3O_4) and its transition point at low temperatures," *Nature*, 1939. **144**:327–328.

92. Ö. Özdemir and D. J. Dunlop, "Hallmarks of maghemitization in low-temperature remanence cycling of partially oxidized magnetite nanoparticles," *Journal of Geophysical Reserach*, 2010. **115**:B02101.

93. D. Maity, S.-G. Choo, J. Yi, J. Ding, and J. M. Xue, "Synthesis of magnetite nanoparticles via a solvent-free thermal decomposition route," *Journal of Magnetism and Magnetic Materials*, 2009. **321**(9):1256–1259.

94. B. D. Cullity and C. D. Graham, Introduction to magnetic materials, 2nd edn., 2009, Wiley.

95. P. Guardia, B. Batlle-Brugal, A. G. Roca, O. Iglesias, M. P. Morales, C. J. Serna, A. Labarta, and X. Batlle, "Surfactant effects in magnetite nanoparticles of controlled size," *Journal of Magnetism and Magnetic Materials*, 2007. **316**(2):e756–e759.

96. N. Rao, S. Girshick, J. Heberlein, P. McMurry, M. Bench, S. Jones, D. Hansen, and B. Micheel, "Nanoparticle formation using a plasma expansion process," *Plasma Chemistry and Plasma Processing*, 1995. **15**(4):581–607.

97. M. R. Zachariah, M. I. Aquino, R. D. Shull, and E. B. Steel, "Formation of superparamagnetic nanocomposites from vapor phase condensation in a flame," *Nanostructured Materials*, 1995. **5**(4):383–392.

98. C. Janzen, J. Knipping, B. Rellinghaus, and P. Roth, "Formation of silica-embedded iron-oxide nanoparticles in low-pressure flames," *Journal of Nanoparticle Research*, 2003. **5**(5–6):589–596.

99. D. Li, W. Y. Teoh, R. C. Woodward, J. D. Cashion, C. Selomulya, and R. Amal, "Evolution of morphology and magnetic properties in silica/maghemite nanocomposites," *Journal of Physical Chemistry C*, 2009. **113**(28):12040–12047.

100. R. Strobel and S. E. Pratsinis, "Direct synthesis of maghemite, magnetite and wustite nanoparticles by flame spray pyrolysis," *Advanced Powder Technology*, 2009. **20**(2):190–194.

101. B. Guo, H. Yim, A. Khasanov, and J. Stevens, "Formation of magnetic Fe_xO_y/silica core-shell particles in a one-step flame aerosol process," *Aerosol Science and Technology*, 2010. **44**(4):281–291.

102. B. M. Kumfer, K. Shinoda, B. Jeyadevan, and I. M. Kennedy, "Gas-phase flame synthesis and properties of magnetic iron oxide nanoparticles with reduced oxidation state," *Journal of Aerosol Science*, 2010. **41**(3):257–265.

103. I. I. Slowing, B. G. Trewyn, S. Giri, and V. S.-Y. Lin, "Mesoporous silica nanoparticles for drug delivery and biosensing applications," *Advanced Functional Materials*, 2007. **17**(8):1225–1236.

104. I. I. Slowing, J. L. Vivero-Escoto, C.-W. Wu, and V. S.-Y. Lin, "Mesoporous silica nanoparticles as controlled release drug delivery and gene transfection carriers," *Advanced Drug Delivery Reviews*, 2008. **60**(11):1278–1288.

105. C. Barbé, J. Bartlett, L. Kong, K. Finnie, H. Q. Lin, M. Larkin, S. Calleja, A. Bush, and G. Calleja, "Silica particles: a novel drug-delivery system," *Advanced Materials*, 2004. **16**(21):1959–1966.

106. M. Vallet-Regí, F. Balas, and D. Arcos, "Mesoporous materials for drug delivery," *Angewandte Chemie International Edition*, 2007. **46**(40):7548–7558.

107. J. L. Vivero-Escoto, I. I. Slowing, B. G. Trewyn, and V. S. Y. Lin, "Mesoporous silica nanoparticles for intracellular controlled drug delivery," *Small*, 2010. **6**(18):1952–1967.

108. J. Lu, M. Liong, Z. Li, J. I. Zink, and F. Tamanoi, "Biocompatibility, biodistribution, and drug-delivery efficiency of mesoporous silica nanoparticles for cancer therapy in animals," *Small*, 2010. **6**(16):1794–1805.

109. F. Tang, L. Li, and D. Chen, "Mesoporous silica nanoparticles: synthesis, biocompatibility and drug delivery," *Advanced Materials*, 2012. **24**(12):1504–1534.

110. D. Liu, X. He, K. Wang, C. He, H. Shi, and L. Jian, "Biocompatible silica nanoparticles-insulin conjugates for mesenchymal stem cell adipogenic differentiation," *Bioconjugate Chemistry*, 2010. **21**(9):1673–1684.

111. T. Asefa and Z. Tao, "Biocompatibility of mesoporous silica nanoparticles," *Chemical Research in Toxicology*, 2012. **25**(11):2265–2284.

112. M. A. Correa-Duarte, M. Giersig, and L. M. Liz-Marzán, "Stabilization of CdS semiconductor nanoparticles against photodegradation by a silica coating procedure," *Chemical Physics Letters*, 1998. **286**(5–6):497–501.

113. P. Mulvaney, L. M. Liz-Marzán, M. Giersig, and T. Ung, "Silica encapsulation of quantum dots and metal clusters," *Journal of Materials Chemistry*, 2000. **10**(6):1259–1270.

114. T. T. Tan, S. T. Selvan, L. Zhao, S. Gao, and J. Y. Ying, "Size control, shape evolution, and silica coating of near-infrared-emitting PbSe quantum dots," *Chemistry of Materials*, 2007. **19**(13):3112–3117.

115. D. Wang, J. Qian, F. Cai, S. He, S. Han, and Y. Mu, "'Green'-synthesized near-infrared PbS quantum dots with silica-PEG dual-layer coating: ultrastable and biocompatible optical probes for in vivo animal imaging," *Nanotechnology*, 2012. **23**(24):245701.

116. T. Ung, L. M. Liz-Marzán, and P. Mulvaney, "Controlled method for silica coating of silver colloids. influence of coating on the rate of chemical reactions," *Langmuir*, 1998. **14**(14):3740–3748.

117. V. V. Hardikar and E. Matijević, "Coating of nanosize silver particles with silica," *Journal of Colloid and Interface Science*, 2000. **221**(1):133–136.

118. Y. Kobayashi, H. Katakami, E. Mine, D. Nagao, M. Konno, and L. M. Liz-Marzán, "Silica coating of silver nanoparticles using a modified Stöber method," *Journal of Colloid and Interface Science*, 2005. **283**(2):392–396.

119. L. M. Liz-Marzán, M. Giersig, and P. Mulvaney, "Synthesis of nanosized gold-silica core-shell particles," *Langmuir*, 1996. **12**(18):4329–4335.

120. E. Mine, A. Yamada, Y. Kobayashi, M. Konno, and L. M. Liz-Marzán, "Direct coating of gold nanoparticles with silica by a seeded polymerization technique," *Journal of Colloid and Interface Science*, 2003. **264**(2):385–390.

121. I. Pastoriza-Santos, J. Pérez-Juste, and L. M. Liz-Marzán, "Silica-coating and hydrophobation of CTAB-stabilized gold nanorods," *Chemistry of Materials*, 2006. **18**(10):2465–2467.

122. C. Fernández-López, C. Mateo-Mateo, R. n. A. Álvarez-Puebla, J. Pérez-Juste, I. Pastoriza-Santos, and L. M. Liz-Marzán, "Highly controlled silica coating of PEG-capped metal nanoparticles and preparation of SERS-encoded particles," *Langmuir*, 2009. **25**(24):13894–13899.

123. Q. Liu, Z. Xu, J. A. Finch, and R. Egerton, "A novel two-step silica-coating process for engineering magnetic nanocomposites," *Chemistry of Materials*, 1998. **10**(12):3936–3940.

124. F. G. Aliev, M. A. Correa-Duarte, A. Mamedov, J. W. Ostrander, M. Giersig, L. M. Liz-Marzán, and N. A. Kotov, "Layer-by-layer assembly of core-shell magnetite nanoparticles: effect of silica coating on interparticle interactions and magnetic properties," *Advanced Materials*, 1999. **11**(12):1006–1010.

125. W. Zhao, J. Gu, L. Zhang, H. Chen, and J. Shi, "Fabrication of uniform magnetic nanocomposite spheres with a magnetic core/mesoporous silica shell structure," *Journal of the American Chemical Society*, 2005. **127**(25):8916–8917.

126. Y. Sun, L. Duan, Z. Guo, Y. DuanMu, M. Ma, L. Xu, Y. Zhang, and N. Gu, "An improved way to prepare superparamagnetic magnetite-silica core-shell nanoparticles for possible biological application," *Journal of Magnetism and Magnetic Materials*, 2005. **285**(1–2):65–70.

127. W. Chen, N. Xu, L. Xu, L. Wang, Z. Li, W. Ma, Y. Zhu, C. Xu, and N. A. Kotov, "Multifunctional magnetoplasmonic nanoparticle assemblies for cancer therapy and diagnostics (theranostics)," *Macromolecular Rapid Communications*, 2010. **31**(2):228–236.

128. J. E. Lee, N. Lee, T. Kim, J. Kim, and T. Hyeon, "Multifunctional mesoporous silica nanocomposite nanoparticles for theranostic applications," *Accounts of Chemical Research*, 2011. **44**(10):893–902.

129. G. Bhakta, R. K. Sharma, N. Gupta, S. Cool, V. Nurcombe, and A. Maitra, "Multifunctional silica nanoparticles with potentials of imaging and gene delivery," *Nanomedicine: Nanotechnology, Biology and Medicine*, 2011. **7**(4):472–479.

130. S. Y. Lim, J. H. Kim, J. S. Lee, J. Ahn, M.-G. Kim, and C. B. Park, "Multi-layered stacks of fluorescent dye-doped silica nanoparticles decorated by gold nanoparticles for solid-phase optical biosensing," *Journal of Materials Chemistry*, 2011. **21**:17623–17626.

131. H. Liu, T. Liu, X. Wu, L. Li, L. Tan, D. Chen, and F. Tang, "Targeting gold nanoshells on silica nanorattles: a drug cocktail to fight breast tumors via a single irradiation with near-infrared laser light," *Advanced Materials*, 2012. **24**(6):755–761.

132. X. Wang, H. R. Chen, Y. Y. Zheng, M. Ma, Y. Chen, K. Zhang, D. P. Zeng, and J. L. Shi, "Au-nanoparticle coated mesoporous silica nanocapsule-based multifunctional platform for ultrasound mediated imaging, cytoclasis and tumor ablation," *Biomaterials*, 2013. **34**(8):2057–2068.

133. D.-W. Wang, X.-M. Zhu, S.-F. Lee, H.-M. Chan, H.-W. Li, S. K. Kong, J. C. Yu, C. H. K. Cheng, Y.-X. J. Wang, and K. C.-F. Leung, "Folate-conjugated Fe_3O_4@SiO_2@gold nanorods@mesoporous SiO_2 hybrid nanomaterial: a theranostic agent for magnetic resonance imaging and photothermal therapy," *Journal of Materials Chemistry B*, 2013. **1**:2934–2942.

134. Y. Lu, Y. Yin, Z.-Y. Li, and Y. Xia, "Synthesis and self-assembly of Au@SiO_2 core-shell colloids," *Nano Letters*, 2002. **2**(7):785–788.

135. Y.-H. Deng, C.-C. Wang, J.-H. Hu, W.-L. Yang, and S.-K. Fu, "Investigation of formation of silica-coated magnetite nanoparticles via sol-gel approach," *Colloids*

and Surfaces A: Physicochemical and Engineering Aspects, 2005. **262**(1–3):87–93.

136. D. Yang, J. Hu, and S. Fu, "Controlled synthesis of magnetite-silica nanocomposites via a seeded sol-gel approach," *The Journal of Physical Chemistry C*, 2009. **113**(18):7646–7651.

137. P. Yang, X. Li, R. Zhang, N. Liu, and Y. Zhang, "Nanocrystals encapsulated in SiO_2 particles: silanization and homogenous coating for bio applications," *Journal of Nanoscience and Nanotechnology*, 2013. **13**(3):1784–1788.

138. T. Li, J. Moon, A. A. Morrone, J. J. Mecholsky, D. R. Talham, and J. H. Adair, "Preparation of Ag/SiO_2 nanosize composites by a reverse micelle and sol-gel technique," *Langmuir*, 1999. **15**(13):4328–4334.

139. S. Santra, R. Tapec, N. Theodoropoulou, J. Dobson, A. Hebard, and W. Tan, "Synthesis and characterization of silica-coated iron oxide nanoparticles in microemulsion: the effect of nonionic surfactants," *Langmuir*, 2001. **17**(10):2900–2906.

140. T. Tago, S. Tashiro, Y. Hashimoto, K. Wakabayashi, and M. Kishida, "Synthesis and optical properties of SiO_2-coated CeO_2 nanoparticles," *Journal of Nanoparticle Research*, 2003. **5**(1–2):55–60.

141. C.-W. Lu, Y. Hung, J.-K. Hsiao, M. Yao, T.-H. Chung, Y.-S. Lin, S.-H. Wu, S.-C. Hsu, H.-M. Liu, C.-Y. Mou, C.-S. Yang, D.-M. Huang, and Y.-C. Chen, "Bifunctional magnetic silica nanoparticles for highly efficient human stem cell labeling," *Nano Letters*, 2007. **7**(1):149–154.

142. A. Narita, K. Naka, and Y. Chujo, "Facile control of silica shell layer thickness on hydrophilic iron oxide nanoparticles via reverse micelle method," *Colloids and Surfaces A: Physicochemical and Engineering Aspects*, 2009. **336**(1–3):46–56.

143. Y. T. Kim, S. M. Cho, Y. G. Seo, H. D. Yoon, Y. M. Im, and D. H. Yoon, "Influence of hydrogen on SiO_2 thick film deposited by PECVD and FHD for silica optical waveguide," *Crystal Research and Technology*, 2002. **37**(12):1257–1263.

144. A. Teleki, S. E. Pratsinis, K. Wegner, R. Jossen, and F. Krumeich, "Flame-coating of titania particles with silica," *Journal of Materials Research*, 2005. **20**(5):1336–1347.

145. S. Basak, V. Tiwari, J. Fan, S. Achilefu, V. Sethi, and P. Biswas, "Single step aerosol synthesis of nanocomposites by aerosol routes: γ-Fe_2O_3/SiO_2 and their functionalization," *Journal of Material Research*, 2011. **26**(10):1125–1133.

146. J. C. Rostaing, F. Coeuret, J. Pelletier, T. Lagarde, and R. Etemadi, "Highly homogeneous silica coatings for optical and protective applications deposited by PECVD at room temperature in a planar uniform distributed electron cyclotron resonance plasma reactor," *Thin Solid Films*, 1995. **270**(1–2):49–54.

147. S. M. Han and E. S. Aydil, "Study of surface reactions during plasma enhanced chemical vapor deposition of SiO_2 from SiH_4, O_2, and Ar plasma," *Journal of Vacuum Science & Technology A: Vacuum, Surfaces, and Films*, 1996. **14**(4):2062–2070.

148. A. Goullet, C. Vallée, A. Granier, and G. Turban, "Optical spectroscopic analyses of OH incorporation into SiO_2 films deposited from O_2/tetraethoxysilane plasmas," *Journal of Vacuum Science and Technology A: Vacuum, Surfaces and Films*, 2000. **18**(5):2452–2458.

149. K. Teshima, Y. Inoue, H. Sugimura, and O. Takai, "Room-temperature deposition of high-purity silicon oxide films by RF plasma-enhanced CVD," *Surface and Coatings Technology*, 2001. **146–147**:451–456.

150. K. Teshima, Y. Inoue, H. Sugimura, and O. Takai, "Growth and structure of silica films deposited on a polymeric material by plasma-enhanced chemical vapor deposition," *Thin Solid Films*, 2002. **420–421**:324–329.

151. T. Tsuru, H. Shigemoto, M. Kanezashi, and T. Yoshioka, "2-Step plasma-enhanced CVD for low-temperature fabrication of silica membranes with high gas-separation performance," *Chemical Communications*, 2011. **47**(28):8070–8072.

152. H. Nagasawa, H. Shigemoto, M. Kanezashi, T. Yoshioka, and T. Tsuru, "Characterization and gas permeation properties of amorphous silica membranes prepared via plasma enhanced chemical vapor deposition," *Journal of Membrane Science*, 2013. **441**:45–53.

153. K. Okimura and N. Maeda, "Dissociation processes in plasma enhanced chemical vapor deposition of SiO_2 films using tetraethoxysilane," *Journal of Vacuum Science & Technology A*, 1998. **16**(6):3157–3163.

154. P. González, D. Fernández, J. Pou, E. García, J. Serra, B. León, and M. Pérez-Amor, "Photo-induced chemical vapour deposition of silicon oxide thin films," *Thin Solid Films*, 1992. **218**(1–2):170–181.

155. P. Bergonzo, U. Kogelschatz, and I. W. Boyd, "Direct photo-deposition of silicon dioxide films using a xenon excimer lamp," *Applied Surface Science*, 1993. **69**(1–4):393–397.

156. P. Bergonzo and I. W. Boyd, "Rapid photo-deposition of silicon dioxide films using 172 nm VUV light," *Electronics Letters*, 1994. **30**(7):606–608.

157. P. González, E. García, J. Pou, D. Fernández, J. Serra, B. León, and M. Pérez-Amor, "Silicon oxide thin films grown by Xe_2* excimer lamp chemical vapour deposition: the role of the substrate temperature and the window-substrate distance," *Thin Solid Films*, 1994. **241**(1–2):348–351.

158. K. Awazu and H. Onuki, "Photo-induced synthesis of amorphous SiO_2 film from tetramethoxy-silane on polymethylmethacrylate at room temperature," *Journal of Non-Crystalline Solids*, 1997. **215**(2–3):176–181.

159. K. Awazu and T. Shimizu, "Photochemical synthesis of amorphous SiO_2 derived from tetramethoxy silane using excimer lamps," *Journal of Non-Crystalline Solids*, 2000. **272**(2–3):154–162.

160. K. Kurosawa, N. Takezoe, H. Yanagida, J. Miyano, Y. Motoyama, K. Toshikawa, Y. Kawasaki, and A. Yokotani, "Silica film preparation by chemical vapor deposition using vacuum ultraviolet excimer lamps," *Applied Surface Science*, 2000. **168**(1–4):37–40.

161. A. Yokotani, K. Amari, Y. Maezono, K. Toshikawa, and K. Kurosawa, "Analysis of the photochemical reaction on the surface for room temperature deposition of SiO_2 thin films by photo-CVD using vacuum ultraviolet light," *Japanese Journal of Applied Physics*, 2005. **44**(2):1019–1021.

162. D.-R. Chen and D. Y. H. Pui, "A high efficiency, high throughput unipolar aerosol charger for nanoparticles," *Journal of Nanoparticle Research*, 1999. **1**(1):115–126.

163. M. Fonin, R. Pentcheva, Y. S. Dedkov, M. Sperlich, D. V. Vyalikh, M. Scheffler, U. Rüdiger, and G. Güntherodt, "Surface electronic structure of the Fe_3O_4(100): evidence of a half-metal to metal transition," *Physical Review B*, 2005. **72**(10):104436.

164. T. Jung, H. Burtscher, and A. Schmidt-Ott, "Multiple charging of ultrafine aerosol particles by aerosol photoemission (APE)," *Journal of Aerosol Science*, 1988. **19**(4):485–490.

165. D. Matter, M. Mohr, W. Fendel, A. Schmidt-Ott, and H. Burtscher, "Multiple wavelength aerosol photoemission by excimer lamps," *Journal of Aerosol Science*, 1995. **26**(7):1101–1115.

166. M. Mohr and H. Burtscher, "Photoelectric aerosol charging at high particle concentrations," *Journal of Aerosol Science*, 1997. **28**(4):613–621.

167. A. Maisels, F. Jordan, and H. Fissan, "Dynamics of the aerosol particle photocharging process," *Journal of Applied Physics*, 2002. **91**(5):3377–3383.

168. E. Hontañón and F. E. Kruis, "Single charging of nanoparticles by UV photoionization at high flow rates," *Aerosol Science and Technology*, 2008. **42**(4):310–323.

169. W. A. Hoppel and G. M. Frick, "The nonequilibrium character of the aerosol charge distributions produced by neutralizes," *Aerosol Science and Technology*, 1990. **12**(3):471–496.

170. T. K. Jain, M. K. Reddy, M. A. Morales, D. L. Leslie-Pelecky, and V. Labhasetwar, "Biodistribution, clearance, and biocompatibility of iron oxide magnetic nanoparticles in rats," *Molecular Pharmaceutics*, 2008. **5**(2):316–327.

171. L. G. Saywell and B. B. Cunningham, "Determination of iron: colorimetric o-phenanthroline method," *Industrial & Engineering Chemistry Analytical Edition*, 1937. **9**(2):67–69.

172. J. H. Yoe and A. L. Jones, "Colorimetric determination of iron with disodium-1,2-dihydroxybenzene-3,5-disulfonate," *Industrial & Engineering Chemistry Analytical Edition*, 1944. **16**(2):111–115.

173. D. G. Karamanev, L. N. Nikolov, and V. Mamatarkova, "Rapid simultaneous quantitative determination of ferric and ferrous ions in drainage waters and similar solutions," *Minerals Engineering*, 2002. **15**(5):341–346.

174. X. Huang and M. A. El-Sayed, "Gold nanoparticles optical properties and implementations in cancer diagnosis and photothermal therapy," *Journal of Advanced Research*, 2010. **1**(1):13–28.

175. J. V. Jokerst, T. Lobovkina, R. N. Zare, and S. S. Gambhir, "Nanoparticle PEGylation for imaging and therapy," *Nanomedicine*, 2011. **6**(4):715–728.

176. Z. Qin and J. C. Bischof, "Thermophysical and biological responses of gold nanoparticle laser heating," *Chemical Society Reviews*, 2012. **42**(3):1191–1217.

177. N. B. Shah, J. Dong, and J. C. Bischof, "Cellular uptake and nanoscale localization of gold nanoparticles in cancer using label-free confocal Raman microscopy," *Molecular Pharmaceutics*, 2011. **8**(1):176–184.

178. M. Haruta, "Size- and support-dependency in the catalysis of gold," *Catalysis Today*, 1997. **36**(1):153–166.

179. V. Subramanian, E. E. Wolf, and P. V. Kamat, "Catalysis with TiO_2/gold nanocomposites. effect of metal particle size on the fermi level equilibration," *Journal of the American Chemical Society*, 2004. **126**(15):4943–4950.

180. O. Rosseler, M. V. Shankar, M. K. L. Du, L. Schmidlin, N. Keller, and V. Keller, "Solar light photocatalytic hydrogen production from water over Pt and Au/TiO_2(anatase/rutile) photocatalysts: Influence of noble metal and porogen promotion," *Journal of Catalysis*, 2010. **269**(1):179–190.

181. S. T. Kochuveedu, D. P. Kim, and D. H. Kim, "Surface-plasmon-induced visible light photocatalytic activity of TiO_2 nanospheres decorated by Au nanoparticles with controlled configuration," *Journal of Physical Chemistry C*, 2012. **116**(3):2500–2506.

182. S. Mukherjee, F. Libisch, N. Large, O. Neumann, L. V. Brown, J. Cheng, J. B. Lassiter, E. A. Carter, P. Nordlander, and N. J. Halas, "Hot electrons do the impossible: plasmon-induced dissociation of H_2 on Au," *Nano Letters*, 2013. **13**(1):240–247.

183. M. Brust, M. Walker, D. Bethell, D. J. Schiffrin, and R. Whyman, "Synthesis of thiol-derivatised gold nanoparticles in a two-phase liquid-liquid system," *Journal of the Chemical Society Chemical Communications*, 1994. **7**:801–802.

184. M. Giersig and P. Mulvaney, "Preparation of ordered colloid monolayers by electrophoretic deposition," *Langmuir*, 1993. **9**:3408–3413.

185. T. Yonezawa and T. Kunitake, "Practical preparation of anionic mercapto ligand-stabilized gold nanoparticles and their immobilization," *Colloids and Surfaces A: Physicochemical and Engineering Aspects*, 1999. **149**(1–3):193–199.

186. M. Okumura, K. Tanaka, A. Ueda, and M. Haruta, "The reactivities of dimethylgold(III)β-diketone on the surface of TiO_2: A novel preparation method for Au catalysts," *Solid State Ionics*, 1997. **95**(1–2):143–149.

187. M. Okumura, S.-i. Nakamura, S. Tsubota, T. Nakamura, and M. Haruta, "Deposition of gold nanoparticles on silica by CVD of gold acethylacetonate," *Studies in Surface Science and Catalysis*, 1998. **118**:277–284.

188. J. D. Wnuk, J. M. Gorham, S. G. Rosenberg, W. F. V. Dorp, T. E. Madey, C. W. Hagen, and D. H. Fairbrother, "Electron beam irradiation of dimethyl-(acetylacetonate) gold (III) adsorbed onto solid substrates," *Journal of Applied Physics*, 2010. **107**:054301.

189. A. M. Boies, P. Lei, S. Calder, W. G. Shin, and S. L. Girshick, "Hot-wire synthesis of gold nanoparticles," *Aerosol Science and Technology*, 2011. **45**(5):654–663.

190. A. R. Lowery, A. M. Gobin, E. S. Day, N. J. Halas, and J. L. West, "Immunonanoshells for targeted photothermal ablation of tumor cells," *International Journal of Nanomedicine*, 2006. **1**(2):149–154.

191. R. Bernardi, A. Lowery, P. Thompson, S. Blaney, and J. West, "Immunonanoshells for targeted photothermal ablation in medulloblastoma and

glioma: an in vitro evaluation using human cell lines," *Journal of Neuro-Oncology*, 2008. **86**(2):165–172.

192. F. Castillo, E. D. l. Rosa, and E. Perez, "Gold aggregates on silica templates and decorated silica arrays for SERS applications," *The European Physical Journal D*, 2011. **63**:301–306.

193. M. Liong, J. Lu, M. Kovochich, T. Xia, S. G. Ruehm, A. E. Nel, F. Tamanoi, and J. I. Zink, "Multifunctional inorganic nanoparticles for imaging, targeting, and drug delivery," *ACS Nano*, 2008. **2**(5):889–896.

194. S. L. Westcott, S. J. Oldenburg, T. R. Lee, and N. J. Halas, "Formation and adsorption of clusters of gold nanoparticles onto functionalized silica nanoparticle surfaces," *Langmuir*, 1998. **14**(19):5396–5401.

195. L. Petit, J.-P. Manaud, C. Mingotaud, S. Ravaine, and E. Duguet, "Sub-micrometer silica spheres dissymmetrically decorated with gold nanoclusters," *Materials Letters*, 2001. **51**:478–484.

196. M. Xiao, H. Chen, T. Ming, L. Shao, and J. Wang, "Plasmon-modulated light scattering from gold nanocrystal-decorated hollow mesoporous silica microspheres," *ACS Nano*, 2010. **4**(11):6565–6572.

197. M. A. Hossain, Y. Ikeda, T. Hara, and Y. Nagasaki, "Novel biocompatible nanoreactor for silica/gold hybrid nanoparticles preparation," *Colloids and Surfaces B Biointerfaces*, 2013. **102**:778–782.

198. A. M. Boies, P. Lei, S. Calder, and S. L. Girshick, "Gas-phase production of gold-decorated silica nanoparticles," *Nanotechnology*, 2011. **22**(31):315603.

199. F. M. Veronese and A. Mero, "The impact of PEGylation on biological therapies," *Biodrugs*, 2008. **22**(5):315–330.

200. A. S. Thakor, R. Luong, R. Paulmurugan, F. I. Lin, P. Kempen, C. Zavaleta, P. Chu, T. F. Massoud, R. Sinclair, and S. S. Gambhir, "The fate and toxicity of Raman-active silica-gold nanoparticles in mice," *Science Translational Medicine*, 2011. **3**(79):79ra33.

201. H. Xing, W. Bu, S. Zhang, X. Zheng, M. Li, F. Chen, Q. He, L. Zhou, W. Peng, Y. Hua, and J. Shi, "Multifunctional nanoprobes for upconversion fluorescence, MR and CT trimodal imaging," *Biomaterials*, 2012. **33**(4):1079–1089.

202. S. Calder, Aerosol methods for surface modification of nanoparticles, Ph.D. thesis, 2011, University of Minnesota.

203. R. Gopalakrishnan and C. J. Hogan, "Determination of the transition regime collision kernel from mean first passage times," *Aerosol Science and Technology*, 2011. **45**(12):1499–1509.

204. R. G. Nuzzo, B. R. Zegarski, and L. H. Dubois, "Fundamental studies of the chemisorption of adsorbates on well-defined organic-surfaces," *Journal of the Electrochemical Society*, 1987. **134**(3):C110–C110.

205. V. Salgueiriño-Maceira, M. A. Correa-Duarte, M. Farle, A. López-Quintela, K. Sieradzki, and R. Diaz, "Bifunctional gold-coated magnetic silica spheres," *Chemistry of Materials*, 2006. **18**(11):2701–2706.

206. X. Ji, R. Shao, A. M. Elliott, R. J. Stafford, E. Esparza-Coss, J. A. Bankson, G. Liang, Z.-P. Luo, K. Park, J. T. Markert, and C. Li, "Bifunctional gold nanoshells with a superparamagnetic iron oxide-silica core suitable for both MR imaging and photothermal therapy," *Journal of physical Chemistry C*, 2007. **111**(17):6245–6251.

207. K. Park, G. Liang, X. Ji, Z.-P. Luo, C. Li, M. C. Croft, and J. T. Markert, "Structural and magnetic properties of gold and silica doubly coated γ-Fe_2O_3 nanoparticles," *Journal of physical Chemistry C*, 2007. **111**(50):18512–18519.

208. J. L. Lyon, D. A. Fleming, M. B. Stone, P. Schiffer, and M. E. Williams, "Synthesis of Fe oxide core/Au shell nanoparticles by iterative hydroxylamine seeding," *Nano Letters*, 2004. **4**(4):719–723.

209. H.-Y. Park, M. J. Schadt, Wang, I. I. S. Lim, P. N. Njoki, S. H. Kim, M.-Y. Jang, J. Luo, and C.-J. Zhong, "Fabrication of magnetic core@shell Fe oxide@Au nanoparticles for interfacial bioactivity and bio-separation," *Langmuir*, 2007. **23**(17):9050–9056.

210. L. Wang, J. Luo, M. M. Maye, Q. Fan, Q. Rendeng, M. H. Engelhard, C. Wang, Y. Lin, and C.-J. Zhong, "Iron oxide-gold core-shell nanoparticles and thin film assembly," *Journal of Materials Chemistry*, 2005. **15**(18):1821–1832.

211. S. Pal, M. Morales, P. Mukherjee, and H. Srikanth, "Synthesis and magnetic properties of gold coated iron oxide nanoparticles," *Journal of Applied Physics*, 2009. **105**(7):07B504.

212. P. K. Jain, Y. Xiao, R. Walsworth, and A. E. Cohen, "Surface plasmon resonance enhanced magneto-optics (SuPREMO): Faraday rotation enhancement in gold-coated iron oxide nanocrystals," *Nano Letters*, 2009. **9**(4):1644–1650.

213. S. I. Stoeva, F. Huo, J.-S. Lee, and C. A. Mirkin, "Three-layer composite magnetic nanoparticle probes for DNA," *Journal of the American Chemical Society*, 2005. **127**:15362–15363.

214. J. Kim, S. Park, J. E. Lee, S. M. Jin, J. H. Lee, I. S. Lee, I. Yang, J.-S. Kim, S. K. Kim, M.-H. Cho, and T. Hyeon, "Designed fabrication of multifunctional magnetic gold nanoshells and their application to magnetic resonance imaging and photothermal therapy," *Angewandte Chemie International Edition*, 2006. **45**:7754–7758.

215. O. Veiseh, J. W. Gunn, and M. Zhang, "Design and fabrication of magnetic nanoparticles for targeted drug delivery and imaging," *Advanced Drug Delivery Reviews*, 2010. **62**:284–304.

216. P. Saiyasitpanich, T. C. Keener, M. Lu, S.-J. Khang, and D. E. Evans, "Collection of ultrafine diesel particulate matter (DPM) in cylindrical single-stage wet electrostatic precipitators," *Environmental Science & Technology*, 2006. **40**:7890–7895.